

https://dspace.org/

Tectonic evolution of the deepwater Orange Basin (offshore South Africa) using 3D reflection seismic data: implications for hydrocarbon systems

Mahlalela, Vuyolwethu

2018

https://hdl.handle.net/10539/25624

Mahlalela, Vuyolwethu Andile (2018) Tectonic evolution of the deepwater Orange Basin (offshore South Africa) using 3D reflection seismic data:implications for hydrocarbon systems, University of the Witwatersrand, Johannesburg, https://hdl.handle.net/10539/25624

Downloaded from a DSpace repository. https://dspace.org/

Tectonic evolution of the deepwater Orange Basin (offshore South Africa) using 3D reflection seismic data: Implications for hydrocarbon systems

Vuyolwethu Mahlalela

Supervised by

Dr Zubair Jinnah

Dr Musa Manzi

A thesis submitted to the

Faculty of Science, University of the Witwatersrand

in fulfilment of the requirements for the degree of

Master of Science

Johannesburg

2018

UNIVERSITY OF THE WITWATERSRAND, JOHANNESBURG

NRF National Research Foundation

DECLARATION

I _____ (Student number: _____) am a student registered for _____ in the year _____. I hereby declare the following:

- I am aware that plagiarism (the use of someone else's work without their permission and/or without acknowledging the original source) is wrong.
- I confirm that the work submitted for assessment for the above course is my own unaided work except where I have explicitly indicated otherwise.
- I have followed the required conventions in referencing the thoughts and ideas of others.
- I understand that the University of the Witwatersrand may take disciplinary action against me if there is a belief that this is not my own unaided work or that I have failed to acknowledge the source of the ideas or words in my writing.

Signature: _____Date: _____

ABSTRACT

This study applies seismic attributes to the high-resolution 3D reflection seismic data acquired for the deepwater exploration block in the Orange Basin, offshore South Africa, to provide insight into the mechanisms controlling deformation in hydrocarbon systems. The seismic interpretation was carried out on high-resolution, prestack time-migrated 3D seismic data that image post-rift sequences from the Upper Cretaceous to the Quaternary. Three post-rift sequences were identified in the seismic sections; post-rift sequences II, IV and V. Two slumping events caused by gravity failure of the margin were also identified in the Coniacian to Santonian (post-rift sequence II) and Late Cenozoic (post-rift sequence V) sequences. The seismic data also image a thrust fault system in the lower slope, which is interpreted to have been formed by episodic gravity failure from the Coniacian to Santonian. The geometry of this thrust fault system formed independently from the two detachment levels which coincide with the Cenomanian-Turonian boundary source rocks and top of the Turonian marine shale unit. The shale detachments are inferred to be moderately overpressured. The Late Cenozoic slumping event creates S to WSW and N to ENE dipping normal faults that cross-cut one another. The thrust faults and S to WSW dipping normal faults were interpreted as possible conduits for hydrocarbon migration to the seafloor to form pockmarks. Large submarine canyons were interpreted to have formed by a combination of the two slumping events. This study is the first attempt to constrain the tectonic history of the deepwater Orange Basin through the interpretation of high-resolution 3D seismic data acquired for hydrocarbon exploration. In this study, it is proposed that high-resolution 3D seismics should be recognised as a fundamental geophysical method in studying the tectonic history of the region and to detect hydrocarbons and structures that affect these economic resources.

ACKNOWLEDGEMENTS

I am indebted to many people who have played a significant role in assisting me during my MSc journey. I would like express my sincere gratitude and appreciation to my supervisors, Dr Zubair Jinnah and Dr Musa Manzi, for their support, guidance and willingness to review my work and provide constructive feedback. It has been an incredibly rewarding experience working with you both, especially having to integrate your expertise for better insight into deepwater tectonic systems.

Special thanks are due to the National Research Foundation (NRF) for funding the research project and Shell Global Solutions International B.V. and the Petroleum Agency South Africa (PASA) for providing the 3D reflection seismic data. I would like to acknowledge IHS for providing licenses for the Kingdom Suite® seismic and geological interpretation software and Schlumberger for providing the Petrel® E&P software platform as well as the Wits Seismic Research Centre for providing research equipment for my research.

I would like to thank the Sungu Sungu Group for providing valuable information on the deepwater Orange Basin. I am particularly grateful to my mentor, Mr Solomon Lephoto from the Sungu Sungu Group, who has taught me a great deal about the petroleum exploration industry and supported my career goals.

I would also like to extend my thanks to my colleagues for those lunchtime conversations. I appreciate you all for providing me with personal and professional guidance. I am grateful to my friends for their support and prayers. This journey would not have been the same without you homies.

Above all, I would like to thank my parents, siblings and Zandi for the selfless love, support and unremitting encouragement. Thank you, mom and dad, for always being there to listen and support any decision I made although you hardly understood what my research was about. I would never be able to pay back the love and sacrifices you made to shape my life. I could not have been blessed with more amazing parents.

Table of contents

Declaration i

Abstract ii

Acknowledgements iii

Table of contents iv

List of figures vii

List of tables xvi

1. Introduction 1

1.1. Background 1

1.2. Thesis structure 2

1.3. Geological setting 2

1.4. The application of reflection seismic data in the Orange Basin 8

1.5. Project aims and objectives 9

2. Geological and structural setting of the Orange Basin 11

2.1. Sequence stratigraphy 11

2.2. Structural setting 17

2.3. Hydrocarbon migration 21

3. Review of 3D reflection seismic method 23

3.1. Background 23

3.2. Acquisition 23

3.3. Processing 27

3.4. Seismic resolution limit 30

3.5. Interpretation 31

3.5.1. Conventional 3D seismic interpretation 31

3.5.2. Autotracking and manual picking 32

3.6. Seismic attributes 32

3.6.1. Volumetric seismic attributes 33

3.6.2. Horizon-based seismic attributes 34

4. Methodology 36

4.1. Seismic interpretation 36

4.1.1. Horizon interpretation 38

4.1.2. Fault interpretation 41

4.1.3. Data conditioning 42

4.2. The application of volumetric attributes 46

4.3. 3D geological model 53

5. Structural styles in the deepwater fold and thrust belt 58

5.1. Introduction 58

5.2. Results 60

5.2.1. Basal detachment fault 60

5.2.2. Fault and fold geometries 63

5.2.3. Application of horizon-based attributes 70

5.2.4. Application of volumetric attributes 73

5.3. Interpretation and discussion 78

6. Structural controls on pockmark distribution and formation of submarine canyon 83

6.1. Introduction 83

6.2. Results 84

6.2.1. Pockmarks 84

6.2.2. Submarine canyon 88

6.3. Interpretation and discussion 91

7. Discussion 94

7.1. Seismic attributes 94

7.2. Basin evolution from Cenomanian to Quaternary 95

7.3. A comparison between the Orange Basin shelf and upper slope versus lower slope environments 101

8. Conclusion 102

References 104

Appendices 119

Appendix A 119

Appendix B: 3D geological model 125

List of figures

Figure 1.1. (a) Tectonic plate reconstruction illustrating rifting of South America and Africa at 155 Ma to 135 Ma. AB (Agulhas Bank); AFFZ (Agulhas-Falkland Fracture Zone); AP (Agulhas Plateau); EWM (Ellsworth Island); FI (Falkland Islands); LA (Luderitz Arch); MCP (Mozambique coastal plain); MEB (Maurice Ewing Bank); MR (Mozambique Ridge); OB (Orange Basin); WB (Walvis Basin) (after Watkeys, 2006). (b) A schematic diagram showing the formation of syn-rift basins in the South Atlantic. Black arrows indicate the direction of continental sediment movement (after Dingle, 1992). 4

Figure 1.2. (a) Tectonic plate reconstruction illustrating drifting of South America from Africa and development of Southern Africa's passive margin. AFFZ (Agulhas-Falkland Fracture Zone); AP (Agulhas Plateau); FI (Falkland Islands); MEB (Maurice Ewing Bank); MR (Mozambique Ridge); OB (Orange Basin); TP (Tristan Plume) (after Watkeys, 2006). (b) A Schematic diagram showing the emplacement of continental flood basalts initiating the South Atlantic drift phase and subsequent deposition of marine sediments of the Orange Basin (after Dingle, 1992). 6

Figure 1.3. Bathymetric map superimposed with the deepwater Orange Basin 3D seismic grid shown by the red polygon. The study area covers approximately 8200 km^2. Seismic profiles used in the study by Brown et al. (1995) are shown by the black lines. The green polygon shows the 2D seismic survey used in the study by de Vera et al. (2010). The green polygon extends out of the bathymetric map (basemap sourced from the National Oceanic and Atmospheric Administration, https://maps.ngdc.noaa.gov/viewers/bathymetry, March, 2017). 10

Figure 2.1. Chronostratigraphy and sequence stratigraphy of the Orange Basin illustrating the major stratigraphic units and unconformities based on various studies. 6-12, 13, 14, 15-16, 17-20 represent supersequences classified by Brown et al. (1995). OX (Oxfordian); KI (Kimmeridgian); TI (Tithonian); BE (Berriasian); VA (Valanginian); HA (Hauterivian); BA (Barremian); AP (Aptian); AL (Albian); CE (Cenomanian); TU (Turonian); CO (Coniacian); SA (Santonian); CA (Campanian); MA (Maastrichtian); Pal (Palaeocene); Eo (Eocene); Oli (Oligocene); Mio

(Miocene) and Plio (Pliocene). A to D is the classification by Paton et al. (2008) used to group sequences from the Hauterivian to Holocene. I – V represents the classification by de Vera et al. (2010) used to group sequences from the Hauterivian to Holocene. C1 – C2 represents the classification used by Kuhlmann et al. (2010) to group sequences from the Hauterivian to Holocene (after Seranne and Anka, 2005; Paton et al., 2008; de Vera et al., 2010; Kuhlmann et al., 2010; Boyd et al., 2011). 15

Figure 2.2. A schematic stratigraphic cross-section through the Orange Basin depoccentre indicating the basin structure, sedimentary sequences and source rock intervals. 6At1, 13At1, 14At1, 15At1, 17At1 and 22At1 represent type-1 unconformities or subaerial unconformities classified by Brown et al. (1995). 6At1 (drift onset unconformity); 13At1 (Mid-Aptian unconformity); 14At1 (Albian unconformity); 15At1 (Cenomanian unconformity); 17At1 (Maastrichtian unconformity) and 22At1 (Palaeogene unconformity) (modified from Jungslager, 1999). 16

Figure 2.3. A schematic cross-section illustrating the main post-rift sequences (I-V) and the Cretaceous gravity-driven system in post-rift sequence II. The gravity-driven system is characterised by landward-dipping thrust faults and basinward-dipping growth faults that sole into a common detachment. u/c represents unconformity. The Santonian is abbreviated as Sant and the Maastrichtian as Maast (modified from de Vera et al., 2010). 18

Figure 2.4. Seismic sections illustrating examples of gas escape features. (a) Gas chimney outlined by dashed black lines. (b) Yellow arrows indicating bright spots. (c) Gas chimney feeding pockmark. (d) Mud volcanoes or Mud mounds indicated by red arrows (Paton et al., 2007; Anka et al., 2014)…….. 22

Figure 3.1. A Schematic diagram illustrating raypaths for reflections from interfaces. Vp represents the compressional waves and ρ represents the density. There is an acoustic impedance contrast across these interfaces, where $V_{p2}\rho_2 > V_{p1}\rho_1$ or $V_{p2}\rho_2 < V_{p1}\rho_1$ (After Thomas, 2015). 24

Figure 3.2. Processing flow used to process the Orange Basin 3D seismic data. The green box shows processing done by Dolphin Geophysical Polar Duchess. The blue boxes show processing done using SIPMAP ((Kramer and Heck, 2014). 29

Figure 4.1. Bathymetric map superimposed with the deepwater Orange Basin licence area indicated by the red polygon. The study area covers approximately 8200 km^2. The green polygon shows the 2D seismic survey used in a study by Hirsch et al. (2007). Borehole data used to calculate the densities of the rocks are found within the green polygon (basemap sourced from the National Oceanic and Atmospheric Administration, https://maps.ngdc.noaa.gov/viewers/bathymetry, March, 2017) .. 37

Figure 4.2. A survey map of the deepwater Orange Basin licence area showing inlines (parallel to acquisition direction) and crosslines (perpendicular to acquisition direction). The survey is 8000km^2. The 400km^2 study area is highlighted by the red polygon. 38

Figure 4.3. An amplitude display seismic section showing velocities (m/s) and densities (g/cm^3) of the stratigraphic units. The green arrows indicate the picked interfaces that produce strong reflections. The Cenomanian-Turonian boundary is discontinuous. The black boxes highlight areas where reflectors terminate below the Maastrichtian unconformity. The vertical exaggeration (VE) of the section is 8: 1.. 41

Figure 4.4. A depth structure map of the horizon at the top of the thrust fault system (base of the Santonian) highlighting an area with low signal-to-noise ratio (indicated by the dashed box). The red line indicates an arbitrary line that passes through the area of low signal-to-noise ratio presented in Figure 4.5. 44

Figure 4.5. An amplitude seismic section showing the structurally complex area with low signal-to-noise ratio in the NE portion of the study area. This area is highlighted by the blue dashed box. The vertical exaggeration (VE) of the section is 8:1.. 44

Figure 4.6. The seafloor horizon (a) before and (b) after smoothing using the Gaussian method. The dashed box highlights a structurally complex area where noise was generated by manual picking. 45

Figure 4.7. Horizon at the top of the thrust fault system (base of the Santonian) (a) before and (b) after applying the Kriging method to interpolate in structurally complex areas with sparse data. The dashed box highlights the areas that are structurally complex or have sparse data 45

Figure 4.8. Chaos attribute applied to the (a) inline, (b) crossline and (c) time slice (Z = 2400 ms) prior to ant tracking computation. Blue arrows indicate structures that were further enhanced by ant

tracking. In (a) and (b), the darkest zones are zones with high chaoticness. These highly chaotic zones are fracture/fault zones. Sections (a) and (b) are vertically exaggerated by a factor of 7... 47

Figure 4.9. Stereonet filters used to computer ant tracking seismic cube. (a) Stereonet for normal faults dipping at 0°-90° N to ENE (b) Stereonet for normal faults dipping at 0°-90° S to WSW..... 49

Figure 4.10. (a) An ant tracked volume of the first run with the stereonet filter applied to detect faults dipping N-ENE. The red arrows point to fault whose continuity is highlighted in the second run. (b) An ant tracked volume of the second run with the stereonet filter applied to detect faults dipping N-ENE. Sections (a) and (b) are vertically exaggerated by a factor of 7.…..... 51

Figure 4.11. An ant tracked volume highlighting the extracted N-ENE dipping faults in green. Vertical exaggeration (VE) is 7:1.. 52

Figure 4.12. An ant tracked volume highlighting the S-WSW dipping faults in pink. Vertical exaggeration (VE) is 7:1.. 53

Figure 4.13. 3D seismic volume overlain with gridded horizons. The contour interval is 50 m. Vertical exaggeration (VE) is 7:1 54

Figure 4.14. Horizons are intersected with the fault framework to create solid model. The model is divided into five zones. 55

Figure 4.15. 3D model showing layering and displacement of layers due to faulting. 56

Figure 4.16. Workflow used to construct a 3D geological model of the deepwater Orange Basin. 57

Figure 5.1. Chronostratigraphic and sequence chart for the Orange Basin illustrating major stratigraphic units and sedimentation rates. Stratigraphic units below the red line were cut from the seismic volume. 6-12, 13, 14, 15-16, 17-20 represent supersequences classified by Brown et al. (1995). OX (Oxfordian); KI (Kimmeridgian); TI (Tithonian); BE (Berriasian); VA (Valanginian); HA (Hauterivian); BA (Barremian); AP (Aptian); AL (Albian); CE (Cenomanian); TU (Turonian); CO (Coniacian); SA (Santonian); CA (Campanian); MA (Maastrichtian); Pal (Palaeocene); Eo (Eocene); Oli (Oligocene); Mio (Miocene) and Plio (Pliocene). I – V represents the classification by de Vera et al. (2010) used to group sequences from the Hauterivian to Holocene (modified from Boyd et al., 2011; Loegering et al., 2013).…..... 59

Figure 5.2. (a) An amplitude display seismic section and (b) a schematic diagram showing thrust faults attached to two basal detachment levels. The thrust faults to the NW sole into the Coniacian detachment and the thrust faults to the SE sole into the Cenomanian-Turonian detachment. Post-rift sequences II, IV and V were identified. Sections (a) and (b) are vertically exaggerated by a factor of 3. 61

Figure 5.3. An amplitude display section showing the Coniacian and Cenomanian-Turonian detachments. The Cenomanian-Turonian detachment is terminated by a slump deposit in the south. The vertical exaggeration (VE) of the section is 17:1..... 62

Figure 5.4. A depth structure map of the Cenomanian-Turonian detachment layer showing the discontinuous nature of the detachment. The detachment layer is at shallower depths in the north and progressively deepens towards the south. The contour interval for the map is 50 m. 63

Figure 5.5. A 3D model of the thrust fault system showing variations in dip angle with depth and to the north, the faults dip steeply. The faults in the south, along the deformation front, have dip angles between 30° and 40°, and shallow to 10° with depth. In the north, the faults are dipping at high angles (60° - 70). The vertically exaggeration (VE) is 5:1. 64

Figure 5.6. An amplitude display seismic section showing faults at the deformation front. The horizon used to measure displacement along the fault is highlighted. . The vertical exaggeration (VE) of the section is 8:1. 65

Figure 5.7. An elevation map of the horizon located at the top of the thrust fault system (base of the Santonian) (highlighted in Figure 5.5) with an overlay of thrust fault polygons. The faults are trending WNW-ESE. The red line represents an arbitrary line presented in Figure 5.8. 66

Figure 5.8. A south-to-north profile of the Coniacian to Santonian thrust fault system showing variations in vertical displacement with distance along the strike of the fault. The faults in grey occur along the deformation front; the faults in green are mapped in the inner part of the thrust fault system and the faults in pink are at the rear of the thrust fault system. Anomalous displacement measurements are indicated by the red circles. 67

Figure 5.9. An amplitude display seismic section showing the geometry of the folds. The folds are asymmetric with backlimbs that dip gentler than the fault ramp. The backlimbs dip approximately 4° – 24°. The thrust faults cut through the forelimbs of the folds and the footwall synclines. The area to the north is structurally complex and highly deformed compared to the south. The black block highlights faults along the deformation front; green block highlights faults in the inner part of thrust fault system and pink block shows faults at the rear of the system. Vertical exaggeration (VE) is 3:1 69

Figure 5.10. (a) A dip map of the Maastrichtian unconformity highlighting faults trending WNW-ESE with varying dip angles along the faults in the central region (marked by the dashed polygon). To the north, the faults are discontinuous and they have a NE-SW trend (indicated by blue arrow). The southern portion of the study area (below the dashed polygon) is less faulted. (b) A dip azimuth map of the Maastrichtian unconformity showing faults dipping SW-WSW in the central region of the study area (marked by the red arrow). In the northern and southern regions, the faults are dipping predominantly to the north, indicated by the black arrows. The contour interval for (a) and (b) is 100 m. 71

Figure 5.11. (a) A dip map of the base of the Palaeogene horizon illustrating a dense fault network trending WNW-ESE with varying dip angles along the faults in the central region of the study area (indicated by the dashed polygon). To the north, the faults are disconnected and they have a more NE-SW trend. To the south, there is less faulting and the faults are discontinuous. (b) A dip azimuth map of the base of the Palaeogene horizon illustrating faults dipping SW-WSW in the central region of the study area (indicated by the red arrow). In the northern and southern regions, the faults are dipping predominantly N to NW (indicated by the black arrows). The contour interval for (a) and (b) is 100 m. 72

Figure 5.12. An amplitude display of inline 15648. A number of normal faults displace the Maastrichtian unconformity and base of the Palaeogene horizons. The faults indicated by the red and green arrows have displacement below the vertical resolution limit of 12 m, thus cannot be seen on the amplitude display. The vertical exaggeration (VE) of the section is 7:1. 74

Figure 5.13. Chaos attribute applied to inline 15648 prior to ant tracking computation. The red and green arrows indicate normal faults, with fault displacement below the vertical resolution limit of 12 m, which were enhanced by the chaos attribute. Vertical exaggeration (VE) of the section is 7:1. 74

Figure 5.14. Ant tracked sections of inline 15648. These sections show the (a) first run and (b) second run of the ant tracking algorithm limited to detecting fault with a N to ENE dip direction and dip angles between 0° and 90°. A number of faults have been highlighted by the attribute. The faults marked by the red arrows are difficult to see on the amplitude seismic display. Section (a) and (b) are vertically exaggerated by a factor of 7.. 75

Figure 5.15. An ant tracked section of inline 15648 limited to detecting fault with a S to WSW dip direction and dip angles between 0° and 90°. A number of faults have been highlighted by the attribute. The faults marked by the green arrows are below the vertical resolution limit of 12 m. Vertical exaggeration (VE) is 7:1. 76

Figure 5.16. (a) Time slice of ant tracking attribute showing N to NE dipping normal faults (indicated by the dashed polygon). The first run was computed with parameters reflecting the more aggressive ants and the second run was computed with parameters reflecting the passive ants. The faults within the polygon are fragmented. (b) Time slice of ant tracking attribute showing S to WSW dipping normal faults (indicated by the dashed polygon) computed with parameters reflecting aggressive ants. The faults within the polygon are interconnected..... 77

Figure 5.17. (a) Uninterpreted amplitude section. (b) Interpreted amplitude section showing the Coniacian detachment along the base of the wedge. The vertical exaggeration (VE) for (a) and (b) is 17:1..... 779

Figure 5.18. An amplitude display seismic section showing a large displacement (between the pink dotted lines) at the centre of the fault indicated by the black arrows and smaller displacement towards the detachment (indicated by the blue arrows) and fault tip (black circle) indicated by the green arrows. Faults propagate through fault limbs forming fault breakthrough folds. Both the footwall and hangingwall units are thickened, resulting in a constant thickness across dip domains. Vertical exaggeration (VE) of the section is 8:1. 81

Figure 6.1. (a) A depth structure map, (b) dip azimuth map, (c) dip map and (d) edge detection map of the Holocene seafloor highlighting the pockmarks identified in the study area (black dashed polygon). The contour interval for all the maps is 50 m. 85

Figure 6.2. Ant tracked volume with the stereonet filter applied to detect faults dipping N-ENE. A number of faults have been highlighted above the Coniacian-Santonian thrust fault system. The normal faults indicated by the red arrows are linked to the thrust faults. The normal faults terminate in the Palaeogene. The pockmarks are shown by the dashed ellipse. Vertical exaggeration (VE) is 7:1.. 86

Figure 6.3. Ant tracked volume with stereonet filter applied to detect fault with a S-WSW dip direction. The green arrows indicate the termination of the S-WSW dipping normal faults below pockmarks. The red ellipse shows the connectivity between thrust fault and normal fault that propagated to the surface beneath the pockmarks (marked by black dashed circles). Vertical exaggeration (VE) is 7:1.. 87

Figure 6.4. An amplitude display seismic section illustrating the structures imaged in the deepwater Orange Basin. The submarine canyon is formed above the deformation front of the thrust fault system. It has a width of 45 km and is incised to depths of approximately 650 m. The vertical exaggeration (VE) of the section is 17:1 89

Figure 6.5. A dip map of the seafloor horizon highlighting the dip of the canyon wall and pockmarks, in the area marked by the dashed polygon. 90

Figure 7.1. 3D model showing landward-dipping thrust faults becoming slightly curved as they attach to the Cenomanian-Turonian detachment. The thrust faults that connect to the Coniacian detachment maintain a planar geometry. The full 3D model animation can be viewed in the attachment. 97

Figure 7.2. 3D model illustrating deposition of (a) Maastrichtian and (b) early Palaeogene units before formation of N-ENE and W-WSW dipping normal faults. The S-WSW dipping normal faults intersect some of the Coniacian-Santonian thrust faults. The N dipping normal faults are reactivated thrust faults. The continuation of the thrust faults into the Palaeogene is not visible in this view of the model. The full 3D model animation can be viewed in the attachment. 99

Figure 7.3. 3D model showing the stratigraphic units and their corresponding megasequences identified in the deepwater Orange Basin and the intersection of S-WSW dipping normal faults with the base of the pockmark. The continuation of the thrust faults into the Palaeogene is not visible in this view of the model. The full 3D model animation can be viewed in the attachment. 100

List of tables

Table 3.1. Acquisition parameters for the Orange Basin 3D seismic survey (Kramer and Heck, 2014) 26

Table 4.1. The parameters used in the application of the ant tracking attribute on the 3D seismic volume (After Pereira, 2009)..... 48

1. INTRODUCTION

1.1. Background

The breakup of Gondwana during the Late Jurassic and subsequent opening of the South Atlantic Ocean during the Early Cretaceous led to the development of passive margins on the eastern flank of South America and western flank of Africa, both of which host thick syn-rift and post-rift siliclastic successions (Brown et al., 1995; Clemson et al., 1997; Séranne and Anka, 2005; Hirsch et al., 2007; Kuhlmann et al., 2010). Hydrocarbon exploration and discovery have a long history on the eastern flank of South America and northern/central West Africa; however modern exploration techniques have only been applied in southwestern Africa from the mid-1970s (Petroleum Agency South Africa, 2013). Exploration techniques applied to delineate prospective hydrocarbon plays in shallow water environments (with water depths extending to 450 m) offshore southwestern Africa involved the use of 2D reflection seismic data. After 1990, seismic coverage was extended to deepwater areas with water depths greater than 450 m (Muntingh, 1993). With exploration interests shifting progressively to more deepwater areas, recent studies have investigated the gravity-driven systems that extend from the outer shelf through to the abyssal plain and their controls on hydrocarbon accumulation and migration (Granado et al., 2009; Kuhlmann et al., 2010; de Vera et al., 2010; Boyd et al., 2011).

Extensive research has been conducted in sedimentary basins offshore southwestern Africa, particularly along shelfal areas in the Orange Basin, using 2D and 3D reflection seismic data (Light et al., 1992; Light et al., 1993; Brown et al., 1995; Coward et al., 1999; Jungslager, 1999; Broad et al., 2006; Hirsch et al., 2007; Paton et al., 2007; Paton et al., 2008; Hirsch et al., 2010; Kuhlmann et al., 2010; Boyd et al., 2011; Kuhlmann et al., 2011). Although the structural and depositional setting of the Orange Basin has been studied extensively, the deepwater areas within the Orange Basin remain underexplored. The structural and depositional settings of the deepwater areas in the Orange Basin have not been constrained by 3D seismic data. This study uses high-resolution 3D reflection seismic data provided by Shell Global Solutions International B.V. to constrain the interpretation of the depositional

and structural settings of the deepwater Orange Basin. 3D reflection seismic data have the advantage of mapping deep-seated structures compared to geological, potential field and 2D seismic data. The 3D seismic data were interpreted using seismic attribute analysis. This allowed for the detection of faults with a vertical displacement as small as 12 m, which can have a direct impact on mapping the extent of structurally-controlled hydrocarbon plays.

1.2. Thesis structure

This thesis is divided into eight chapters. Chapter 1 highlights the geological and geophysical background and objectives of the study. Chapter 2 presents the geological and structural setting of the Orange Basin. This chapter also summarises hydrocarbon migration features previously identified in the Orange Basin. Chapter 3 provides a review of the theory and application of the 3D reflection seismic method to hydrocarbon exploration. In addition, the seismic attributes used in this study are described. Chapter 4 contains the detailed methodology carried out in this study. In chapter 5, major and small-scale faults are identified and constrained from the 3D seismic data. The chapter addresses the formation of these structures. Chapter 6 builds on the results of chapter 5 by linking the fault formation to the formation of hydrocarbon migration features and a submarine canyon. Chapter 7 details the basin evolution from Cenomanian to Holocene and compares the shelf and upper continental slope settings to the lower slope environment in the Orange Basin. Chapter 8 summarises the main conclusions and important implications of this study.

1.3. Geological setting

The southwestern continental margin of Africa is a passive margin that formed in response to extensional stresses caused by the separation of the African and South American continents during the Late Jurassic and subsequent opening of the South Atlantic Ocean during the Early Cretaceous (Brown et al., 1995; Clemson et al., 1997; Séranne and Anka, 2005; Hirsch et al., 2007; Kuhlmann et al., 2010; Figure 1.1a). The rifting of Gondwana was followed by initial faulting and the formation of the Walvis,

Luderitz and Orange syn-rift basins (Figure 1.1a), which are characterised by grabens and half-grabens that trend sub-parallel to the present day coastline. The syn-rift basins were infilled by Upper Jurassic to Lower Cretaceous deposits of siliciclastic continental and lacustrine sediments, and volcanics rocks (Brown et al., 1995; Hirsch et al., 2007; Hirsch et al., 2010; Figure1.1b).

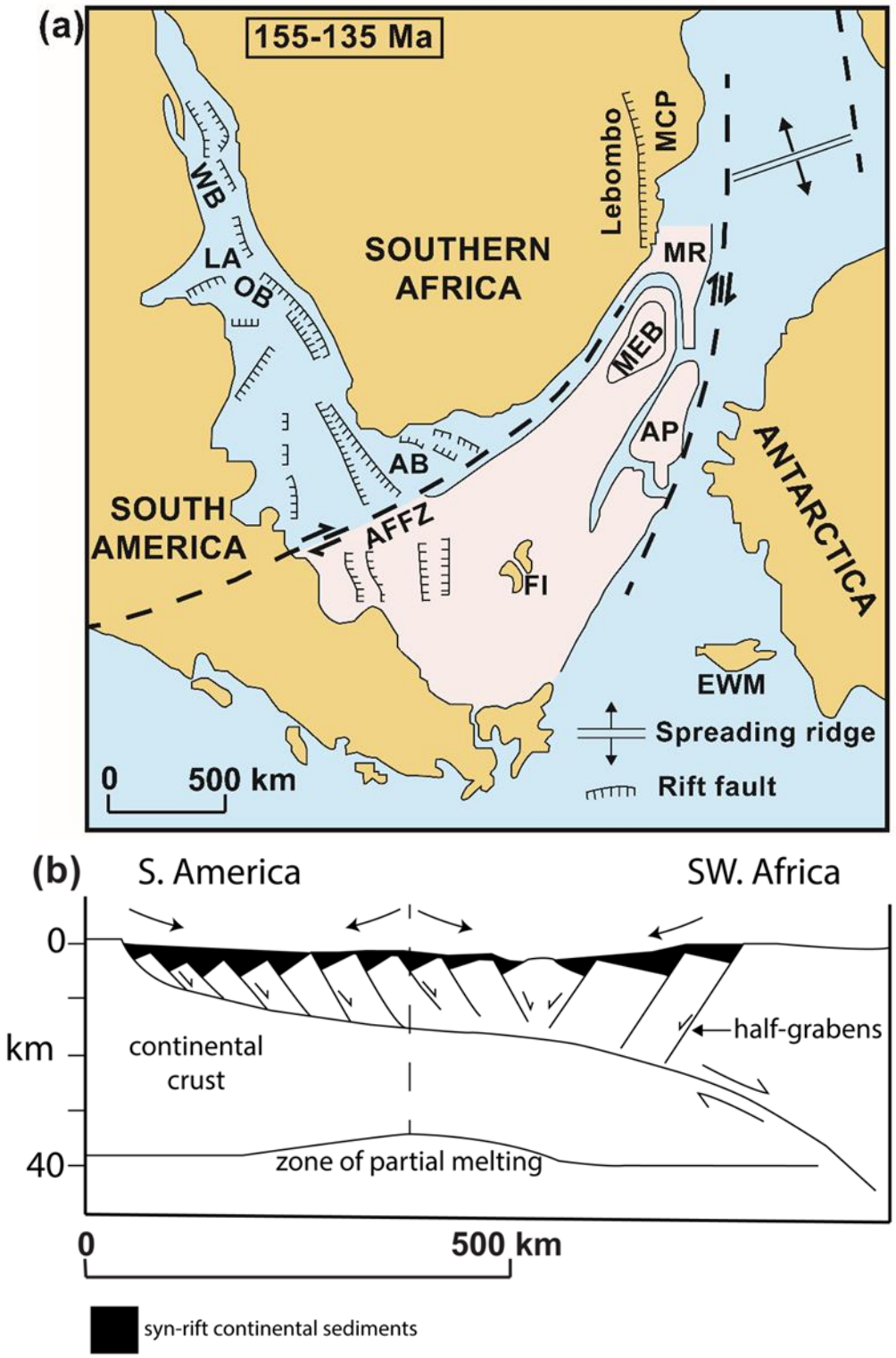


Figure 1.1. (a) Tectonic plate reconstruction illustrating rifting of South America and Africa at 155 Ma to 135 Ma. AB (Agulhas Bank); AFFZ (Agulhas-Falkland Fracture Zone); AP (Agulhas Plateau); EWM (Ellsworth Island); FI (Falkland Islands); LA (Luderitz Arch); MCP (Mozambique coastal plain); MEB (Maurice Ewing Bank); MR (Mozambique Ridge); OB (Orange Basin); WB (Walvis Basin) (after Watkeys, 2006). (b) A schematic diagram showing the formation of syn-rift basins in the South Atlantic. Black arrows indicate the direction of continental sediment movement (after Dingle, 1992).

Coevally with rifting, Paraná-Etendeka continental flood basalts were emplaced on the Namibian margin (de Vera et al., 2010; Hirsch et al., 2010). Rifting between the South American and African plates and the emplacement of the continental flood basalts during the Early Cretaceous initiated the opening of the South Atlantic Ocean; this is referred to as the South Atlantic drift phase (Figure 1.2a). Drifting initiated thermal subsidence along the continental margin, which led to the flooding of the basin. This resulted in the deposition of the Orange Basin post-rift sequences composed of deep marine sediments followed by delta progradation (Brown et al., 1995; de Vera et al., 2010; Kuhlmann et al., 2010; Figure 1.2b).

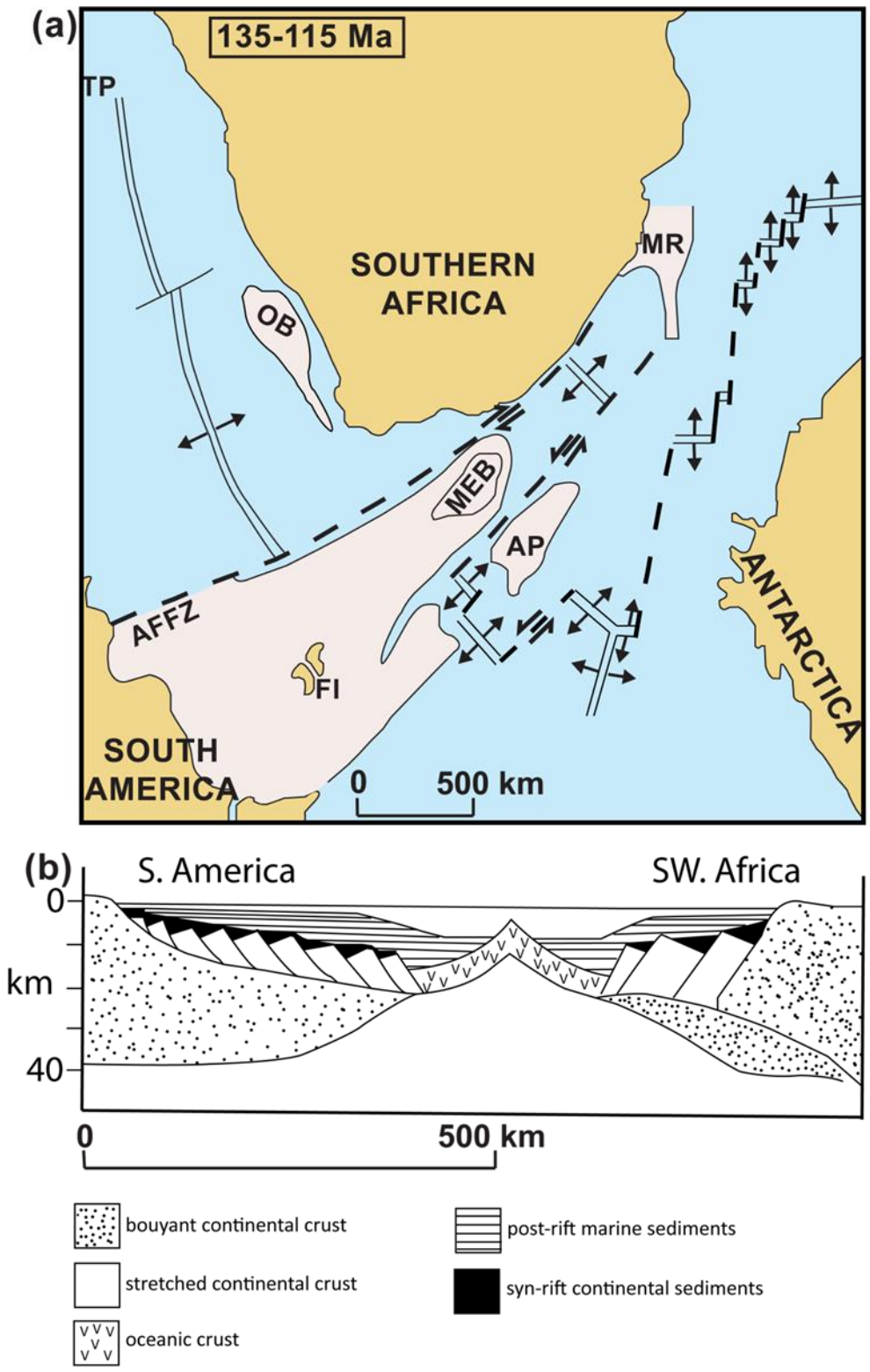


Figure 1.2. (a) Tectonic plate reconstruction illustrating drifting of South America from Africa and development of Southern Africa's passive margin. AFFZ (Agulhas-Falkland Fracture Zone); AP (Agulhas Plateau); FI (Falkland Islands); MEB (Maurice Ewing Bank); MR (Mozambique Ridge); OB (Orange Basin); TP (Tristan Plume) (after Watkeys, 2006). (b) A Schematic diagram showing the emplacement of continental flood basalts initiating the South Atlantic drift phase and subsequent deposition of marine sediments of the Orange Basin (after Dingle, 1992).

This study focuses on the onset of the South Atlantic drift phase and subsequent deposition of the post-rift sequences within the Orange Basin. The change in basin tectonics and lithofacies is due to the termination of the rift phase in the Late Hauterivian, marked by the drift onset unconformity (Dingle, 1992).

The development of a narrow seaway in the South Atlantic began in the Late Hauterivian and was terminated in the Early Aptian during a period of anoxic conditions. The timing of the anoxia coincides with that of the Early Aptian Oceanic Anoxic Event (OAE1a) (Kerr, 1998; Jungslager, 1999; Leckie et al., 2002). These anoxic conditions allowed for the deposition of Barremian and Early Aptian source rocks during periods of marine transgression. The deposition of organic-rich black shales enriched was used to infer anoxic conditions (Jungslager, 1999). In the Mid-Aptian, the southern proto-Atlantic Ocean was flushed by oxygenated waters terminating the anoxic conditions (Jungslager, 1999). Termination of the early drift phase is marked by the Mid-Aptian unconformity. Open marine conditions set in during the Barremian to Aptian, signalling the onset of the main drifting phase in the southern proto-Atlantic Ocean. A major depocentre developed as a result of thermal subsidence. Siliciclastic sediment was supplied to the depocentre by the ancestral Orange and Olifants rivers (Brown et al., 1995; Hirsch et al., 2010). Subsidence in the Orange Basin was predominantly controlled by thermal cooling and depositional loading, caused by the outbuilding of thick sedimentary successions in the Orange and Olifants deltaic systems (Brown et al., 1995).

The main drift phase was initiated during the Aptian to Cenomanian. Shelf progradation dominated during this time. This was followed by aggradation during the Cenomanian to Maastrichtian (Brown et al., 1995; Kuhlmann et al., 2010). Aggradational stacking along a steep continental margin eventually led to the collapse of an unstable shelf edge resulting in the formation of extensional growth faults, widespread slumping, toe-thrust faults and fault-related folds (Brown et al., 1995; Broad et al., 2006). These structures are collectively referred to as post-rift gravity-driven systems. Increased atmospheric and oceanic temperatures, marine transgression and widespread anoxia in the South Atlantic Ocean led to the second phase of source rock deposition in the Cenomanian and Turonian (Light et al., 1993; Kerr, 1998; de Vera et al., 2010).

During the Maastrichtian to Neogene, sediment supply and subsidence decreased as basinward prograding sedimentary wedges developed (Kuhlmann et al., 2010). The post-rift sequences can be divided into five depositional sequences of Late Hauterivian to Holocene ages, separated by numerous unconformities or correlative conformities relating to sea level changes (Coward et al., 1999; de Vera et al., 2010).

The present day continental shelf in the Orange Basin is approximately 100 km wide and extends westwards to 500 m water depths. The shelf break is 500 m deep and the slope extends from 500 m to 2500 m deep (Rogers and Rau, 2006).

1.4. The application of reflection seismic data in the Orange Basin

The interpretation of 2D reflection seismic data acquired by Soekor (Pty) Ltd in the late 1980s has led to the discovery of several hydrocarbon plays within sedimentary basins in the offshore environment of South Africa (Muntingh, 1993; Brown et al., 1995). The combination of 2D reflection seismic data and sequence stratigraphy to explore the post-rift sequences of the Orange Basin provided high-resolution mapping of deepwater depositional systems and delineation of sediment dispersion zones on the shelf edge. Sedimentary, microfossil, petrographic and source rock data were integrated with seismic sequence stratigraphy to support mapping of depositional systems such as unconformities and depositional sequences, resulting in more detailed and refined geologic interpretations (Brown et al., 1995).

Previous studies (Light et al., 1992; Light et al., 1993; Jungslager, 1999) focused on the application of reflection seismology to define stratigraphic units, system tracts, seismic facies, depositional environments and geological structures. These studies were conducted to evaluate the potential for hydrocarbons and prospects of the basin. Recent studies (Granado et al., 2009; de Vera et al., 2010;; Kuhlmann et al., 2010; Boyd et al., 2011; Hartwig et al., 2012; Hartwig, 2014; Scarselli et al., 2016) have investigated the gravity-driven systems that extend from the outer shelf though to the abyssal plain and their controls on hydrocarbon accumulation and migration.

Extensive research (Light et al., 1992; Light et al., 1993; Brown et al., 1995; Coward et al., 1999; Jungslager, 1999; Broad et al., 2006; Hirsch et al., 2007; Paton et al., 2007; Paton et al., 2008; Hirsch et al., 2010; Kuhlmann et al., 2010; Boyd et al., 2011; Kuhlmann et al., 2011) has been conducted in the Orange Basin using 2D and 3D reflection seismic data. However, this research was limited to the continental shelf environments (Figure 1.3). There is little knowledge of the deepwater Orange Basin and previous studies (Granado et al., 2009; de Vera et al., 2010) in the area were done using a 2D seismic profile that extended from the shelf to the deepwater environment. This study utilizes high-resolution 3D reflection seismic data, acquired by Shell Global Solutions International B.V. in the deepwater Orange Basin, to reconstruct basin tectonics and depositional processes, and investigate the structural controls on hydrocarbon migration within the post-rift sequences of the deepwater Orange Basin (Figure 1.3). Conventional seismic interpretation methods are supplemented with the application of horizon-based and volumetric seismic attributes to enhance the detection of structural features that fall below the seismic resolution limit. The integration of high-resolution 3D reflection seismic data and seismic attributes will result in a comprehensive interpretation of the basin tectonics and the structural controls on hydrocarbon migration.

1.5. Project aims and objectives

The aim of this research is to reconstruct basin tectonics and depositional processes to determine whether the structures and depositional sequences identified on the continental shelf continue onto the slope and deepwater. In addition, structural controls on hydrocarbon migration within the post-rift sequences of the deepwater Orange Basin (Figure 1.3) and their timing of activity will be investigated. The project aims will be achieved by interpreting 3D reflection seismic data and applying seismic attributes such as dip, dip azimuth, edge detection, edge enhancement and ant tracking to enhance the imaging of faults and horizons that are below the seismic resolution limit. This information will help constrain the tectonics and construct a 3D regional geological model of the area incorporating seismic horizons and fault systems, which will be used to address the objectives of this research.

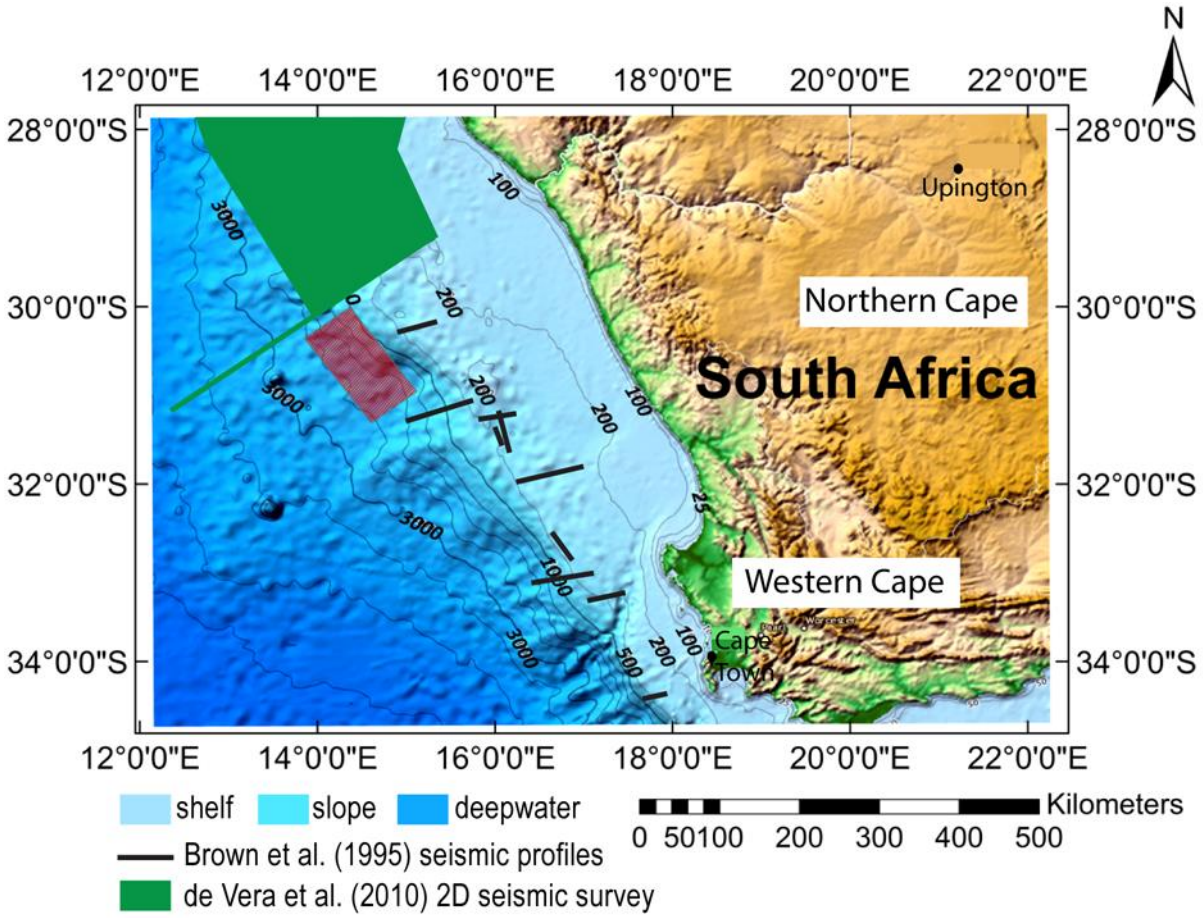


Figure 1.3. Bathymetric map superimposed with the deepwater Orange Basin 3D seismic grid shown by the red polygon. The study area covers approximately 8200 km^2. Seismic profiles used in the study by Brown et al. (1995) are shown by the black lines. The green polygon shows the 2D seismic survey used in the study by de Vera et al. (2010). The green polygon extends out of the bathymetric map (basemap sourced from the National Oceanic and Atmospheric Administration, https://maps.ngdc.noaa.gov/viewers/bathymetry, March, 2017).

2. GEOLOGICAL AND STRUCTURAL SETTING OF THE ORANGE BASIN

2.1. Sequence stratigraphy

Classification of the post-rift depositional sequences in the Orange Basin is based on the identification of stratigraphically significant boundaries such as conformities and correlative conformities. These boundaries mark the top and base of the supersequences. A supersequence is defined as an unconformity bounded sedimentary deposit consisting of relatively conformable successions of genetically related strata (Van Wagoner et al., 1987; Van Wagoner et al., 1988; Brown et al., 1995; Catuneanu et al., 2011). These supersequences are interpreted to have been deposited in response to eustatic sea level changes, tectonic subsidence and changes in the rates of sediment supply (Van Wagoner et al., 1988). A supersequence can be subdivided into depositional system tracts. These include falling stage, lowstand, transgressive and highstand depositional systems tracts. Since the supersequences are deposited during one cycle of sea level rise and fall, each system tract is deposited during a specific part of the cycle of eustatic sea level rise and fall (Catuneanu et al., 2011).

Two types of unconformities are classified by Brown et al. (1995), type 1 and type 2 unconformities. Type 1 unconformities form as a result of fluvial erosion or bypass and are identified by subaerial and submarine erosion, submarine canyon formation and the deposition of a lowstand system tract (Brown, et al., 1995; Catuneanu, et al., 2011). This type of unconformity is the most common unconformity identified by Brown et al. (1995) in the post-rift Cretaceous rocks of the Orange Basin.

The post-rift successions above the Hauterivian unconformity are characterised by five supersequences reaching an estimated total thickness of approximately 7 km (Boyd et al., 2011). Brown et al. (1995) defined five supersequences made up of 28 third-order sequences and classified the Orange Basin post-rift sequences using an alphanumerical nomenclature system. Sequences with durations between 1 and 2 Ma are referred to as third-order sequences (Brown et al., 1995). Numbers ranging

from 1 to 22 in stratigraphic successions are grouped into seismically-distinctive, unconformity-bounded supersequences. The less defined sequences found in the numerically designated sequences are classified by alphabetic symbols A to E. Most sequences are classified based on the symbol given to their basal unconformities, type 1 or type 2 unconformities i.e., the basal unconformity for supersequence 14A is 14At1. The supersequences are separated by second-order type 1 unconformities and are marked by major cycles of transgression and regression reflected by component third-order sequence sets. These supersequences record depositional and tectonic events that dominated during the deposition of the post-rift sequences of the Orange Basin (Brown et al., 1995).

Supersequence 6-12 was deposited between the Late Hauterivian and Aptian, marking the end of the rift phase (Figure 2.1). This supersequence records a period of marine transgression and flooding of the drift onset unconformity 6At1 (Figure 2.2) followed by a period dominated by aggradational and to a lesser extent progradational stacking of third-order sequences. These events indicate that the rate of relative sea level rise, caused by tectonic subsidence and an increase in eustatic sea level, was more or less equal to the rate of sediment supply (Brown et al., 1995). The upper unconformity 13At1 coincides with a major 130 m eustatic drop in sea level at 112 Ma (Paton et al., 2008; Figure 2.2). The drop in sea level occurred as a result of South America and Africa drifting apart (Seranne and Anka, 2005). The eustatic drop in sea level has been documented in basins adjacent to the Atlantic Ocean which are the Basque-Cantabrian and Maestrat Basins (Spain), Wessex Basin (southern England) and Lusitanian Basin (Portugal) (García-Mondéjar, 1990; Ruffell, 1992; Dinis and Trincão, 1995; McMahon and Turner, 1998; Bover-Arnal et al., 2014). It has also been documented in the Qishn and Nahr Umr Formations in Oman and marks the beginning of convergence between the African, Arabian and Eurasian plates (Immenhauser et al., 1999; Robin et al., 2010; Hersi et al., 2014).

Supersequence 13 was deposited across the Aptian and Albian (Figure 2.1). This supersequence records a period of relative sea level fall following tectonic uplift, intensive erosion, transgression and regional flooding of unconformity 13At1 (Figure 2.2). Flooding resulted in the deposition of predominantly progradational third-order sequences, and minor aggradational third-order sequences were recognised in regions where lowstand system tracts did not occur. These events are associated

with high to moderate subsidence rates and slow decrease and increase in the eustatic sea level (Brown et al., 1995). The unconformity at the top of supersequence 13 is associated with a fall in eustatic sea level at 107 Ma (Paton et al., 2008).

Supersequence 14 was deposited between the Albian and Cenomanian (Figure 2.1). This supersequence records a period of relative sea level fall, tectonic uplift, moderate erosion, transgression and regional flooding of unconformity 14At1 (Figure 2.2). Alternating progradational and aggradational third- and fourth-order sequences (duration of ~120 ka) were deposited. These events indicate that an accelerating rise in sea level, caused by high subsidence rates, and an accelerating rise in eustatic sea level, was relatively balanced by high sediment supply (Brown et al., 1995).

Supersequence 15-16, deposited between the Cenomanian and Campanian, records a period of relative sea level fall and minor uplift followed by minor erosion, major transgression and regional flooding of unconformity 15At1 (Figure 2.2). Third- and fourth-order aggradational sequences are deposited. These aggradational sequences develop a slightly progradational geometry (Brown et al., 1995). The geometry of the third-order sequence sets indicates that a high but slowly decreasing sea level, produced by high subsidence rates and a maximum highstand of eustatic sea level, was balanced with high sediment supply rates. Aggradational stacking along an oversteepened continental margin eventually led to the collapse of an unstable shelf edge resulting in the formation of extensional growth faults, widespread slumping, toe-thrust faults and fault related folds limited to supersequence 15-16 (Brown et al., 1995; Broad et al., 2006; Figures 2.1 and 2.2).

The deposition of Supersequence 17-20 occurred between the Campanian and Maastrichtian (Figure 2.1). Following major uplift and minor marine transgression, subsequent flooding of unconformity 17At1 (Figure 2.2) resulted in the deposition of highly progradational third-order sequences. These progradational sequences develop a slightly aggradational geometry. These events indicate an accelerated drop and slow rise in sea level, produced by very low subsidence and accelerated eustatic sea level fall, coinciding with moderate to high rates of sediment supply (Brown et al., 1995).

The Upper Cretaceous post-rift depositional sequences were dated using microfossil interpretation charts constructed from the analysis of borehole data acquired by Soekor. An abundance of benthic and planktonic microfossils were documented in the marine condensed sections, which represent maximum flooding events. These marine condensed sections provided the most reliable information to correlate with global standard Cretaceous chronostratigraphy. Studies on microfossil diversity and abundance show that subtle changes in the environment may be used to confirm where unconformities and marine condensed sections are located (Brown et al., 1995).

The seismo-stratigraphic framework was first reported by Brown et al. (1995) and was later adapted by various authors (Seranne and Anka, 2005; Paton et al., 2008; Granado et al., 2009; de Vera et al., 2010; Kuhlmann et al., 2010; Figure 2.1). de Vera et al. (2010) further classified the depositional sequences from I to V incorporating the Cenozoic sedimentary deposits. The Cenozoic succession contains units that were deposited basinward of the break in slope, reaching a maximum thickness of approximately 1500 m. The geometry of this succession becomes increasingly progradational upsequence. Beyond the Cretaceous shelf break, younger episodes of gravity faulting are observed within the Cenozoic sequences (Brown et al., 1995; Paton et al., 2008). This study will use the depositional sequences classified by de Vera et al. (2010).

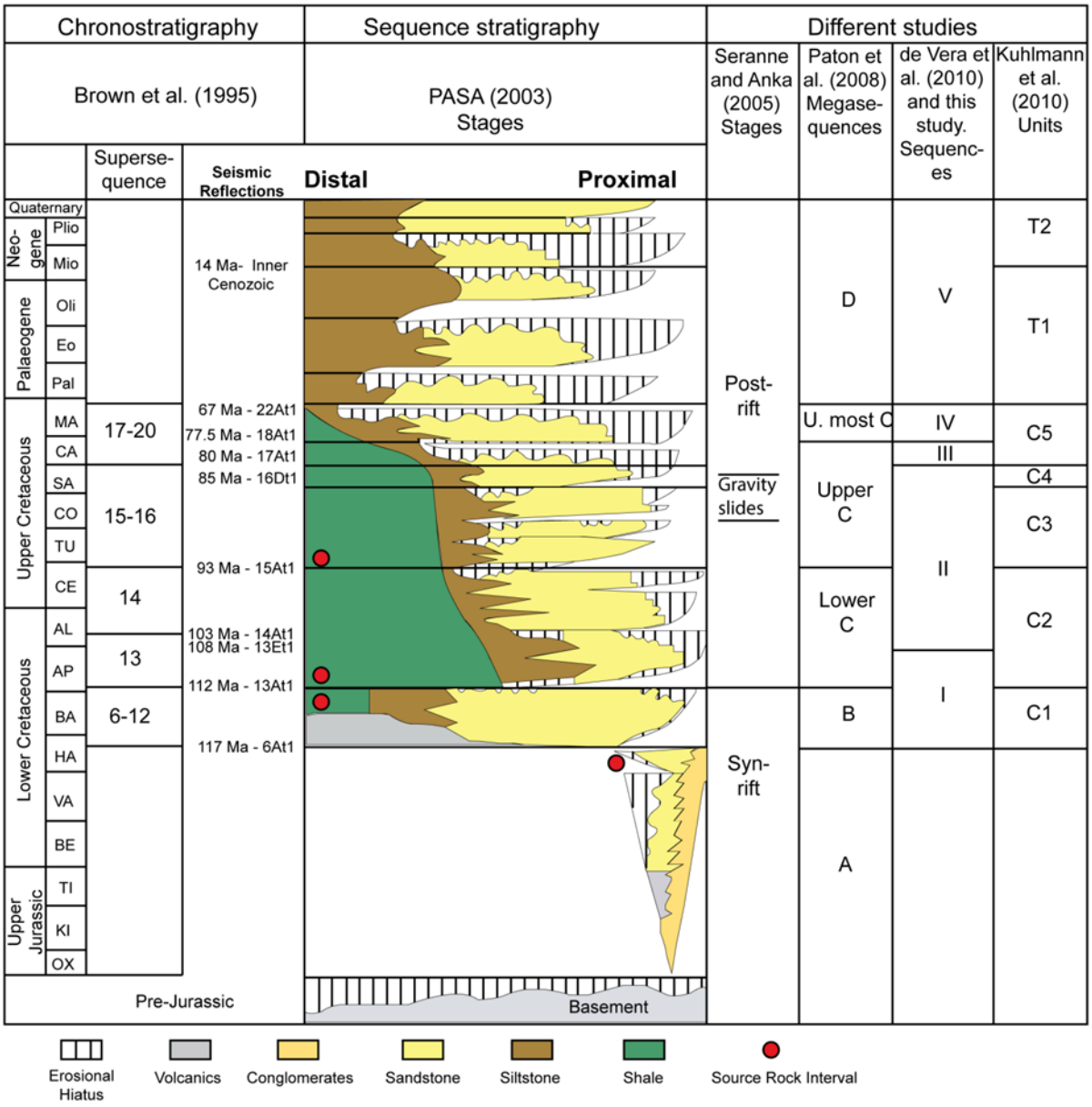


Figure 2.1. Chronostratigraphy and sequence stratigraphy of the Orange Basin illustrating the major stratigraphic units and unconformities based on various studies. 6-12, 13, 14, 15-16, 17-20 represent supersequences classified by Brown et al. (1995). OX (Oxfordian); KI (Kimmeridgian); TI (Tithonian); BE (Berriasian); VA (Valanginian); HA (Hauterivian); BA (Barremian); AP (Aptian); AL (Albian); CE (Cenomanian); TU (Turonian); CO (Coniacian); SA (Santonian); CA (Campanian); MA (Maastrichtian); Pal (Palaeocene); Eo (Eocene); Oli (Oligocene); Mio (Miocene) and Plio (Pliocene). A to D is the classification by Paton et al. (2008) used to group sequences from the Hauterivian to Holocene. I – V represents the classification by de Vera et al. (2010) used to group sequences from the Hauterivian to Holocene. C1 – C2 represents the classification used by Kuhlmann et al. (2010) to group sequences from the Hauterivian to Holocene (after Seranne and Anka, 2005; Paton et al., 2008; de Vera et al., 2010; Kuhlmann et al., 2010; Boyd et al., 2011).

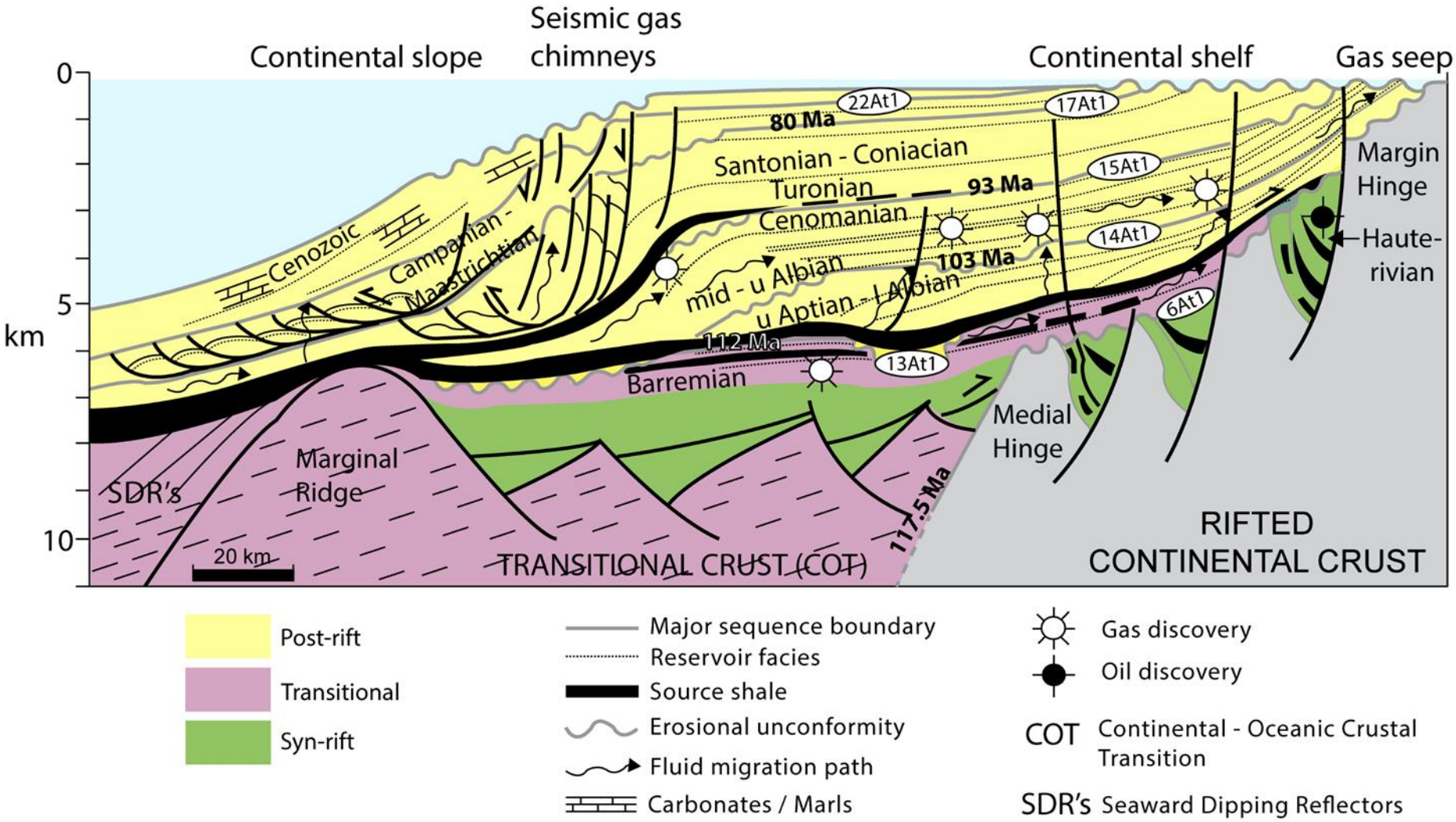


Figure 2.2. A schematic stratigraphic cross-section through the Orange Basin depocentre indicating the basin structure, sedimentary sequences and source rock intervals. 6At1, 13At1, 14At1, 15At1, 17At1 and 22At1 represent type-1 unconformities or subaerial unconformities classified by Brown et al. (1995). 6At1 (drift onset unconformity); 13At1 (Mid-Aptian unconformity); 14At1 (Albian unconformity); 15At1 (Cenomanian unconformity); 17At1 (Maastrichtian unconformity) and 22At1 (Palaeogene unconformity) (modified from Jungslager, 1999).

2.2. Structural setting

From the Late Cenomanian, the continental margin was affected by gravity slumping indicated by the development of extensional growth faults, large-scale slumping, toe-thrust faults and fault-related folds on the slope (Brown et al., 1995; Seranne and Anka, 2005; Broad et al., 2006; de Vera et al., 2010; Kuhlmann et al., 2010) . As previously stated, these structures are collectively referred to as post-rift gravity-driven systems. Numerous gravity-driven systems have been recorded in post-rift sequence II (Figure 2.2). Post-rift sequence II is an unconformity bounded sedimentary deposit consisting of relatively conformable successions of genetically related strata of Mid-Aptian to Santonian age (Van Wagoner et al., 1987; Van Wagoner et al., 1988; Brown et al., 1995; de Vera et al., 2010; Catuneanu et al., 2011). The gravity-driven systems can be separated into three characteristic structural domains based on their contrasting structural styles (de Vera et al., 2010). The gravity-driven systems can be separated into an extensional domain characterised by basinward-dipping listric faults that sole into a basinward-dipping detachment fault, a transitional domain that is characterised by both extensional and compressional faults, and a contractional domain that is dominated by thrust faults dipping landward and asymmetric basinward-verging fault-related folds (Granado et al., 2009; de Vera et al., 2010; Figure 2.3).

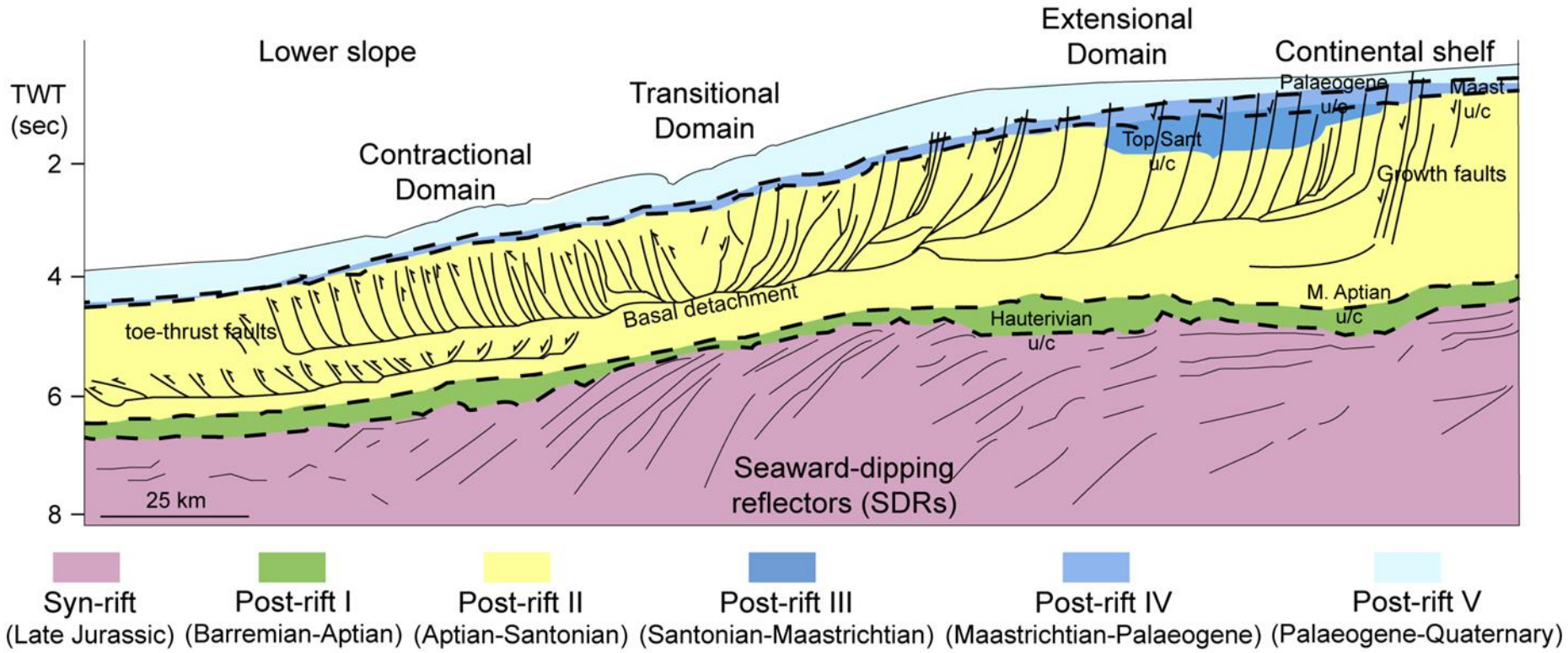


Figure 2.3. A schematic cross-section illustrating the main post-rift sequences (I-V) and the Cretaceous gravity-driven system in post-rift sequence II. The gravity-driven system is characterised by landward-dipping thrust faults and basinward-dipping growth faults that sole into a common detachment. u/c represents unconformity. The Santonian is abbreviated as Sant and the Maastrichtian as Maast (modified from de Vera et al., 2010).

Dingle (1980) identified four cycles of gravitational slumping. Cycle one is associated with deposition of Upper Cretaceous sediments and Cretaceous slumping; cycle two is associated with rapid deposition of Upper Cretaceous sediments coeval with slumping and thrust faulting; cycle three is associated with steady Palaeogene sedimentation and outward progradation of the margin, the rotation of large blocks of consolidated sediment and mass movement of unconsolidated material caused by slumping, and burial of slump deposits by additional deposition of suspended sediment. The final cycle, cycle four, is associated with sedimentation and progradation of the continental slope in the Quaternary. Depositional sequence II, in which the gravity-driven systems are recorded, corresponds to cycle one (Kuhlmann et al., 2010).

The Cretaceous gravitational slumping occurred in the proto-South Atlantic Ocean with increased rates of discharge of the Orange River and fast rates of tectonic subsidence. It is related to two shale units that formed detachment surfaces. These units are of Cenomanian to Turonian and Campanian ages. The listric faults that develop in the extensional domain only develop above the dipping Cenomanian to Turonian detachment surface (Seranne and Anka, 2005; Kuhlmann et al., 2010). Gravitational collapse of the margin during the Cretaceous occurred as short-lived episodic events (de Vera et al., 2010).

Gravity slumping is not limited to the Cretaceous successions. It has also been recorded in the Cenozoic successions. Cenozoic slumping occurred at a time when sedimentation rates were slow and the rate of thermal subsidence was decreasing. The slumping is associated with a shale unit that formed a detachment surface at the base of the Palaeogene (Seranne and Anka, 2005; Kuhlmann et al., 2010). Slumping occurred as a result of reactivation of older growth faults and toe-thrust systems located on the outer edge of the continental margin (Hirsch et al., 2010; Kuhlmann et al., 2010). Based on these observations, Kuhlmann et al. (2010) proposed that the Cenozoic sequence corresponds to cycle three of gravitational slumping. In addition, Wigley and Compton (2006) proposed that slumping during the Cenozoic occurred as a result of margin uplift along the western margin of southern Africa between 17

and 18 Ma. Renewed uplift along the western margin in the Pliocene resulted in westward tilting of the subcontinent. This triggered a second slumping event.

Numerous models have been proposed to explain the cause of margin instability and gravitational failure. The gravity-driven systems of the Orange Basin are characterised by strongly asymmetric fault-related folding; an absence of landward-dipping syn-depositional faults in the extensional domain and the presence of a thin,discrete frictional décollement (Granado et al., 2009; de Vera et al., 2010). The geometry of the gravity-driven systems provides insight into the mechanisms responsible for gravitational failure of the basin margin. The geometry of the gravity driven systems and the short-lived, episodic nature of gravitational failure provides evidence for gravity sliding as the principal mechanism for gravitational failure (de Vera et al., 2010). Gravity sliding is defined as the component controlled by the dip of the detachment and it is also referred to as gravity gliding. Gravity sliding occurred episodically from the Cenomanian to the Campanian. This is supported by the imaging of stacked gravitational failures separated from the undeformed layers in the seismic data. Numerous factors, which include a dipping basin slope, cratonic uplift and the generation of hydrocarbons, facilitated gravity sliding (de Vera et al., 2010). The generation of hydrocarbons in the Cenomanian-Turonian source rocks, which coincide with the décollement of the main gravity-driven system, induced an increase in pore fluid, resulting in decreased friction at the base of the detachment (de Vera et al., 2010). Additionally, cratonic uplift may have increased the dip of the basin slope and as a result favoured gravity sliding. The Cretaceous and Cenozoic gravity slumping events are related to sea level fall followed by delta progradation. Delta progradation over the extensional domain decreased the gravitational potential and ceased gravity sliding (Granado et al., 2009; de Vera et al., 2010; Kuhlmann et al., 2010). However, Cenozoic delta progradation may have contributed to the reactivation of older growth faults in the extensional domain (de Vera et al., 2010).

2.3. Hydrocarbon migration

Hydrocarbon seepage is a process whereby hydrocarbons are released into the hydrosphere, atmosphere, or unconsolidated sediments. Hydrocarbon seepages or gas escape features have been documented along passive and active continental margins. Hydrocarbon seepage is expressed as pockmarks, mud volcanoes, carbonate/mud mounds, gas chimneys, bright spots and polygonal faults on reflection seismic data (Paton et al., 2007; Anka et al., 2014; Figure 2.4). These gas escape features have been observed within the post-rift sequences on the continental shelf (Paton et al., 2007; Kuhlmann et al., 2010; Boyd et al., 2011; Anka et al., 2014). In seismic sections, vertical migration and accumulation of gas is indicated by bright spots and acoustic blanks. The gas appears to have moved freely through the sedimentary succession and is not associated with faults (Kuhlmann et al., 2010). Kuhlmann et al. (2010) identified gas chimneys that originated from deep sedimentary layers and terminate on the seafloor or below horizon 22At1 (Figure 2.2). These gas chimneys occur in areas with shallow water depths of 400 m. The origin of gas is attributed to deep thermogenic hydrocarbon sources and gas hydrate dissociation (Paton et al., 2007; Kuhlmann et al., 2010). In marine settings, gas migration to sedimentary boundaries or the seafloor is attributed to changes in pressure or temperature, resulting in dissociation of gas hydrates. Tectonic movement and submarine mass movement have been suggested as possible processes that cause gas migration (Hartwig, 2014). Additionally, gas migrating from the source rock to overlying sediments can cause margin instability by increasing the pore fluid pressure within the sediments. This weakens the sediments and subsequently causes liquefaction, resulting in mass movement of sediment downslope (Rowan et al., 2004; Bünz et al., 2005).

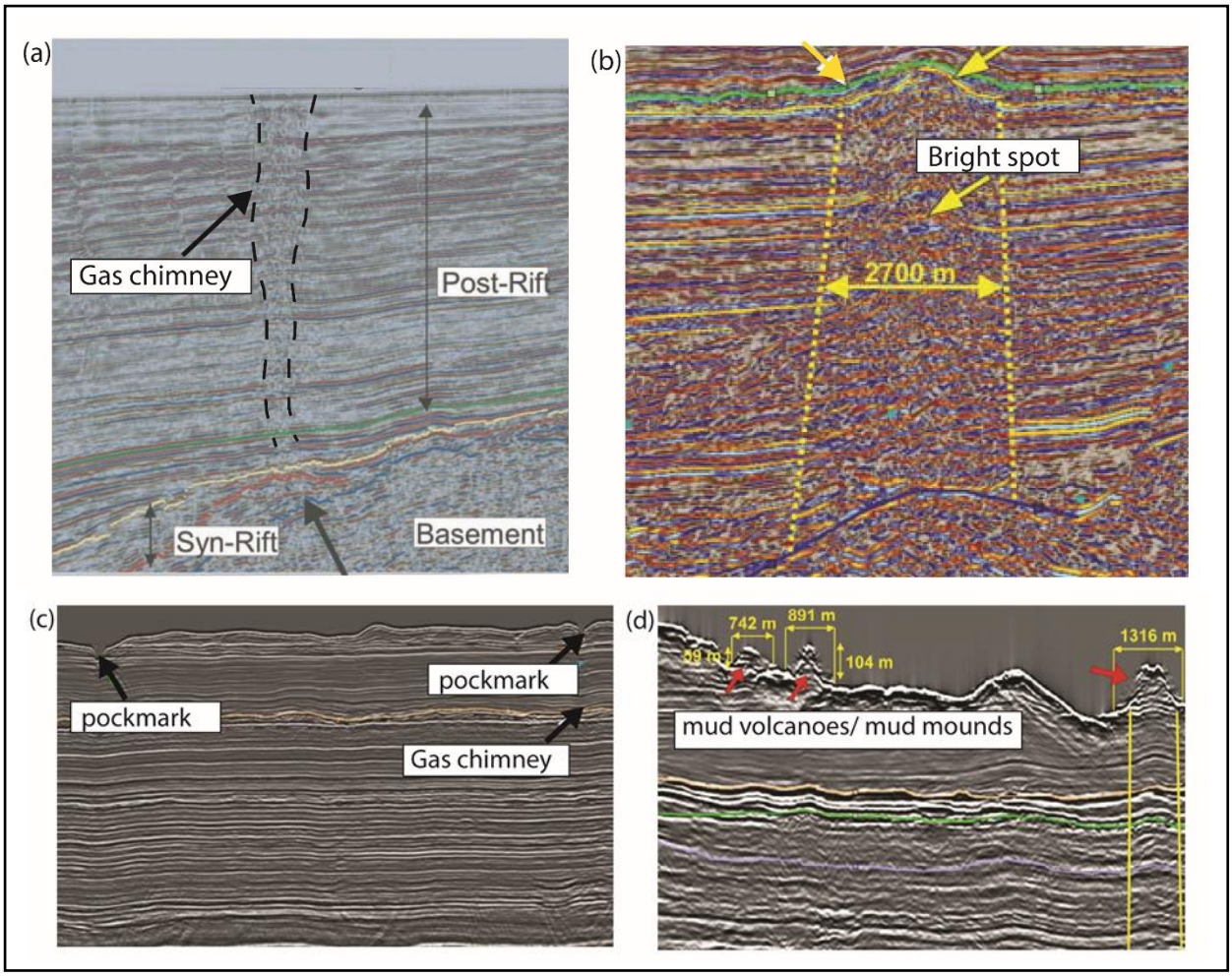


Figure 2.4. Seismic sections illustrating examples of gas escape features. (a) Gas chimney outlined by dashed black lines. (b) Yellow arrows indicating bright spots. (c) Gas chimney feeding pockmark. (d) Mud volcanoes or Mud mounds indicated by red arrows (Paton et al., 2007; Anka et al., 2014).

3. REVIEW OF 3D REFLECTION SEISMIC METHOD

3.1. Background

Since the 1920s reflection seismology has been used for hydrocarbon exploration (Sheriff and Geldart, 1995). The advantage of the reflection seismic technique is that it is able to image large areas, therefore allowing consideration of the extensive architecture of depositional and deformation units (Bull and Cartwright, 2010). In recent years it has been used for exploration in hard-rock terranes and to image deeply seated large-scale and small-scale features in the shallow and deep subsurface environments (Salisbury et al., 2003; Schmelzbach, 2007). In South Africa, it has been applied for gold and platinum mine planning and design (Manzi et al., 2012a). The reflection seismic method is not only used offshore for prospecting of hydrocarbons, it is also used to understand shelf and slope sedimentology and tectonics. The interpretation of subsurface features will allow the interpreter to infer the deformation mechanisms that influenced basin development and unravel the geological history of offshore basins.

3.2. Acquisition

In the reflection seismic method, energy is released from a source and travels as seismic waves into the subsurface. Some of the energy is reflected back to the recording sensors that measure the magnitude of the energy and the direction from which the reflected waves arrive (Dentith and Mudge, 2014). The speed at which each wave travels is determined by the physical properties of the subsurface strata (Davies and Austin, 1997; Liner, 2016). The seismic waves are reflected at lithological and structural boundaries where there is a change in the physical properties of the rocks (Dentith and Mudge, 2014; Liner, 2016; Figure 3.1). This physical property, called acoustic impedance, is defined by the product of the bulk density (ρ) and seismic wave velocity (V). The greater the difference in the acoustic impedance, the greater the amount of incident energy that is reflected (Dentith and Mudge, 2014). The ability to generate a strongly reflective boundary is dependent on the reflection coefficient, the boundary thickness and the geometry of the target (Dentith and Mudge, 2014; Liner, 2016). The reflection

coefficient is described as the amount of energy reflected. A reflection can be recognised when the acoustic impedance contrast produces a reflection coefficient of at least 0.06 (6% of incident energy) (Dentith and Mudge, 2014).

In marine surveys, an array of airguns release pulses of compressed air into the water (Figure 3.1). The energy from the airguns is released at slightly different times to control the frequency and energy of the wavelet and to prevent the generation of air bubbles (Dentith and Mudge, 2014). The energy reflected off of an interface is recorded using hydrophones mounted in a waterproof tube (Figure 3.1). The array of airguns and streamers are towed at a shallow depth behind a moving ship (Handbury and Sorensen, 2013; Dentith and Mudge, 2014; Liner, 2016; Figure 3.1).

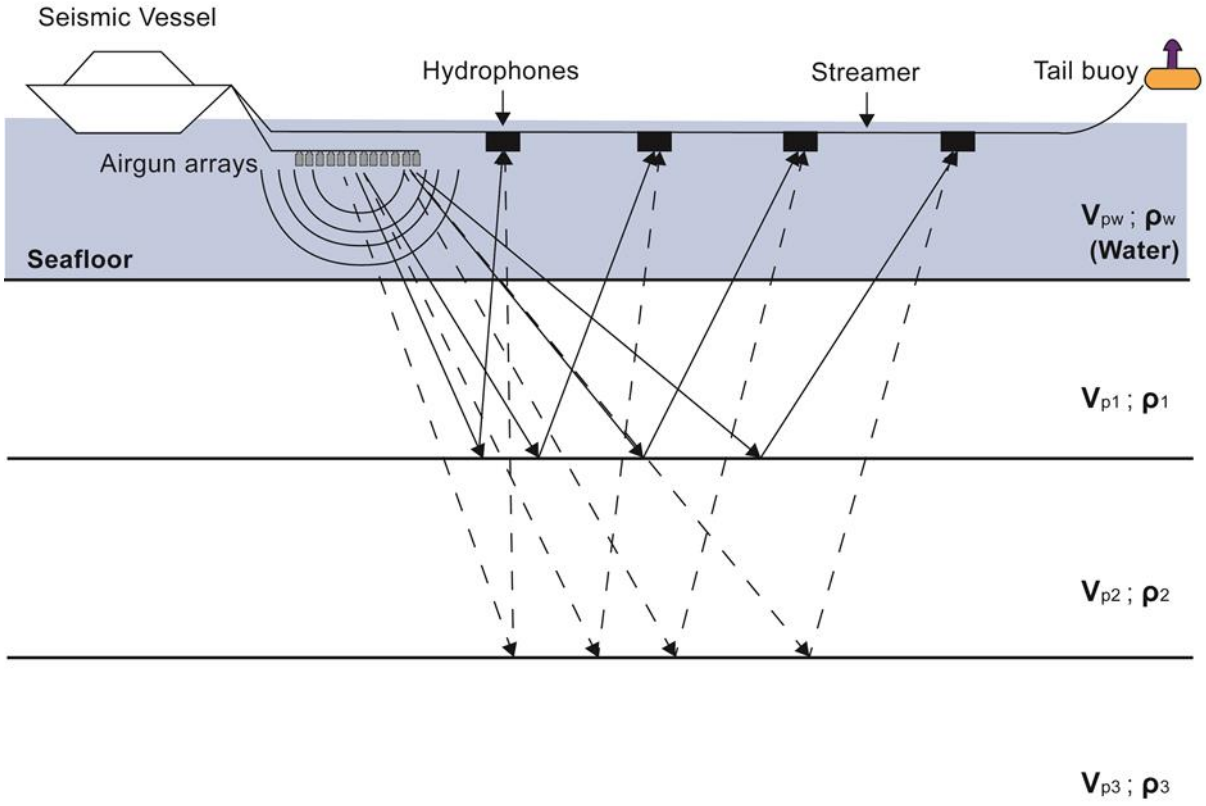


Figure 3.1. A Schematic diagram illustrating raypaths for reflections from interfaces. Vp represents the compressional waves and ρ represents the density. There is an acoustic impedance contrast across these interfaces, where $V_{p2}\rho_2 > V_{p1}\rho_1$ or $V_{p2}\rho_2 < V_{p1}\rho_1$ (After Thomas, 2015).

Some of the challenges encountered when conducting a seismic survey in deepwater environments are due to changes in the sea state. The sea state refers to the degree of turbulence at sea. A high level of turbulence results in sequences that are strongly affected by swell noise. The sea state will cause streamers to deviate from straight or parallel lines. This is referred to as cable feathering (Biondi, 2006; Handbury and Sorensen, 2013). Other challenges encountered include seismic interference caused by other seismic vessels shooting in the region and overlapping shots, which occur when the seismic vessel is travelling fast enough to reach the next shot position before the previous shot's record has expired, resulting in the direct arrival of the latest shot being recorded at the end of the previous shot record (Handbury and Sorensen, 2013).

Table 3.1 summarises the acquisition parameters for the deepwater Orange Basin 3D seismic survey.

Table 3.1. Acquisition parameters for the Orange Basin 3D seismic survey (Kramer and Heck, 2014).

Recording	
Recording format	SEG-D
Record length	7168 ms
Recording filter delay	None
Sample rate	2 ms
Low cut filter hydrophone, slope	4.4 Hz, 12 dB / octave
Low cut filter geophone, slope	Not applicable
High cut filter both, slope	214 Hz, 341 dB / octave
Source	
Source type	Dual source
Number of source arrays	2
Number of sub-arrays	3
Shot point interval	25 m flip / flop +/- 500 ms dither source point interval
Array separation	100 m
Array length	15 m
Source volume	4100 cu in
Number of airguns / array	30
Operating pressure	2000 psi
Source depth	8 m
Nominal CMP fold	80
Sercel SSAS Sentinel, Sercel Seal-428	
Number of streamers	8
Group interval	12.5 m
Group length	12.5 m
Number of hydrophones / group	1
Number of geophones / group	1
Streamer length	7950 m
Streamer separation	200 m
Number of groups / streamer	636
Streamer depth	10 – 15 m linear slant
Nearest offset	222 m

3.3. Processing

Seismic processing is the manipulation of the raw data to produce an image that can be used to infer subsurface geological information by reducing noise, migrating seismic reflections to their true subsurface locations and enhancing the wave signal (Manzi et al., 2013). There are four main primary stages in processing seismic data. These are noise attenuation (mainly deconvolution), velocity analysis, stacking and migration. Secondary processes are designed to improve the efficiency of deconvolution, stacking and migration. Velocity analysis is the calculation of stacking velocity or normal moveout (NMO) velocity from NMO measurements. It involves determining the velocity from selected common midpoint (CMP) gathers, which are a collection of seismic traces that share a common point that is halfway between the source and the receiver, referred to as a midpoint. NMO refers to the difference in reflection arrival time at a given offset and zero-offset (Sheriff, 2002). Deconvolution is a filtering process whereby a seismic wavelet is removed by undoing the process of convolution. This process is performed along the time axis to improve temporal resolution (Yilmaz, 2001; Lines and Newrick, 2004; Dentith and Mudge, 2014). Stacking of seismic traces increases the signal-to-noise ratio (S/N) of the data. Migration is a process whereby features on a stacked seismic section or shot gathers are moved to their correct subsurface positions, resulting in improved lateral resolution (Yilmaz, 2001; Dentith and Mudge, 2014). The Kirchhoff algorithm was used for the migration of the deepwater Orange Basin 3D seismic data. The Kirchhoff migration method sums the amplitudes along a diffraction hyperbola and places the summed amplitude on the crest of the diffraction hyperbola. This method is the most commonly used migration in the petroleum industry for velocity analysis, depth and time imaging (Yilmaz, 2001; Sheriff, 2002; Dentith and Mudge, 2014). The deepwater Orange Basin 3D seismic data were migrated before stacking (prestack migration) using the Kirchhoff algorithm. The Kirchhoff prestack migration has been used in a number of petroleum studies and it has been successful in enhancing the data quality by mapping steeply dipping stratigraphy and complex faulting characterised by strong lateral velocity variations, compared to poststack migration (Yilmaz, 2001; Kramer and Heck, 2014) .

Some of the challenges encountered when processing marine seismic data include multiples, which are arrivals that have been reflected more than once; ghost reflections, which occur as a result of downward reflection off the sea surface and multi-pathing, where several seismic arrivals from the same horizon are recorded at the surface locations due to rapid lateral variations in the velocity model. These result in poor resolution and image quality (Rekdal and Long, 2006; Dentith and Mudge, 2014; Yilmaz and Baysal, 2015).

Processing of the data from the deepwater Orange Basin Licensing Area (OBDWLA) was done by the Global Processing team in Netherlands on behalf of Shell South Africa Upstream B.V. as part of a project on 3D seismic processing and prestack seismic imaging (i.e., prestack migration) for exploration purposes. The pre- and full processing steps included: geometry setup, data conversion (SegD to SegY), trace editing, first break picking, static correction, noise attenuation, velocity analysis, stacking, deconvolution and migration. Outlined in Figure 3.2 is the processing flow that was applied to the Orange Basin 3D seismic data.



Figure 3.2. Processing flow used to process the Orange Basin 3D seismic data. The green box shows processing done by Dolphin Geophysical Polar Duchess. The blue boxes show processing done using SIPMAP (Kramer and Heck, 2014).

3.4. Seismic resolution limit

The minimum distance required to distinguish two reflecting points from one another is referred to as seismic resolution (Yilmaz, 2001; Lines and Newrick, 2004; Carrington, 2012; Dentith and Mudge, 2014; Liner, 2016). In reflection seismics there is vertical and lateral resolution, both controlled by signal bandwidth. The vertical resolution is the minimum distance required between two reflections, one at the top and another at the bottom of a layer, for them to be identified as individual points. When the layer has a thickness greater than or equal to a tuning thickness or a one-quarter dominant wavelength (i.e., $\lambda/_4$), the reflections are discernible (Yilmaz, 2001; Liner, 2016). The seismic wavelength (λ) is given by $v/_f$ where v is the mean velocity and f is the dominant frequency. In order to improve the vertical resolution, the wavelength is reduced by increasing the high-frequency content in the data through seismic deconvolution (Yilmaz, 2001; Lines and Newrick, 2004). Previous studies by Gibson et al. (2000), Jolley et al. (2007), Manzi et al. (2012a) and Manzi et al. (2012b) showed that the detection limit for data with a high signal-to-noise (S/N) ratio is given by $\lambda/_8$.

The lateral resolution is determined by the Fresnel zone for unmigrated, which is an area where seismic waves arrive at the surface within less than half wavelength (Sheriff, 1996; Liner, 2016). When a wave travels through the subsurface, it is not reflected from a single point on the reflector but rather from an area with characteristic dimensions. The radius of the Fresnel zone can be calculated using the following equation:

$$\frac{v}{2}\sqrt{t_0/_f} \tag{3.1}$$

where v is the velocity, t_0 is the two-way travel time and f is the dominant frequency (Yilmaz, 2001; Schmelzbach, 2007; Carrington, 2012). Reducing the width of the Fresnel zone through migration improves the lateral resolution (Yilmaz, 2001).

3.5. Interpretation

After processing, the seismic data are interpreted. Information acquired from seismic data is used to infer the subsurface geology. The information that can be obtained from seismic data includes geological structures (such as lithological boundaries, unconformities and faults) and physical properties. The conventional interpretation of reflection seismic data is based on the identification and picking of strong seismic reflectors on every inline and crossline on seismic sections. The shortfall with the conventional interpretation is that it does not allow for better delineation of geological features below the seismic resolution limit (i.e., one-quarter dominant wavelength). However, seismic attributes can be used to enhance and detect these features in the data (Dentith and Mudge, 2014).

Mapping of subtle faults is of importance in hydrocarbon exploration. Faults may act as seals or conduits, allowing fluid flow along fault networks (Randen et al., 2001). Comprehensive knowledge of fault systems may thus provide useful information on structures along which hydrocarbons migrate and accummulate.

3.5.1. Conventional 3D seismic interpretation

The conventional interpretation of 3D reflection seismic data is a qualitative process that involves the identification and mapping of reflective horizons and large-scale faults (Dentith and Mudge, 2014). These horizons may represent changes in lithology, unconformities, or the upper and lower contacts of mineralised units. The most commonly used seismic attribute to identify horizons and faults present in the seismic data is amplitude. The amplitude is dependent on a contrast in acoustic impedance across an interface and thus provides information on the changes in lithology. The reflective horizons are identified as maximum positive (peak) or maximum negative (trough) amplitudes on the seismic sections. Data polarity determines whether a horizon is picked as a peak or trough. In the American standard of picking, a peak marks an increase in acoustic impedance across an interface while a trough marks a decrease in acoustic impedance (Bacon et al., 2003; Brown, 2011).

3.5.2. Autotracking and manual picking

Picking is an interpretation process whereby a reflective horizon is tracked on seismic sections through the use of interpretation software packages. This can be done manually or automatically (autotracking) depending on the data quality and continuity of the horizon (Herron, 2011; Herron, 2014).

The autopicking technique uses a computer algorithm to accurately and efficiently pick the peak amplitude along the horizon. The interpreter sets parameters that control the effectiveness of the algorithm. These parameters are dependent on the data quality. Once the autotracking parameters have been set, the interpreter plants seed points along the selected horizon in the inlines and crosslines. The seed points serve as starting points from which correlations will be made using the selected autotracking parameters (Bacon et al., 2003; Herron, 2011). Once the horizon has been picked using autotracking, manual picking is implemented in regions of geological complexities and poor signal-to-noise ratios in the data, resulting in a detailed structural interpretation (Herron, 2014).

3.6. Seismic attributes

The term seismic attribute refers to measurements taken on a seismic trace or a surface interpreted from seismic data (Bacon et al., 2003). Seismic attributes are used to enhance the mapping of features on seismic data that are below the seismic resolution limit, resulting in a more accurate interpretation of geological features (Liner, 2016). However, noise can affect the quality of the image produced by the seismic attribute. The attributes applied in this study are grouped into two categories: horizon-based seismic attributes and volumetric seismic attributes. The horizon-based attributes are amplitude, dip, dip azimuth and edge detection, and the volumetric attributes are edge enhancement and ant tracking (Brown, 1996; Brown, 2001; Randen et al., 2001; Marfurt and Chopra, 2007).

3.6.1. Horizon-based seismic attributes

Amplitude

The amplitude attribute is the most commonly used attribute to interpret horizons and faults on seismic data (Brown, 2011). It is dependent on a difference in acoustic impedance across a boundary and thus provides information on the changes in lithology. Additionally, it can provide information on porosity and porefill (Bacon et al., 2003). A limitation of this attribute is that it fails to image small-scale lithological changes in thin beds (i.e., layers with thickness below the tuning thickness) and small-scale faults which are below the seismic resolution limit.

Dip and dip azimuth

Dip and dip azimuth refer to the magnitude and direction, respectively, of the gradient vector calculated at each sample point of the interpreted horizon (Mondt, 1993). The calculations are done by fitting a plane through neighbouring data points and placing the computed values at the central data point (Rijks and Jauffred, 1991). The mathematical expressions of dip and dip azimuth are as follows:

$$dip\ magnitude = (s_x{}^2 + s_y{}^2)^{1/2} \tag{3.2}$$

$$dip\ azimuth = \arctan(^{s_x}/_{s_y}) \tag{3.3}$$

where s_x and s_y are components of dip in the x and y direction, respectively (Marfurt and Chopra, 2007).

Calculating dip and dip azimuth on an interpreted seismic horizon is useful for revealing small scale faults that would be less noticible on migrated seismic sections. The effectiveness of dip and dip azimuth in fault detection is dependent on the fault dip differing from the horizon dip. Additionally, the dip direction of the fault should differ from that of the horizon to allow detection of faults using the dip azimuth attribute. The edge detection attribute, which is a combination of dip and dip azimuth variations, is applied to overcome limitations of dip and dip azimuth attributes (Manzi et al., 2012b).

Edge detection

The edge detection algorithm uses a combination of dip and dip azimuth variations that are normalised to the local noise of the interpreted horizon to detect local changes in the image intensity, associated with discontinuities (Randen et al., 2001; Manzi et al., 2012b). The edge detection technique can be used for better detection of small-scale faults and fault complexities, such as fault continuity and interconnectivity of faults, by manipulation of the colour bar. The edge detection attribute is a more powerful tool in highlighting complex structural detail on horizons when compared to dip and dip azimuth attributes (Manzi et al., 2012b).

3.6.2. Volumetric seismic attributes

Edge enhancement

The edge enhancement attribute accentuates edges (faults) and horizons by computing the changes in the signal amplitude. Local dip estimates of the reflection surfaces are used to reduce noise and enhance changes along the reflective surfaces (Randen et al., 2001; Randen and Sønneland, 2005). This attribute smooths the data, without adding artifacts, while reducing the noise and thus permits the detection of minor amplitude changes (Randen and Sønneland, 2005). This attribute is applied to the seismic volume to reduce noise before the ant tracking attribute is applied.

Ant tracking

Ant tracking is a fault detection technique that uses a series of seismic attributes in a workflow to detect and map faults and fracture networks throughout a 3D seismic volume (Cox and Seitz, 2007). The ant tracking workflow begins with the application of structural smoothing filters such as a Gaussian filter, which removes noise while preserving the fault, followed by the application of enhancement attributes (Solihulhadi and Tolioe, 2007; Ngeri et al., 2015). The ant tracking method uses the concept of swarm intelligence, where ants find the most efficient route between their nest and food, and they communicate with colony members through the release of pheromones (Marfurt and Chopra, 2007; Ngeri et al., 2015). Similarly, in the Petrel software package, electronic ants follow discontinuities to

detect and enhance fault and fracture networks. The ant tracking method provides the interpreter with a more accurate and unbiased mapping of fault networks and horizons (Cox and Seitz, 2007).

4. METHODOLOGY

4.1. Seismic interpretation

3D seismic data from the deepwater Orange Basin Licence Area (OBDWLA) (Figure 4.1) was interpreted using advanced seismic interpretation software packages (IHS Kingdom Suite software and Petrel E&P software platform). These software packages were used for complex modelling of geological structures as well as enhancing the visualization of faults and stratigraphic units.

Acquisition and processing of the data were undertaken by Shell Global Solutions International B.V. The data have been interpreted using the IHS Kingdom Suite software by creating a polygon to isolate the area of interest (400 km^2) from the whole seismic area (8000 km^2) (Figures 4.1 and 4.2). Strong and laterally continuous seismic reflectors, faults and stratigraphic unconformities were tracked and manually picked along each inline and crossline section, for a detailed interpretation. Vertical sections through the data that are parallel to the acquisition direction are referred to as inlines and those perpendicular to the acquisition direction are referred to as crosslines (Morley, 2009a). The seismic reflectors are identified as maximum positive (peak) or maximum negative (trough) amplitudes on the seismic sections. In the initial phase of interpretation, wide line spacing was used to pick the peak of the reflectors. Every 50^{th}, 20^{th} and 10^{th} inline and crossline within the polygon was picked. Once that was completed, the peaks of the reflectors were picked on every inline and crossline to ensure that no lines were skipped. After picking the reflectors, faults were picked. The faults are identified as areas where there is displacement of reflectors. Faults were initially picked on every 5^{th} inline. To ensure that small faults were not skipped during fault picking, every inline and crossline was interpreted. In structurally complex areas where the S/N ratio is low, careful picking of reflectors and faults is paramount for constructing an accurate 3D regional model. This chapter details the reflection seismic methods used to interpret the OBDWLA seismic data.

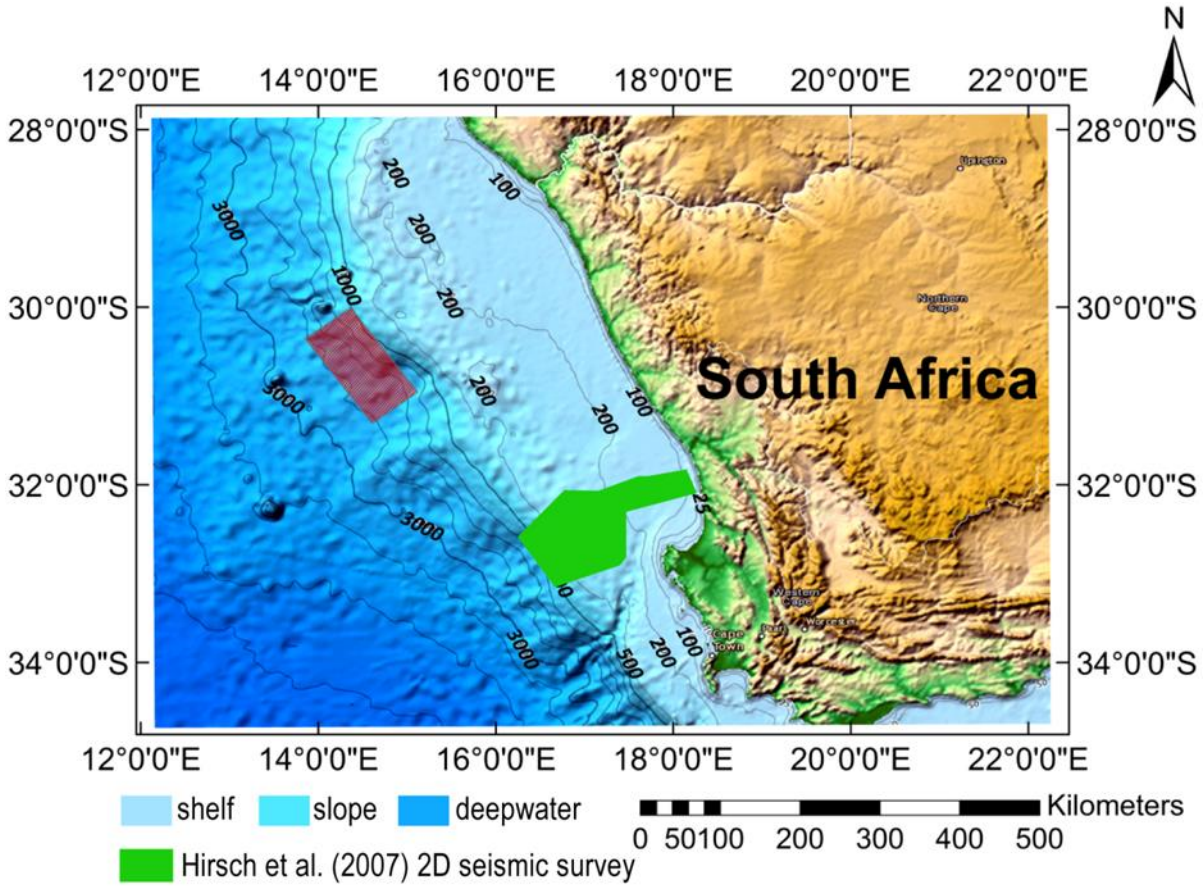


Figure 4.1. Bathymetric map superimposed with the deepwater Orange Basin licence area indicated by the red polygon. The study area covers approximately 8200 km^2. The green polygon shows the 2D seismic survey used in a study by Hirsch et al. (2007). Borehole data used to calculate the densities of the rocks are found within the green polygon (basemap sourced from the National Oceanic and Atmospheric Administration, https://maps.ngdc.noaa.gov/viewers/bathymetry, March, 2017)

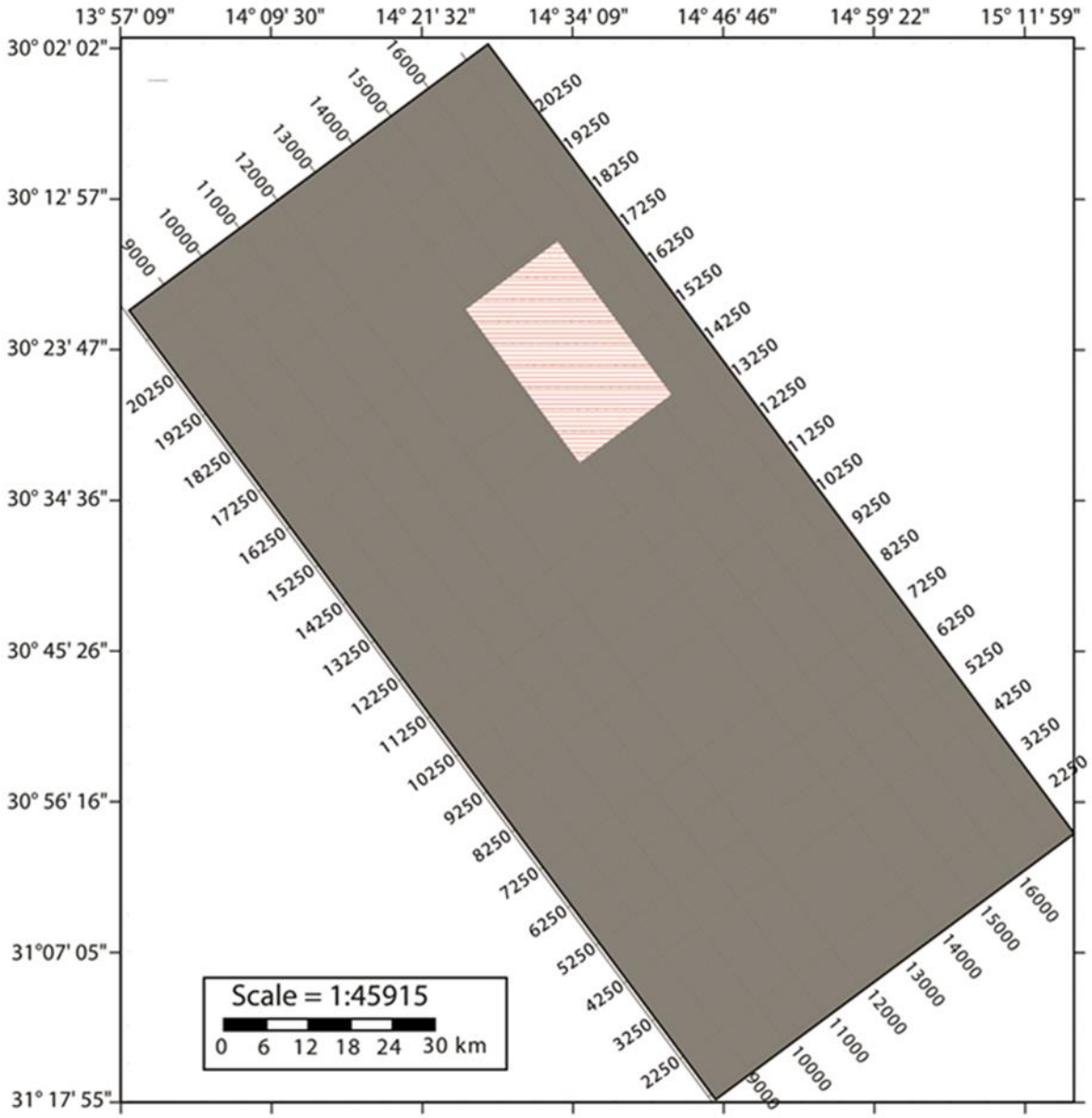


Figure 4.2. A survey map of the deepwater Orange Basin licence area showing inlines (parallel to acquisition direction) and crosslines (perpendicular to acquisition direction). The survey is 8000km^2. The 400km^2 study area is highlighted by the red polygon.

4.1.1. Horizon interpretation

The strong seismic reflectors were picked based on their geological significance. The Cenomanian-Turonian boundary, base of the Coniacian, Maastrichtian unconformity, base of the Palaeogene and Holocene (seafloor) were interpreted using 3D autotracking and manual picking. In structurally complex areas where the horizon was affected by complex faulting and areas with poor S/N

ratio, the horizon was picked manually. The American standard of picking, where the peak is given by an increase in acoustic impedance, was used for picking the horizons (Nietzsche, 2005). The seafloor horizon is well imaged due to a significant acoustic impedance contrast between water (Vp ~1518 m/s and ρ ~1.0 g/cm^3) and unconsolidated siltstones and sandstones on the seafloor (Vp ~1800 m/s and ρ ~1.7 g/cm^3) (Barrett and Froggatt, 1978; Hirsch et al., 2007; Kramer and Heck, 2014; Figure 4.3). The compressional seismic wave velocity (Vp) and density (ρ) increase from water to the seafloor unconsolidated sediments. This resulted in picking the seafloor as a "hard event" (i.e., peak). The base of the Palaeogene is well imaged due to the significant acoustic impedance contrast between the Palaeogene siltstones and sandstones (Vp ~2000 m/s and ρ ~1.7 g/cm^3) and Maastrichtian shales interbedded with siltstones and sandstones (Vp ~2500 m/s and ρ ~1.81 g/cm^3) (Barrett and Froggatt, 1978; Hirsch et al., 2007; Figure 4.3). The Maastrichtian unconformity is well imaged due to the major acoustic impedance contrast between Maastrichtian shales interbedded with siltstones and sandstones (Vp ~2500 m/s and ρ ~1.81 g/cm^3) and Santonian shales interbedded with siltstones and sandstones (Vp ~3000 m/s and ρ ~1.9 g/cm^3) (Barrett and Froggatt, 1978; Hirsch et al., 2007; Figure 4.3). The horizon at the top of the thrust fault system was picked to constrain the fault interpretation. The Santonian and Coniacian units consist of the same rock types, shales interbedded with siltstone and sandstone (see Figure 2.1). The horizon at the top of the thrust fault system is well imaged due to an acoustic impedance contrast between the Santonian units (Vp ~3000 m/s and ρ ~1.9 g/cm^3) and Coniacian units (Vp ~3000 m/s and ρ ~2.15 g/cm^3) (Barrett and Froggatt, 1978; Hirsch et al., 2007; Figure 4.3). The base of the Coniacian is well imaged due to the acoustic impedance contrast between Coniacian shales interbedded with siltsone and sandstone (Vp ~3000 m/s and ρ ~2.15 g/cm^3) and Turonian marine shales (Vp ~3800 m/s and ρ ~2.25g/cm^3) (Barret and Froggatt, 1978; Hirsch et al., 2007; Japsen, 2018; Figure 4.3). The Cenomanian-Turonian boundary is well imaged due to the acoustic impedance contrast between the Turonian marine shales (Vp ~3800 m/s and ρ ~2.25g/cm^3) and organic-rich shales at the Cenomanian-Turonian boundary (Vp ~4500 m/s and ρ ~2.52g/cm^3) (Hirsch et al., 2010; Qin, 2014; Japsen, 2018; Figure 4.3). No borehole data were available in the study area, therefore velocities found in literature were used and densities were inferred from those reported by Hirsh et al. (2007) on the continental margin (see Figure 4.1). The seismic sections were initially interpreted using wide line spacing. Every

50^{th}, 20^{th} and 10^{th} inline and crossline was picked within the polygon. Once the wide grid of picks was completed, infill picks were made on every inline and crossline to ensure that no lines were skipped, resulting in a detailed structural interpretation.

The ages of the stratigraphic boundaries were inferred from previous work (de Vera et al., 2010) conducted in the Orange Basin. The seismic character of the units was compared with the seismic character of the units documented in the compressional domain in de Vera et al. (2010) (see Figure 2.3). The Coniacian to Santonian units are characterised by basinward-verging reflectors that have been disrupted by the landward-dipping thrust system (Figure 4.3), this has only been recorded in the Coniacian to Santonian units of the Orange Basin. The base of the Maastrichtian units (Maastrichtian unconformity) is characterised by a high-amplitude seismic reflector package and termination of seismic reflections below the unconformity (de Vera et al., 2010; Figure 4.3). The base of the Palaeogene and Cenomanian-Turonian interfaces were determined by Shell Global Solutions International B.V, using the velocities of the sediments (Kramer and Heck, 2014).

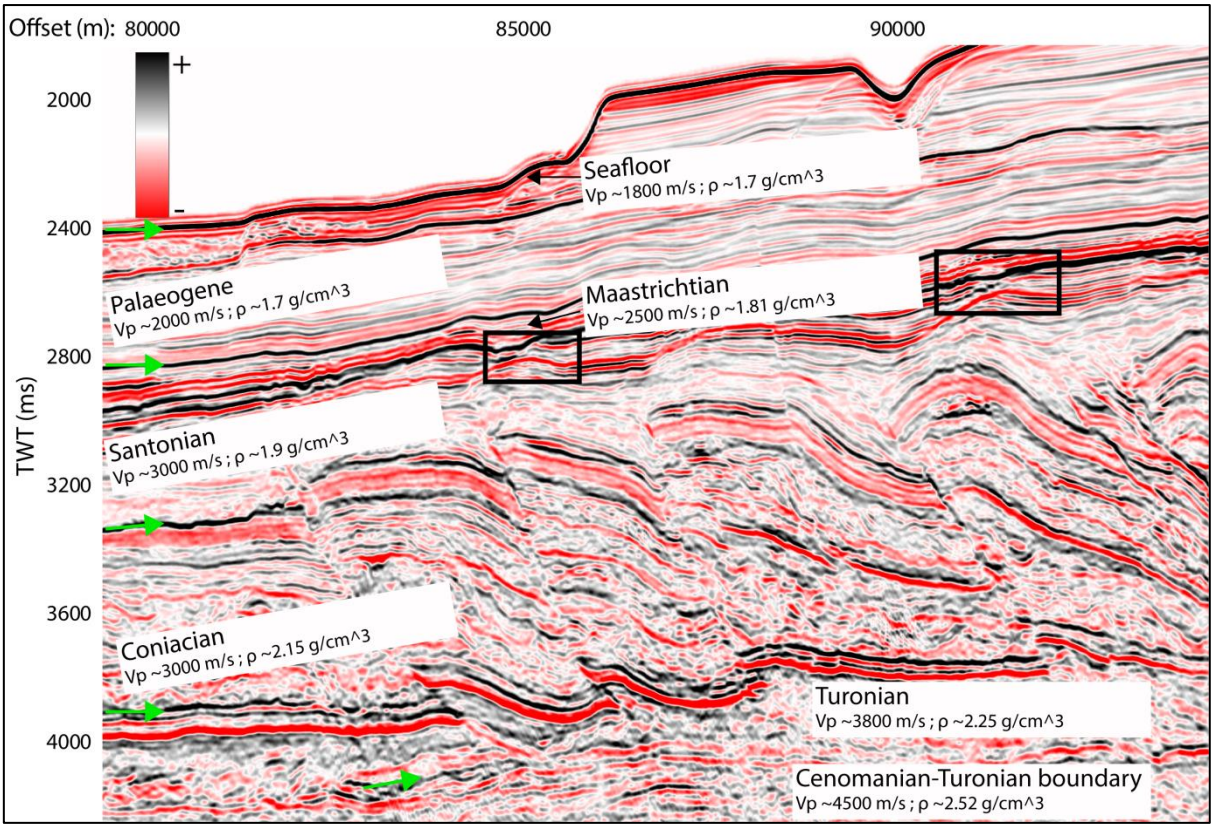


Figure 4.3. An amplitude display seismic section showing velocities (m/s) and densities (g/cm^3) of the stratigraphic units. The green arrows indicate the picked interfaces that produce strong reflections. The Cenomanian-Turonian boundary is discontinuous. The black boxes highlight areas where reflectors terminate below the Maastrichtian unconformity. The vertical exaggeration (VE) of the section is 8: 1.

4.1.2. Fault interpretation

Faults were identified in the seismic data as areas where there were terminations of the seismic reflector and displacement of the reflector on the opposite side of the fault plane (Dentith and Mudge, 2014). Distinguishing normal and reverse faulting was done by observing the type of displacement of the hangingwall and footwall blocks. With normal faults, the hangingwall rocks are downthrown and with reverse faults, the hangingwall rocks are displaced upwards relative to the footwall rocks (Davis and Reynolds, 2011). The folds associated with the faulting are characterised by changes in the dip of the reflector. In order to resolve faults on a seismic section, the vertical displacement of the faults should be greater than or equal to one quarter of the dominant wavelength $\lambda/4$ (Carrington, 2012; Manzi et al., 2013; Dentith and Mudge, 2014). However, faults below this limit can be detected using seismic attributes. The detection limit can be defined by $\lambda/8$ for seismic data with high S/N ratio. For this study,

the dominant frequency reported in the seismic acquisition and processing report is 50 Hz. Using the reported average seismic velocity of 2400 m/s and the dominant frequency of 50 Hz, the wavelength of the data is 48 m. Using the above wavelength for the detection limits of $\lambda/4$ and $\lambda/8$, the resolution limits are 12 m and 6 m, respectively. Therefore, geological features below the vertical resolution limit of 12 m are not directly resolved on the amplitude display sections.

The first- and second-order scale thrust faults were picked using the conventional interpretation methods, along every inline and crossline. In this study, first-order scale faults are faults with a vertical displacement of 40 m to 300 m and second-order scale faults are faults with a vertical displacement between 12 m and 40 m. Picking of the normal faults, identified in the Maastrichtian and Palaeogene units, using the conventional interpretation methods proved to be challenging due to changes in vertical displacement along fault strike. In some parts of the study area, the displacement decreased below the vertical resolution limit along the strike of the fault. These third-order scale faults, which have a vertical displacement of less than one-quarter of the dominant wavelength, were detected through attributes analysis.

4.1.3. Data conditioning

Surface smoothing

The seafloor, base of the Palaeogene and Maastrichtian unconformity horizons have continuous and strong reflectors with minimal deformation. The Coniacian to Santonian sequences were deformed by the thrust faults and the Cenomanian-Turonian horizon is highly discontinuous. The northern portion of the study area is structurally complex and has a low S/N ratio (Figure 4.4). The horizons in this part (indicated by the dashed blue box) of the study area were manually picked (Figure 4.5). Manual picking is used in areas where the reflectors are unclear due to complex geology or poor S/N ratios. The disadvantage of using this mode of picking is that in poor S/N areas, where the reflector continuity is unclear, there are inconsistencies in picking (mispicks). Manual picking can also generate noise (Figure

4.6a). Smoothing (gridding) of the surface is used to interpolate over areas with poor S/N ratios and to smooth anomalous picks. Two types of gridding methods were used; the Gaussian and Kriging methods (Childs, 2004; Brett, 2016). Gaussian and Kriging are interpolation methods used to determine an unknown value at a given location. The Gaussian method was used to smooth the seafloor (Figure 4.6b), base of Palaeogene and Maastrichtian unconformity horizons. The Gaussian method removes the high-frequency background noise and computes the weighted average of each neighbouring point, with the weighted average more towards the central points (Brett, 2016). The Kriging method was used to grid the horizons at the top and base of the Coniacian-Santonian thrust system (Figure 4.7a-b) and the Cenomanian-Turonian horizon. This method derives an average value for an unmeasured point based on the known data points neighbouring this point. This method of gridding works well in areas with sparse data points (Childs, 2004).

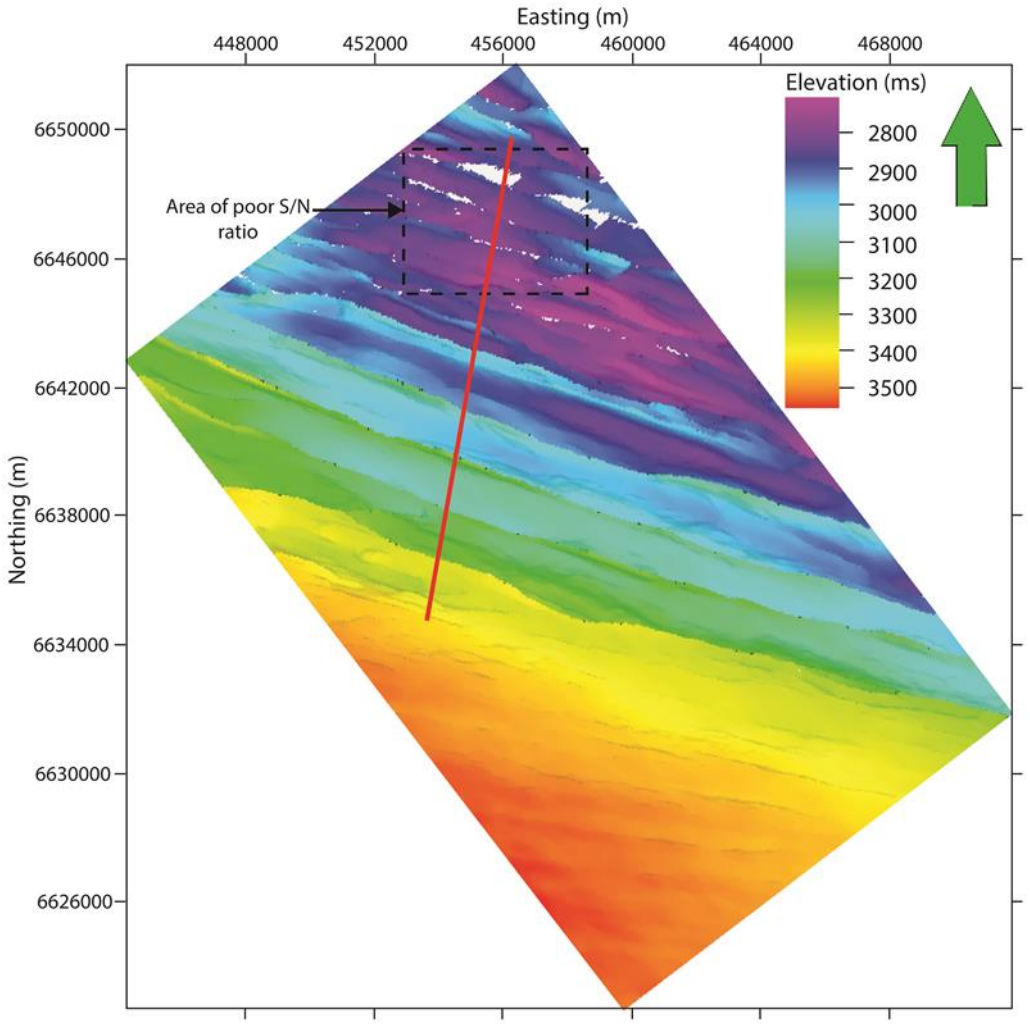


Figure 4.4. A depth structure map of the horizon at the top of the thrust fault system (base of the Santonian) highlighting an area with low signal-to-noise ratio (indicated by the dashed box). The red line indicates an arbitrary line that passes through the area of low signal-to-noise ratio presented in Figure 4.5.

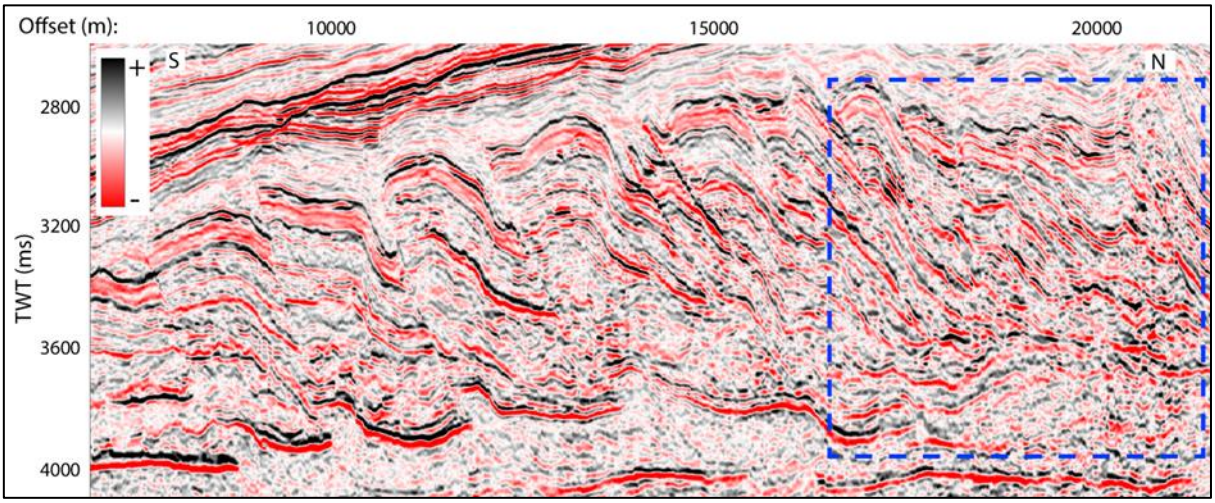


Figure 4.5. An amplitude seismic section showing the structurally complex area with low signal-to-noise ratio in the NE portion of the study area. This area is highlighted by the blue dashed box. The vertical exaggeration (VE) of the section is 8:1.

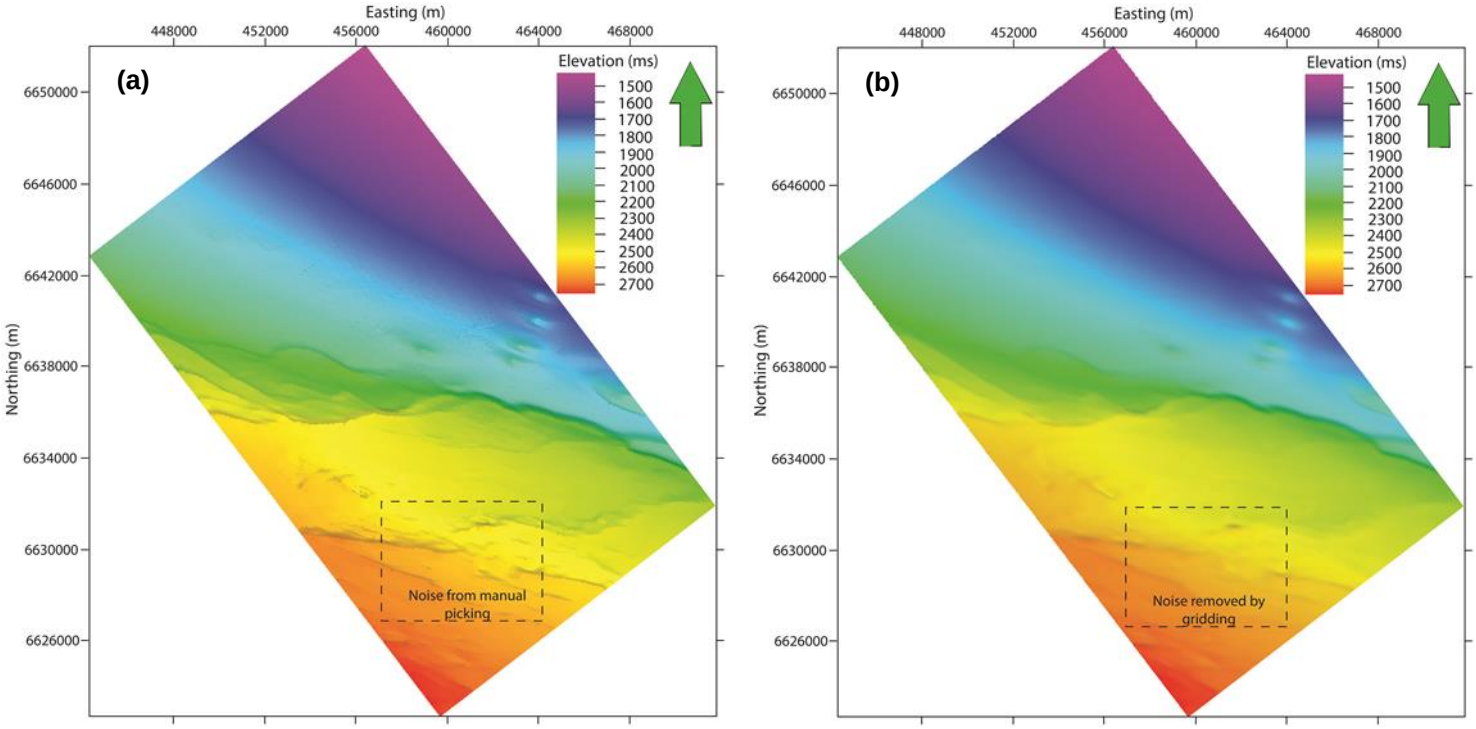


Figure 4.6. The seafloor horizon (a) before and (b) after smoothing using the Gaussian method. The dashed box highlights a structurally complex area where noise was generated by manual picking.

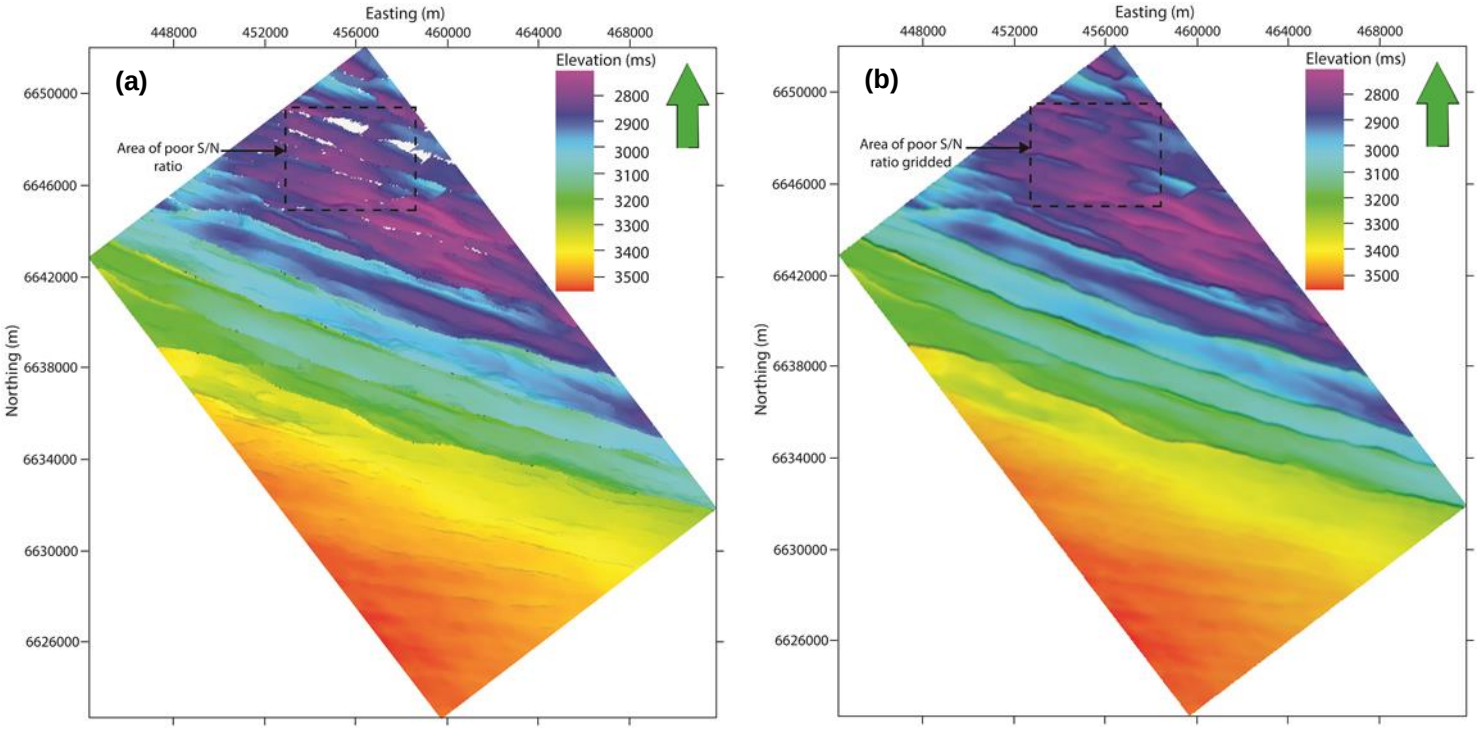


Figure 4.7. Horizon at the top of the thrust fault system (base of the Santonian) (a) before and (b) after applying the Kriging method to interpolate in structurally complex areas with sparse data. The dashed box highlights the areas that are structurally complex or have sparse data.

4.2. The application of volumetric attributes

The ant tracking attribute was applied to the seismic volume to increase confidence in structural interpretation and reduce bias associated with the interpretation of faults on seismic data. The ant tracking workflow is divided into four stages. These stages are seismic conditioning, edge detection, edge enhancement and interpretation (Pereira, 2009; Khair et al., 2012).

In the seismic conditioning stage, spatial noise is reduced while enhancing reflector continuity and preserving edges (structures). During this stage, the structural smoothing attribute is applied to eliminate noise and small-scale features (Khair et al., 2012). In this study, seismic conditioning was not applied, as the small-scale features could possibly be faults or fractures which are of interest to this study. For the edge detection stage, the chaos attribute was applied to the seismic volume. The chaos attribute measures the disorganisation in the dip and azimuth orientations (Pereira, 2009; Koson et al., 2014). Chaotic textures in the seismic data are detected using this attribute and in turn highlight positions where the reflector has been disrupted. The chaos attribute was used to enhance third-order scale faults and discontinuities (Pereira, 2009; Khair et al., 2012). Different parameters were used for chaos to find the best fitting variables to enhance the detection of edges. A filter size of 1.5 in the x-, y- and z-direction was determined to be best suited for these data (Figure 4.8a-c). Once the chaos attribute was applied, the ant tracking algorithm was computed on the chaos volume with the ant parameters and stereonet filter parameters presented in Table 4.1 and Figure 4.9a-b. In the final stage, fault patches are extracted from the ant tracked cube (Khair et al., 2012).

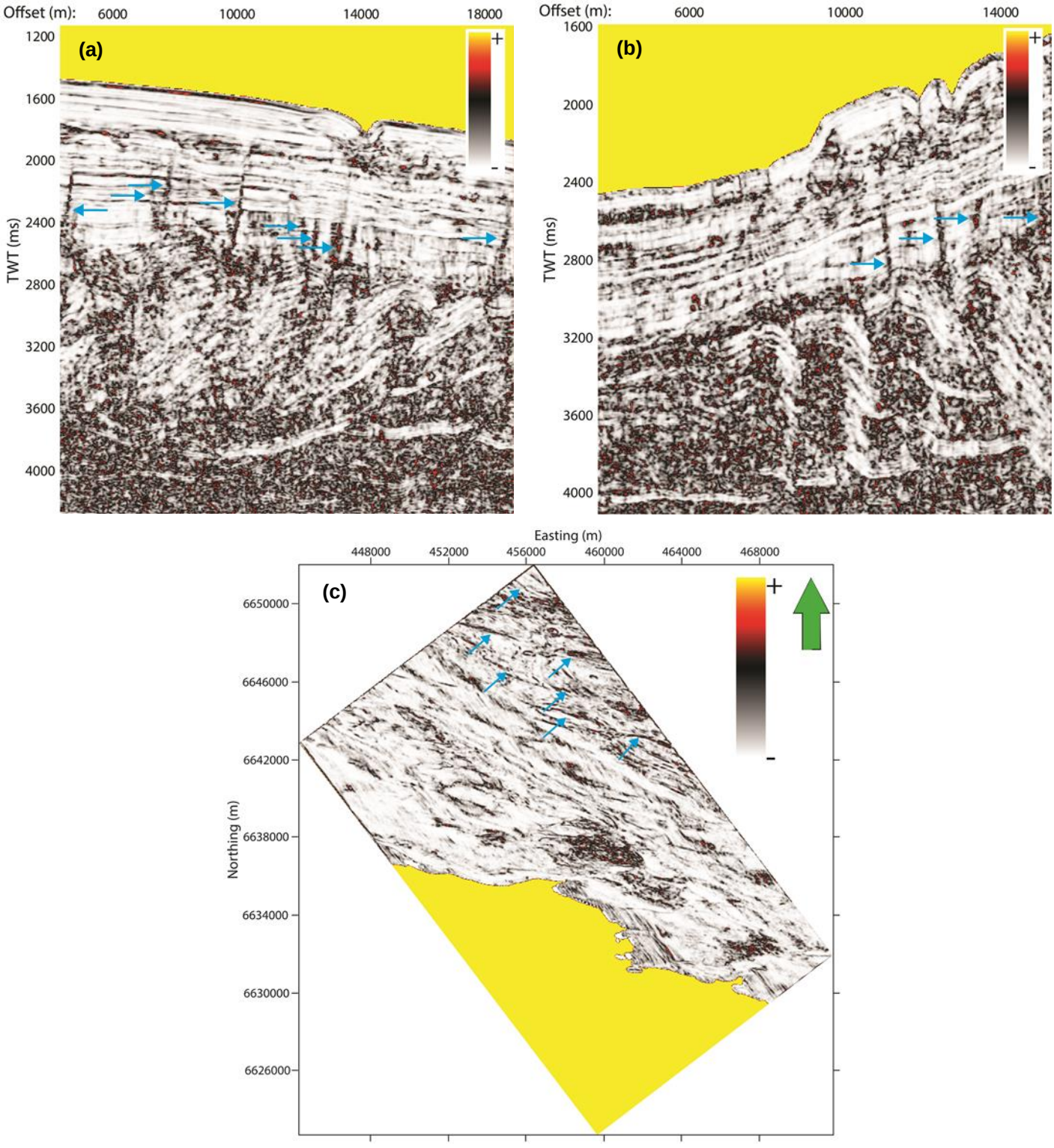


Figure 4.8. Chaos attribute applied to the (a) inline, (b) crossline and (c) time slice (Z = 2400 ms) prior to ant tracking computation. Blue arrows indicate structures that were further enhanced by ant tracking. In (a) and (b), the darkest zones are zones with high chaoticness. These highly chaotic zones are fracture/fault zones. Sections (a) and (b) are vertically exaggerated by a factor of 7.

Table 4.1. The parameters used in the application of the ant tracking attribute on the 3D seismic volume (After Pereira, 2009).

Parameter	Aggressive ants	Passive ants	Description
Initial ant boundary	5	7	Defines the initial distribution of agents. Large values result in loss of detail.
Ant track deviation	2	2	Controls the amount of deviation allowed on either side of the tracking direction.
Ant step size	3	3	The number of voxels an ant agent can move with every increment. An increase in this value will lower the resolution.
Illegal steps allowed	2	1	Defines the number of steps an ant agent can take without finding a local maximum in one direction in its search distance.
Legal steps required	2	3	The extent of connectivity of the detected edge
Stop criteria (%)	10	5	The percentage of illegal steps that any agent is allowed

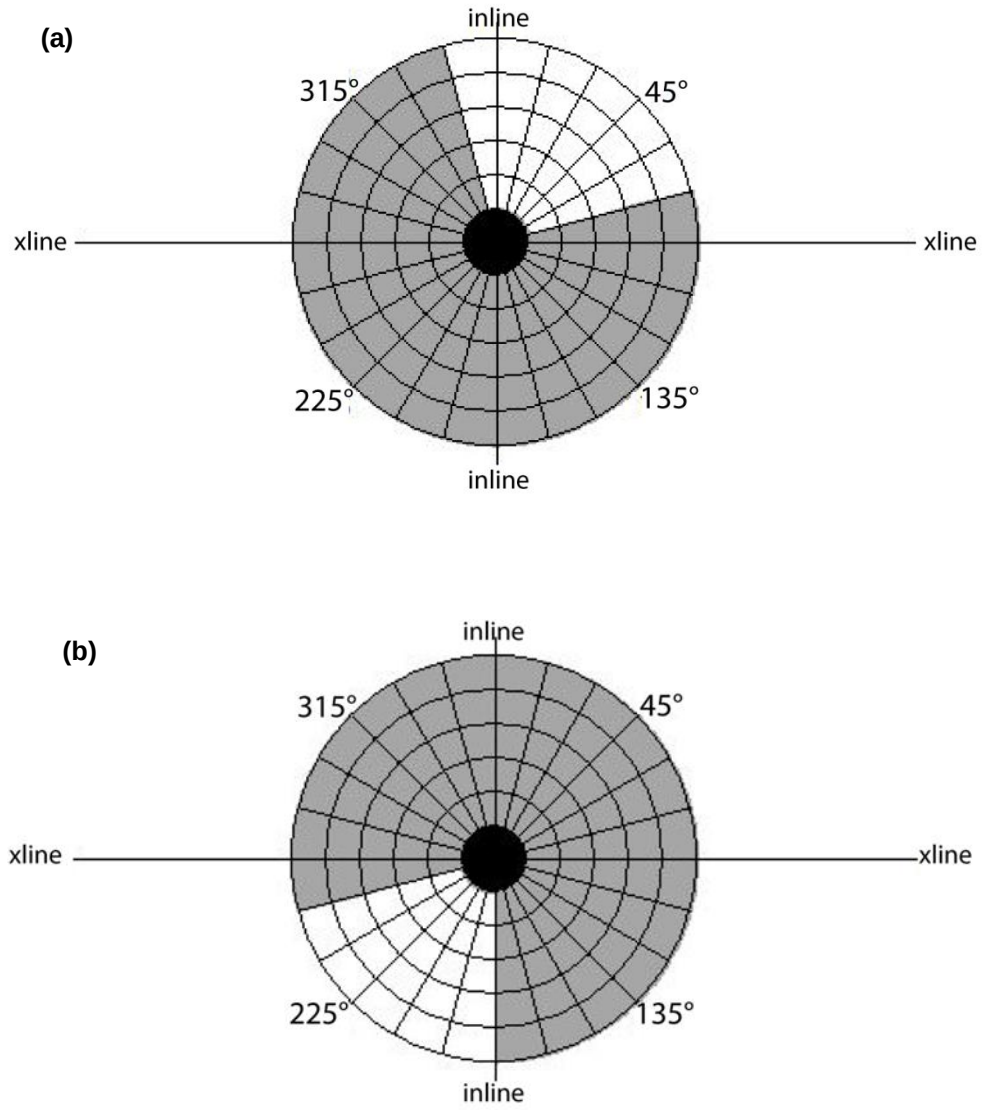


Figure 4.9. Stereonet filters used to compute ant tracking seismic cube. (a) Stereonet for normal faults dipping at 0°-90° N to ENE (b) Stereonet for normal faults dipping at 0°-90° S to WSW.

The ant tracking algorithm was run twice on the chaos volume which enabled better detection of faults and fractures. The first ant tracking run was computed with parameters reflecting the aggressive ants to detect both major and small-scale structures. The second ant tracking run was computed on the output volume of the first ant tracking run. This time, passive ants were used. Figure 4.10a is the result of the first run of the ant tracking attribute. Bedding-parallel discontinuities have been detected as well as several faults; however their continuity is not apparent. The second run highlighted the continuity of the faults while reducing the resolution of the discontinuities parallel to bedding (Figure 4.10b). Computing the ant tracking algorithm over the same attribute cube will result in further delineation of faults. In the first and second ant tracking passes, the stereonet filter was applied to detect faults that dip 0° to 90° N-ENE (see Figure 4.9a).

The ant tracking algorithm was run again on the chaos volume. This time the stereonet filter was applied to detect faults with dip directions between 180°-250° (S-WSW) and dip 0° to 90° (see Figure 4.9b). The aggressive ant parameters were used and only one run was computed.

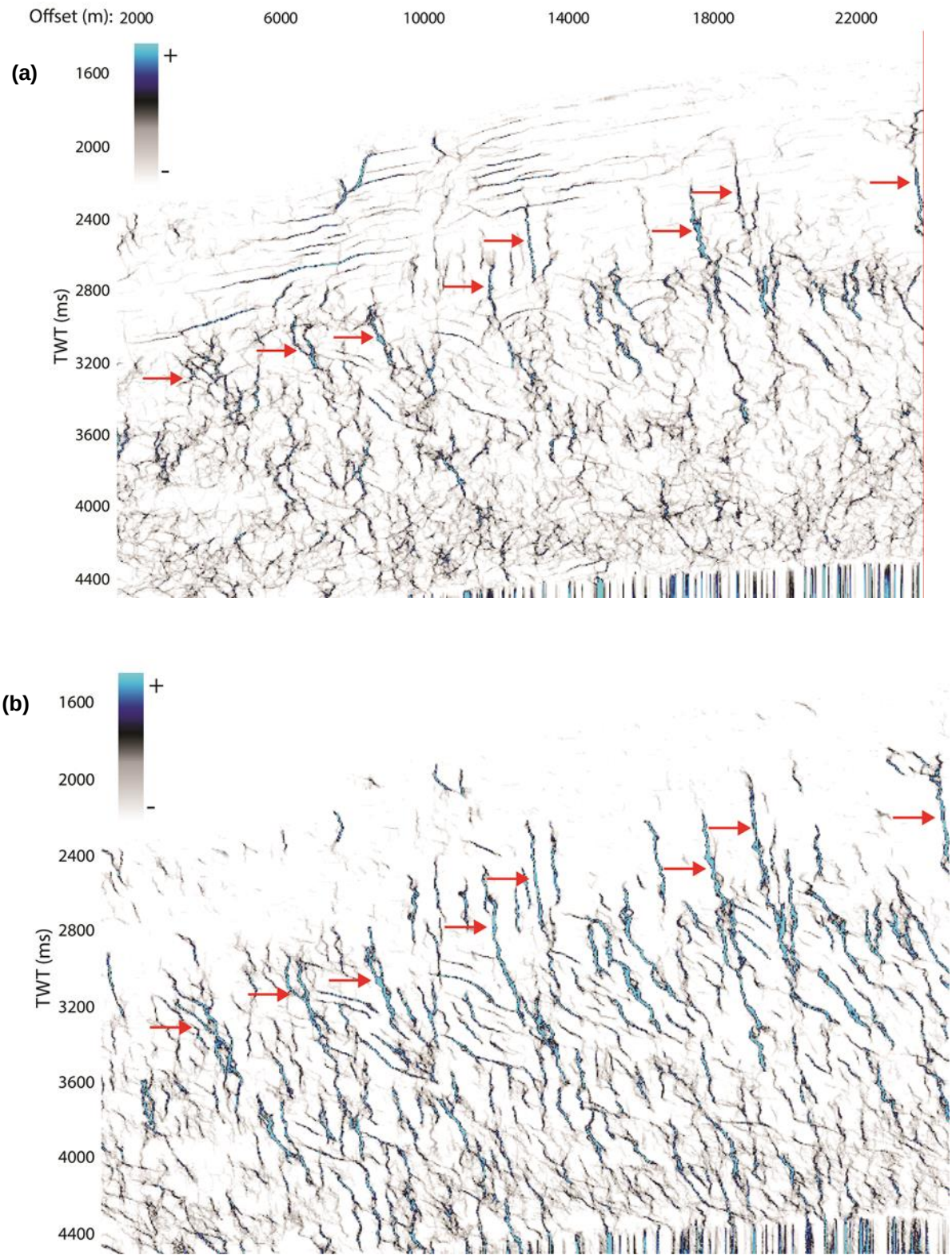


Figure 4.10. (a) An ant tracked volume of the first run with the stereonet filter applied to detect faults dipping N-ENE. The red arrows point to fault whose continuity is highlighted in the second run. (b) An ant tracked volume of the second run with the stereonet filter applied to detect faults dipping N-ENE. Sections (a) and (b) are vertically exaggerated by a factor of 7.

The final stage of ant tracking involves the extraction of the N-ENE and S-WSW dipping faults from the ant tracked seismic volume (Figures 4.11 and 4.12).

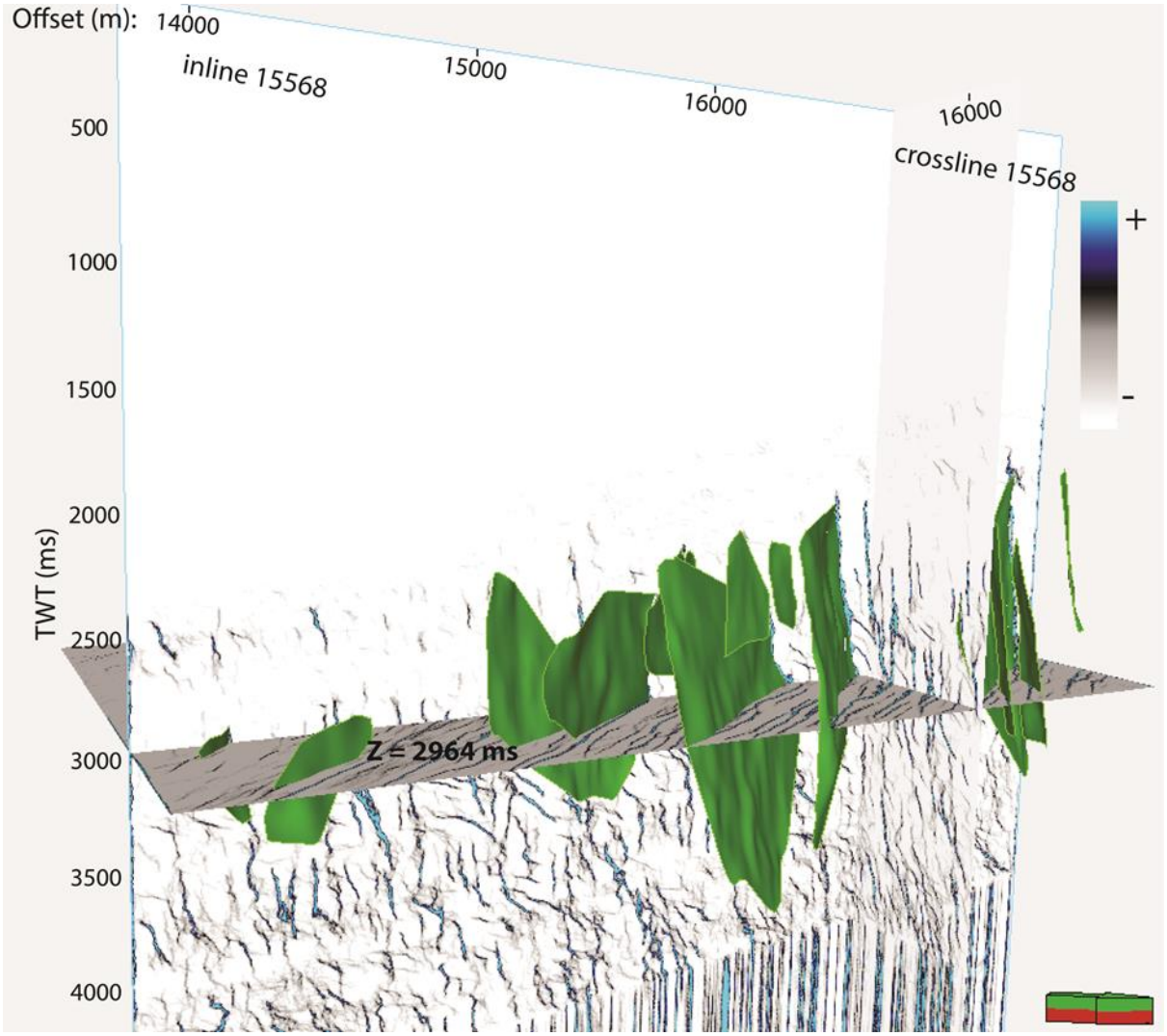


Figure 4.11. An ant tracked volume highlighting the extracted N-ENE dipping faults in green. Vertical exaggeration (VE) is 7:1.

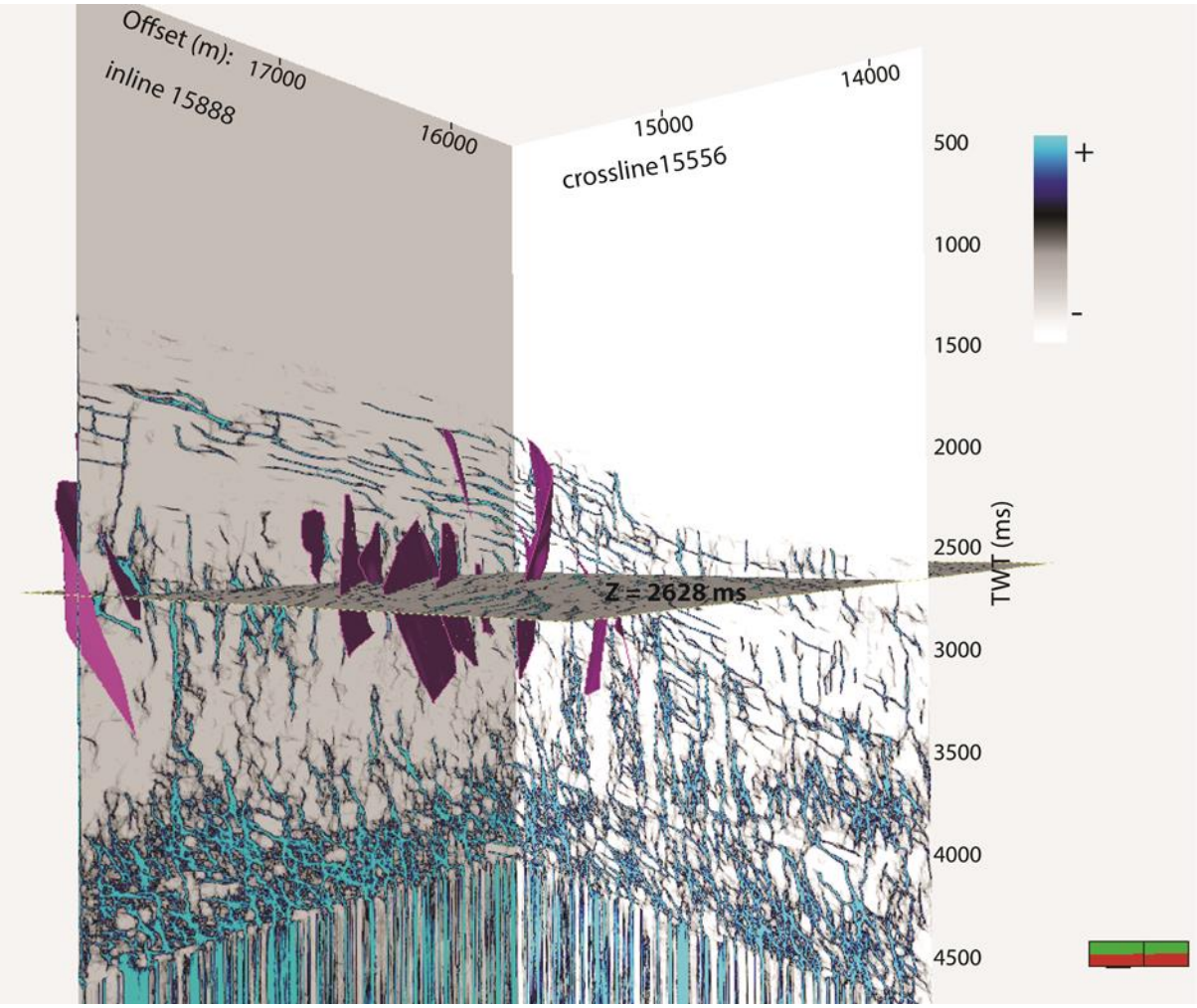


Figure 4.12. An ant tracked volume highlighting the S-WSW dipping faults in pink. Vertical exaggeration (VE) is 7:1.

4.3. 3D geological model

Modelling of the complex structures in the study area involved: (1) 3D seismic imaging, (2) picking of horizons and first- and second-order scale structures, (3) data conditioning using signal filters, (4) detection and extraction of third-order scale faults by attribute analysis, (5) fault and horizon modelling, and (6) structural gridding. With the use of advanced modelling software packages such as Petrel, the interpreter can produce a high-quality 3D structural model which takes into account complex architectures such as cross-cutting faults (Manzi et al., 2013).

Before modelling, the faults and horizons have to be picked, and the structural framework and the coverage of the faults have to be defined. Three sets of faults were delineated, the N dipping thrust

faults, N-ENE and S-WSW dipping normal faults, which cover an area of 400 km^2. Fault modelling involved smoothing of individual faults. For horizon modelling, the Cenomanian-Turonian boundary, top and base of the Coniacian-Santonian units, base of the Palaeogene and seafloor were modelled as conformable horizons. The base of the Maastrichtian was modelled as an erosional unconformity. The initial step of modelling the horizons is to grid all the horizons. The horizons which are intersected by faults (i.e., top and base of the Coniacian-Santonian units) were gridded using the modelled fault polygons as an input and the areas that were not intersected by faults on the horizon were gridded using the Gaussian gridding method (Figure 4.13).

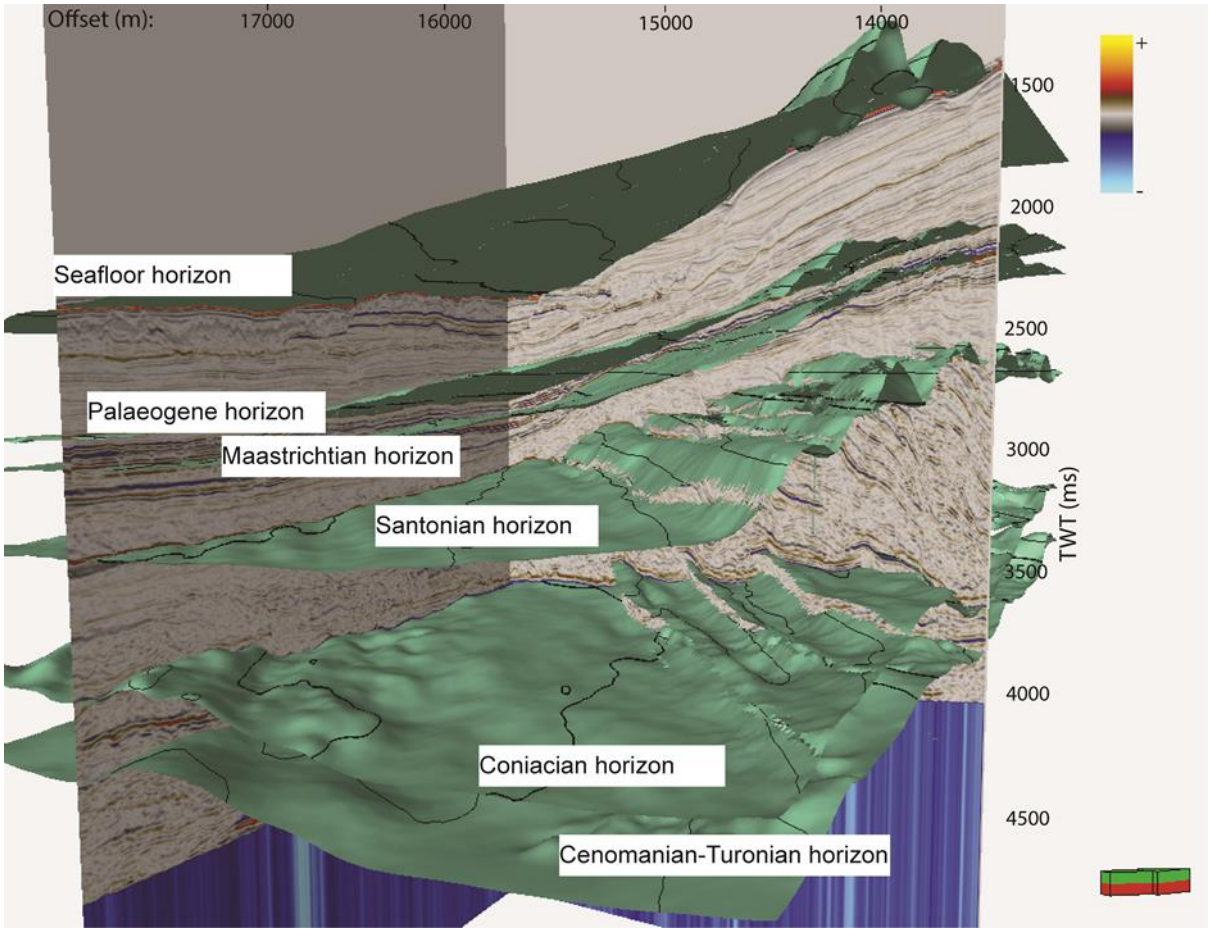


Figure 4.13. 3D seismic volume overlain with gridded horizons. The contour interval is 50 m. Vertical exaggeration (VE) is 7:1.

Once the horizons had been gridded, the zones were defined. Zones are the intervals between the horizons. The horizons were grouped into five zones, which were further divided into layers (Figure 4.14).

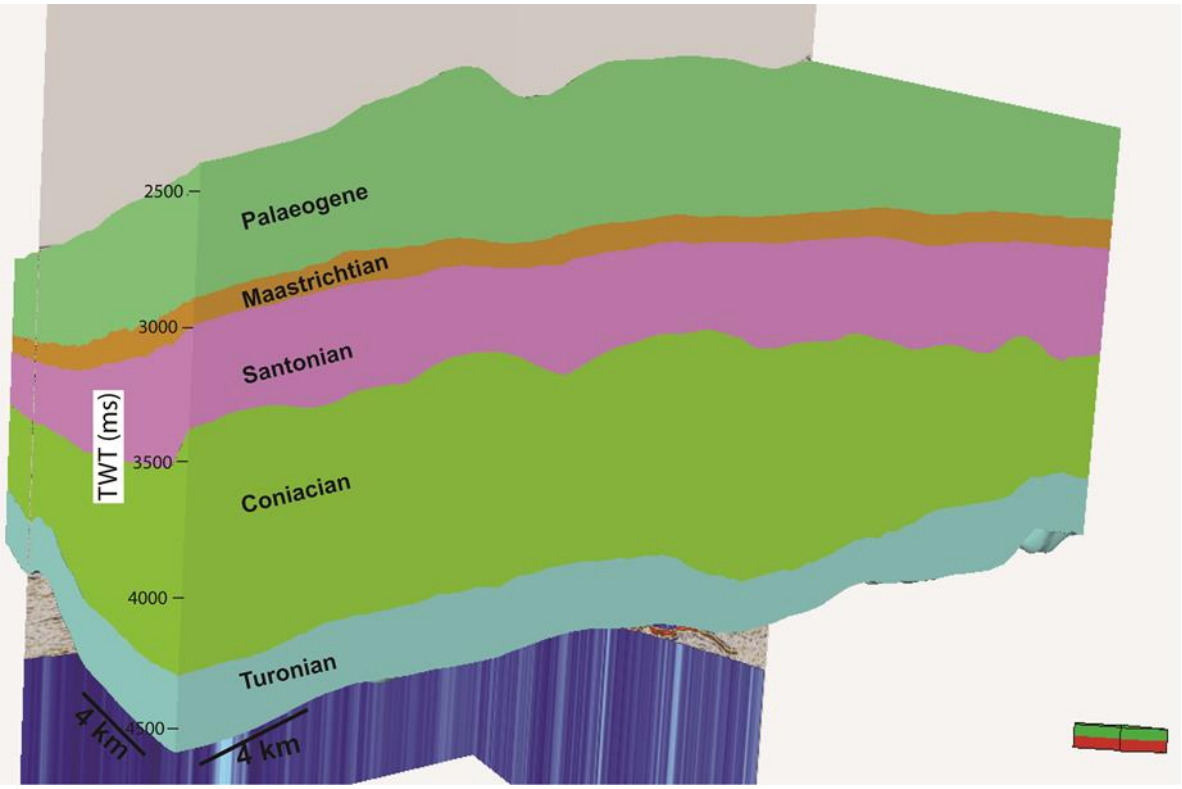


Figure 4.14. Horizons are intersected with the fault framework to create solid model. The model is divided into five zones.

The horizon modelling uses a fault block-based approach, where the fault framework is used to sort the horizon data into discrete fault blocks. A horizon surface is produced for the individual fault blocks and as the surface intersects fault zones, it is displaced. Once the faults and horizons have been modelled, structural gridding is applied. Structural gridding uses the structural framework and applies the geometry of the faults and the defined zones as the input to produce stair-stepped corner point grids (Figure 4.15). Figure 4.16 presents the workflow used to construct the 3D geological model.

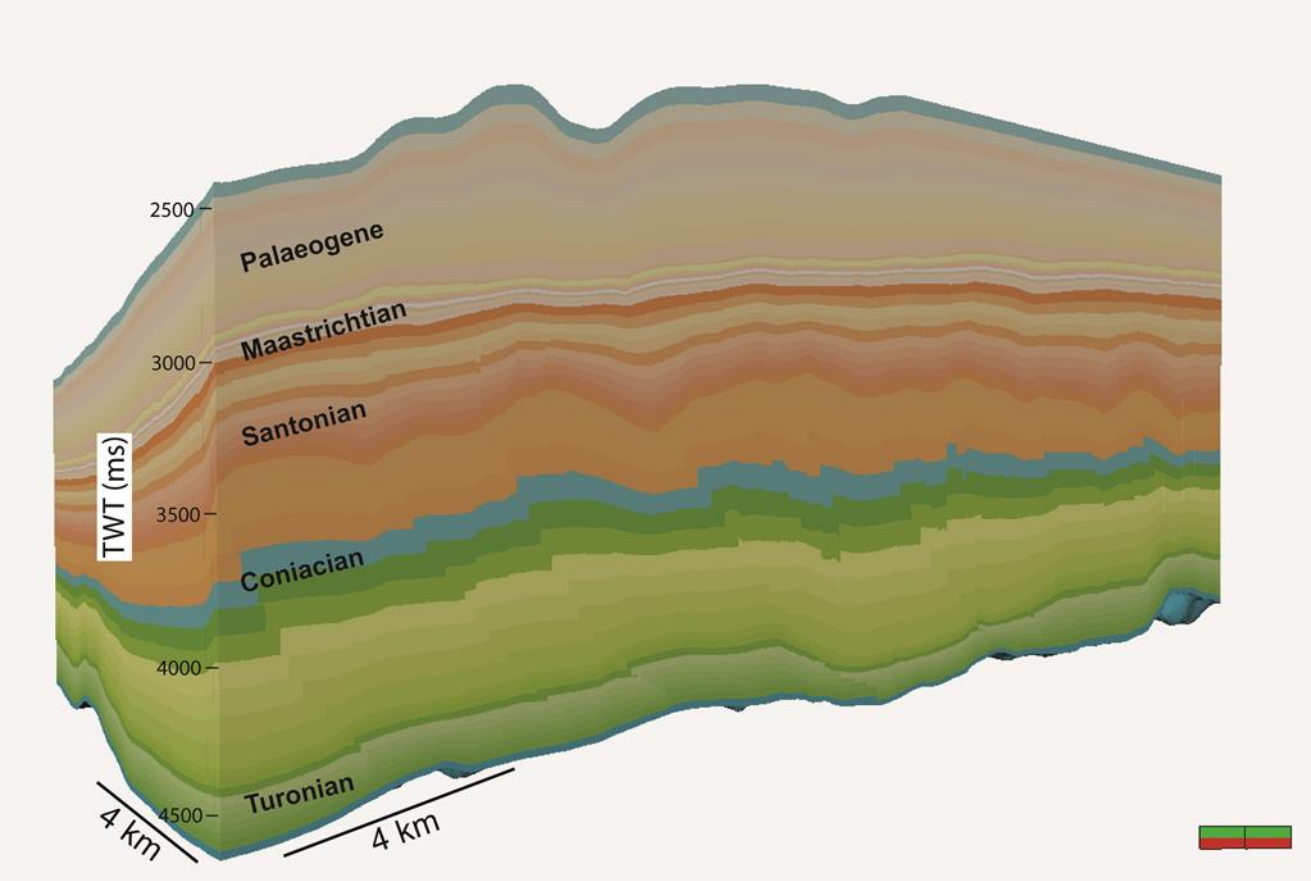


Figure 4.15. 3D model showing layering and displacement of layers due to faulting.

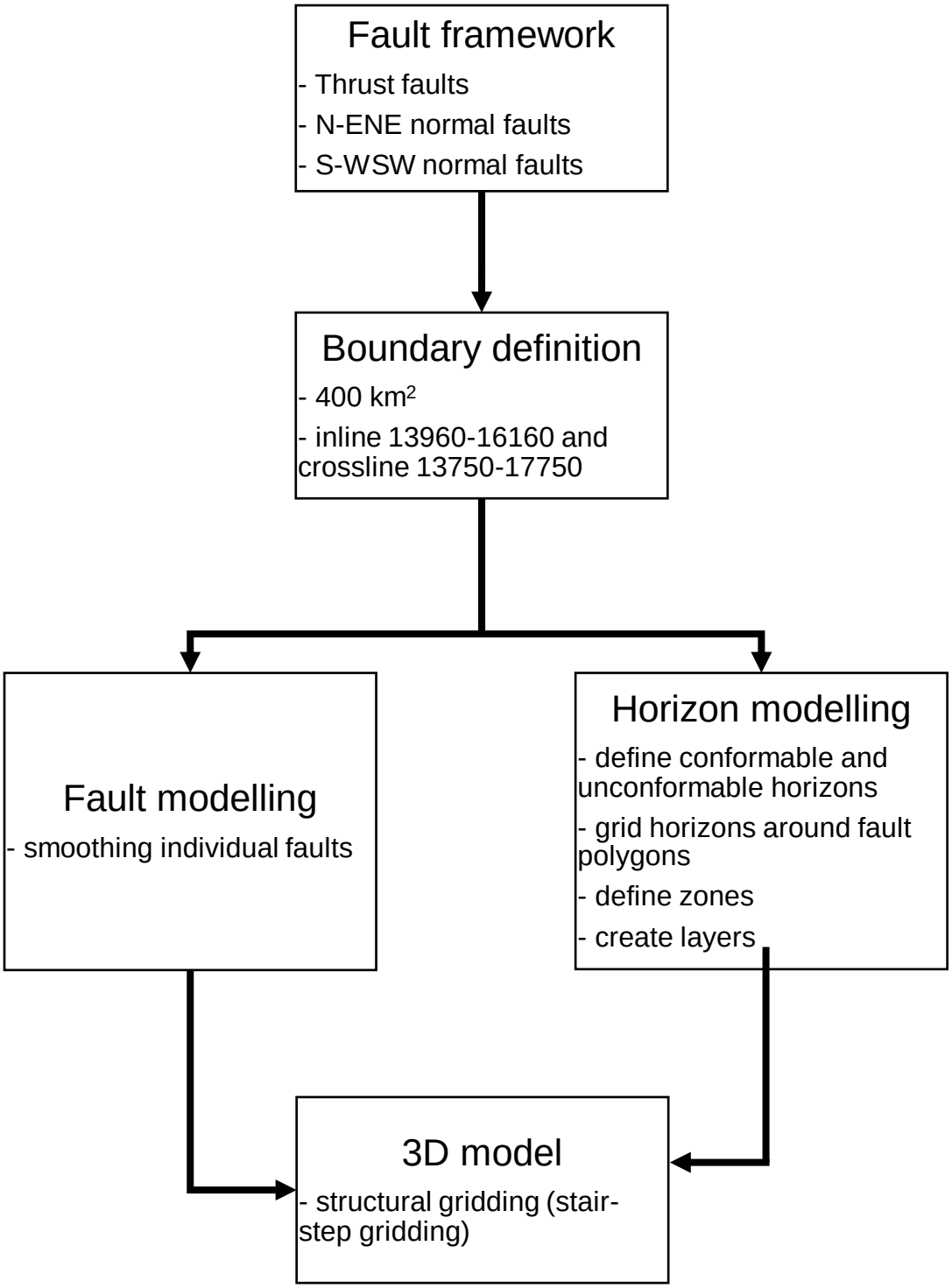


Figure 4.16. Workflow used to construct a 3D geological model of the deepwater Orange Basin.

5. STRUCTURAL STYLES IN THE DEEPWATER FOLD AND THRUST BELT

5.1. Introduction

The lower portion of the continental slope is characterised by a contractional domain which developed in the Coniacian to Santonian sedimentary sequences. The contractional domain is dominated by thrust faults that connect with a regional basal detachment (de Vera et al., 2010). The structural styles observed in passive margin fold belts are strongly dependent on the type of detachment layer (Rowan et al., 2004). The deformation processes occurring within the detachment layer have a major influence on the geometries of the thrust- related folds, which may be associated with pathways for fluid migration and petroleum trap formation (Maloney et al., 2010). Understanding the deformation mechanisms is of great importance to successfully explore deepwater fold and thrust belts.

The high-resolution 3D seismic data provided by Shell Global Solutions International B.V imaged the stratigraphy to approximately 4.4 s, indicated by the red line (Figure 5.1). Due to confidentiality, data below post-rift sequence II were cut from the seismic volume by Shell Global Solutions International B.V. This chapter presents the interpretation of horizons and faults with the use of conventional seismic interpretation methods and the application of seismic attributes. Horizon-based attributes were applied to detect small-scale faults with displacement less than the vertical resolution limit of 12 m. These attributes were applied specifically to the Maastrichtian unconformity and base of the Palaeogene horizons, to detect normal faults that were not imaged using the conventional interpretation methods. The volumetric attribute applied was ant tracking. Ant tracking was applied to enhance the detection of small-scale faults and determine whether there is connectivity between the thrust faults in the Coniacian-Santonian units and the normal faults in the Maastrichtian and Palaeogene units. Boreholes were not available for this study; therefore, velocities found in literature were used for the time-to-depth estimates.

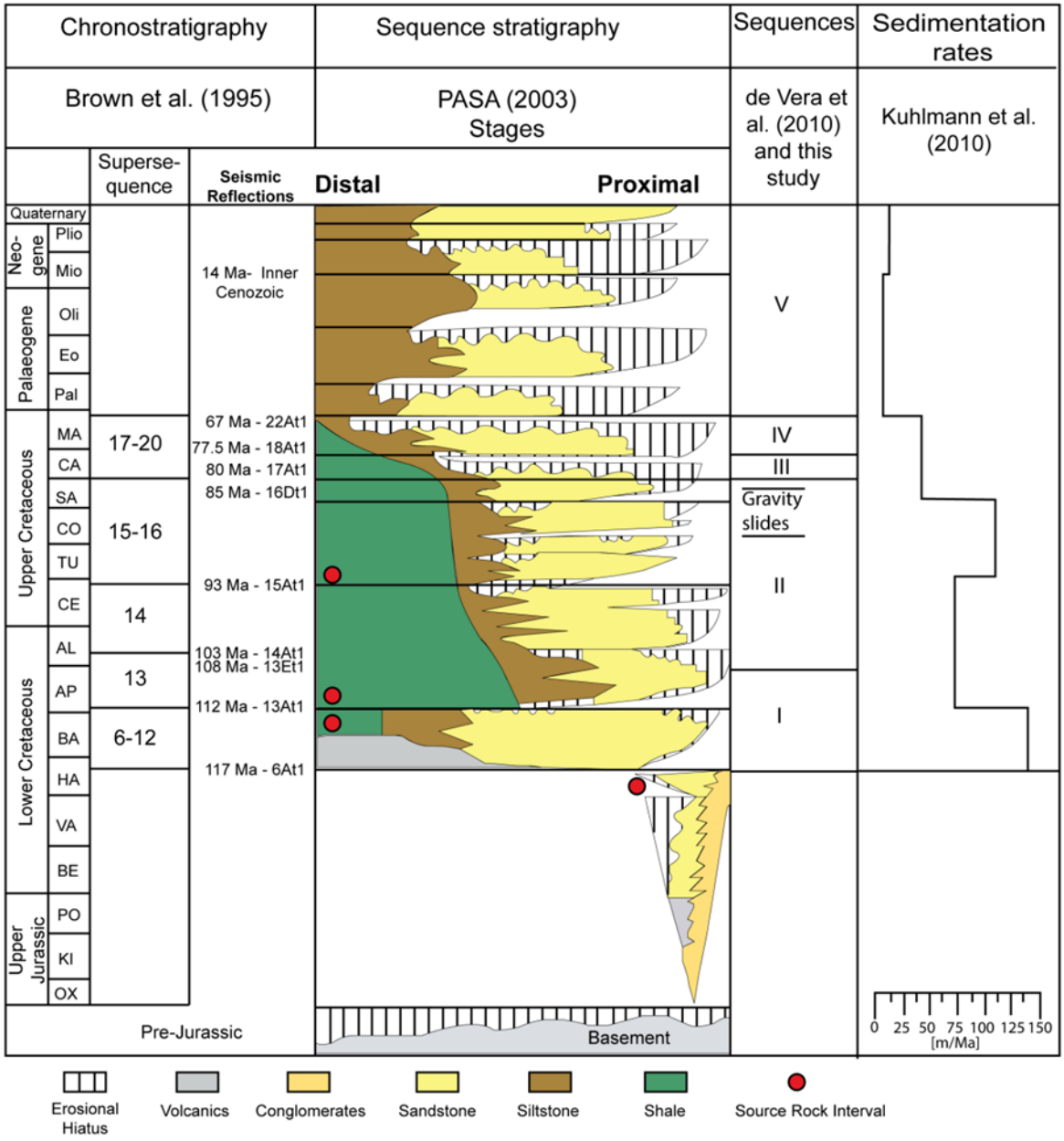


Figure 5.1. Chronostratigraphic and sequence chart for the Orange Basin illustrating major stratigraphic units and sedimentation rates. Stratigraphic units below the red line were cut from the seismic volume. 6-12, 13, 14, 15-16, 17-20 represent supersequences classified by Brown et al. (1995). OX (Oxfordian); KI (Kimmeridgian); TI (Tithonian); BE (Berriasian); VA (Valanginian); HA (Hauterivian); BA (Barremian); AP (Aptian); AL (Albian); CE (Cenomanian); TU (Turonian); CO (Coniacian); SA (Santonian); CA (Campanian); MA (Maastrichtian); Pal (Palaeocene); Eo (Eocene); Oli (Oligocene); Mio (Miocene) and Plio (Pliocene). I – V represents the classification by de Vera et al. (2010) used to group sequences from the Hauterivian to Holocene (modified from Boyd et al., 2011; Loegering et al., 2013).

5.2. Results

5.2.1. Basal detachment fault

Two basal detachment layers are imaged in the contractional domain. The basal detachment that formed first possibly coincides with the Cenomanian-Turonian boundary at 4150 ms, approximately 7800 m deep, and the second detachment layer is observed at the base of the Coniacian at approximately 3600 ms, approximately 5700 m deep (Figure 5.2a-b). The Cenomanian-Turonian detachment is discontinuous and is terminated by slump deposits in the southern portion of the study area (Figures 5.3 and 5.4). The detachments are picked by the identification of common fault terminations.

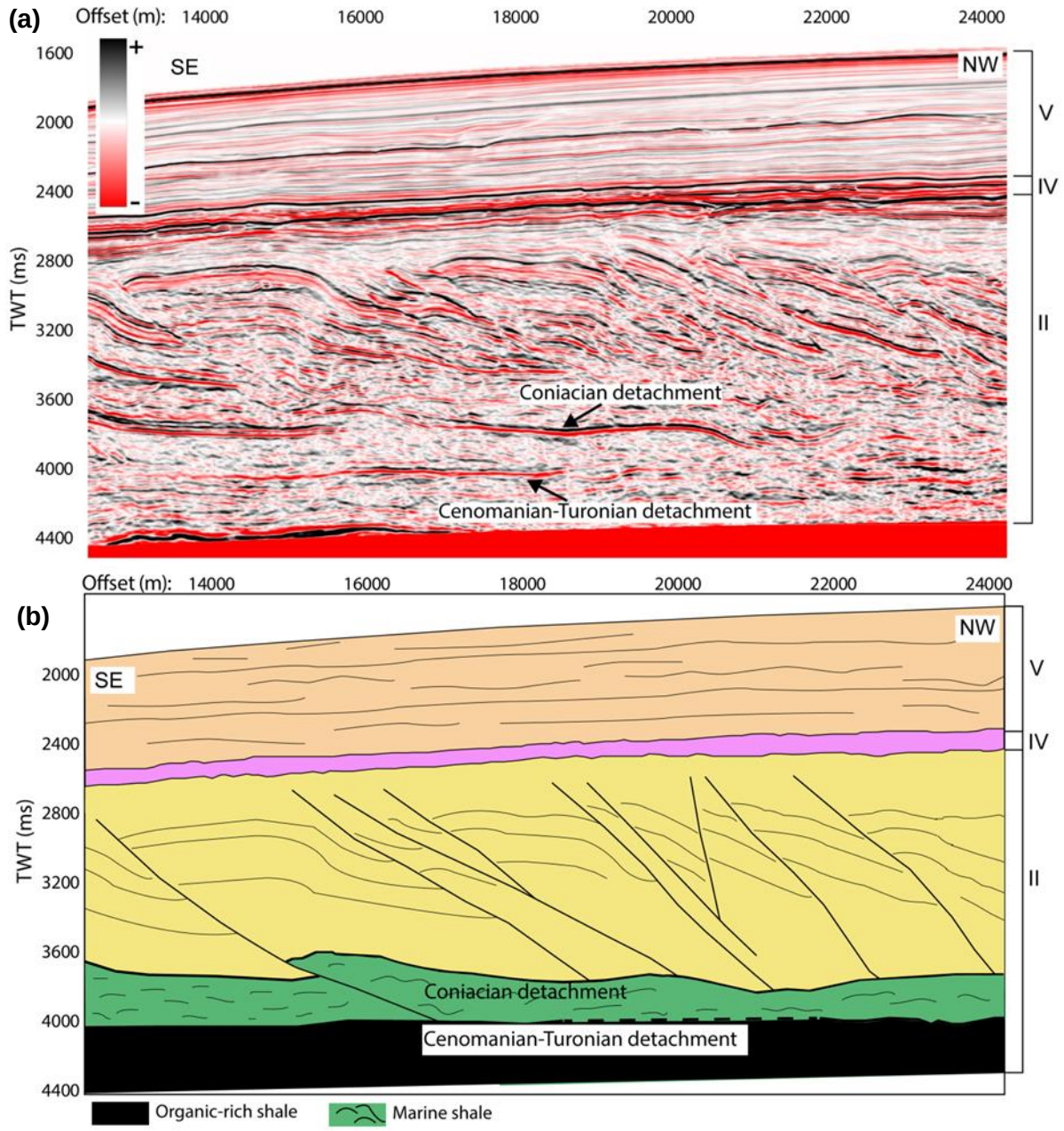


Figure 5.2. (a) An amplitude display seismic section and (b) a schematic diagram showing thrust faults attached to two basal detachment levels. The thrust faults to the NW sole into the Coniacian detachment and the thrust faults to the SE sole into the Cenomanian-Turonian detachment. Post-rift sequences II, IV and V were identified. Sections (a) and (b) are vertically exaggerated by a factor of 3.

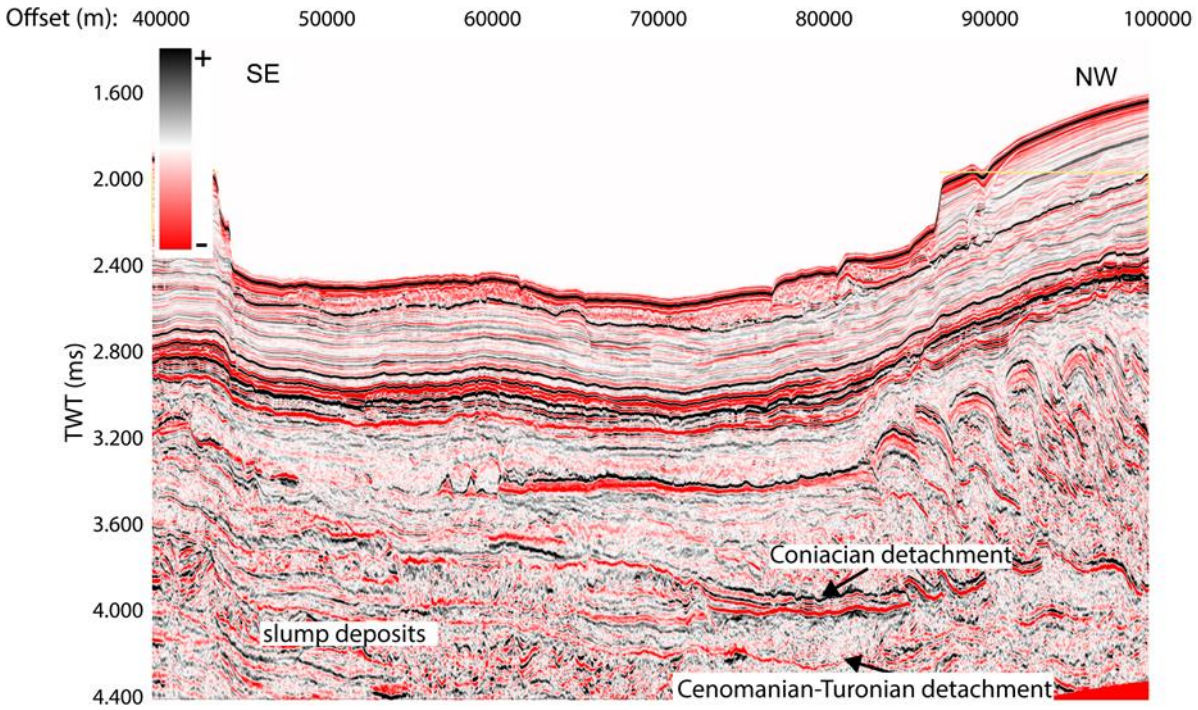


Figure 5.3. An amplitude display section showing the Coniacian and Cenomanian-Turonian detachments. The Cenomanian-Turonian detachment is terminated by a slump deposit in the south. The vertical exaggeration (VE) of the section is 17:1.

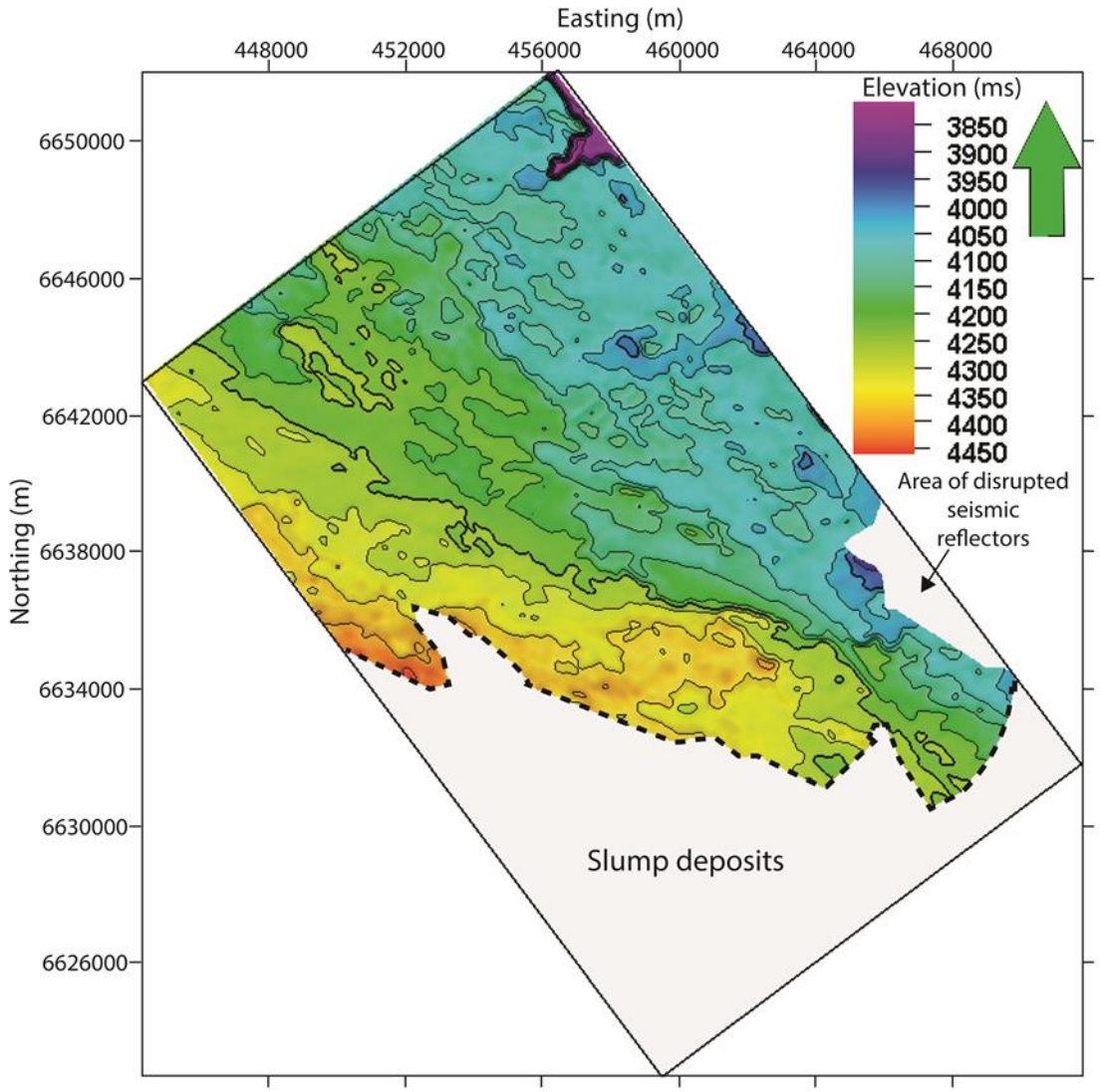


Figure 5.4. A depth structure map of the Cenomanian-Turonian detachment layer showing the discontinuous nature of the detachment. The detachment layer is at shallower depths in the north and progressively deepens towards the south. The contour interval for the map is 50 m.

5.2.2. Fault and fold geometries

The study area is dominated by thrust faults dipping landwards with a planar geometry, becoming slightly curved as they connect with the basal detachment at the Cenomanian-Turonian boundary. However, the thrust faults that attach to the Coniacian basal detachment maintain a planar geometry (see Figures 5.2a-b and 5.5). The thrust faults strike 290° with a N to NNE dip direction. They dip between 30° to 45° basinward and the dip angle increases to 60° towards the north (Figure 5.5).

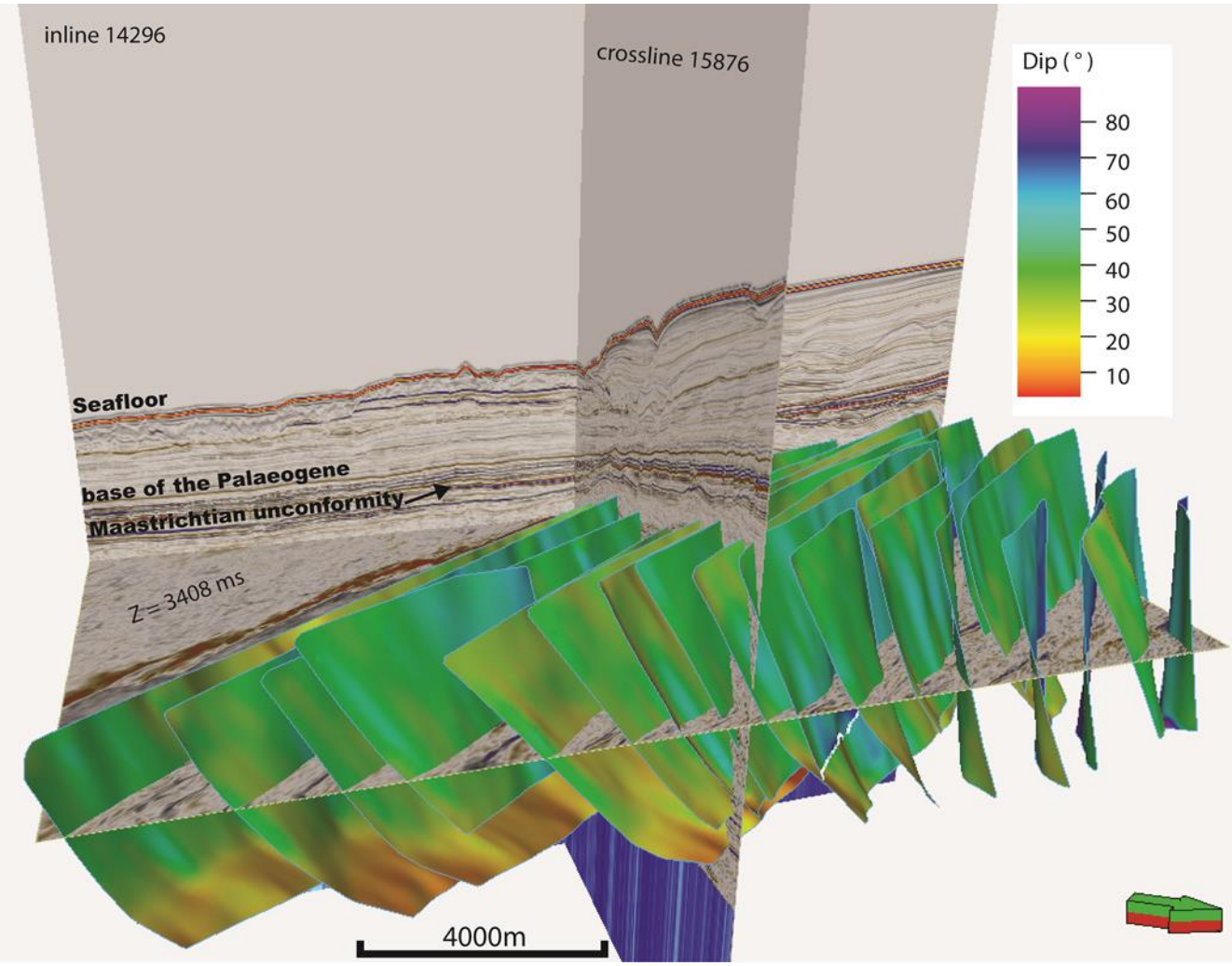


Figure 5.5. A 3D model of the thrust fault system showing variations in dip angle with depth and to the north, the faults dip steeply. The faults in the south, along the deformation front, have dip angles between 30° and 40°, and shallow to 10° with depth. In the north, the faults are dipping at high angles (60° - 70°). The vertical exaggeration (VE) is 5:1.

The thrust faults extend along strike for several tens of kilometres and their spacing ranges from 0.2 to 1.7 km (Figures 5.6 and 5.7). The maximum distances between faults are at the deformation front and they progressively decrease landward (Figure 5.7). The displacement along the faults was measured on the horizon at the top of the Coniacian-Santonian thrust fault system (base of the Santonian) (Figure 5.6). The displacement measurements presented in Figure 5.8 are measured in time and converted to depth using an average velocity of 3000 m/s, which is the average velocity of the Coniacian to Santonian units. The displacement for 22 faults is measured at 1000 m intervals along the strike of the fault (Appendix A). Figure 5.8 presents faults where more than 2 displacement measurements are recorded

along the strike of the fault. The displacement along the faults increases progressively from the faults located at the deformation front to the fault identified in the inner part of the thrust fault system (Figures 5.8 and 5.9). Large displacement measurements ranging from 38 to 413 m are recorded in the inner part of the thrust fault system. Smaller displacement measurements ranging from 60 to 240 m and 15 to 173 m are recorded at the deformation front and the rear of the thrust fault system, respectively (Figure 5.8). Displacement measurements on individual faults, measured along the fault ramp, are presented in Appendix A. Maximum displacement measurements are recorded at the centre of the fault ramp with a decrease in displacement towards the fault tip and detachment fault.

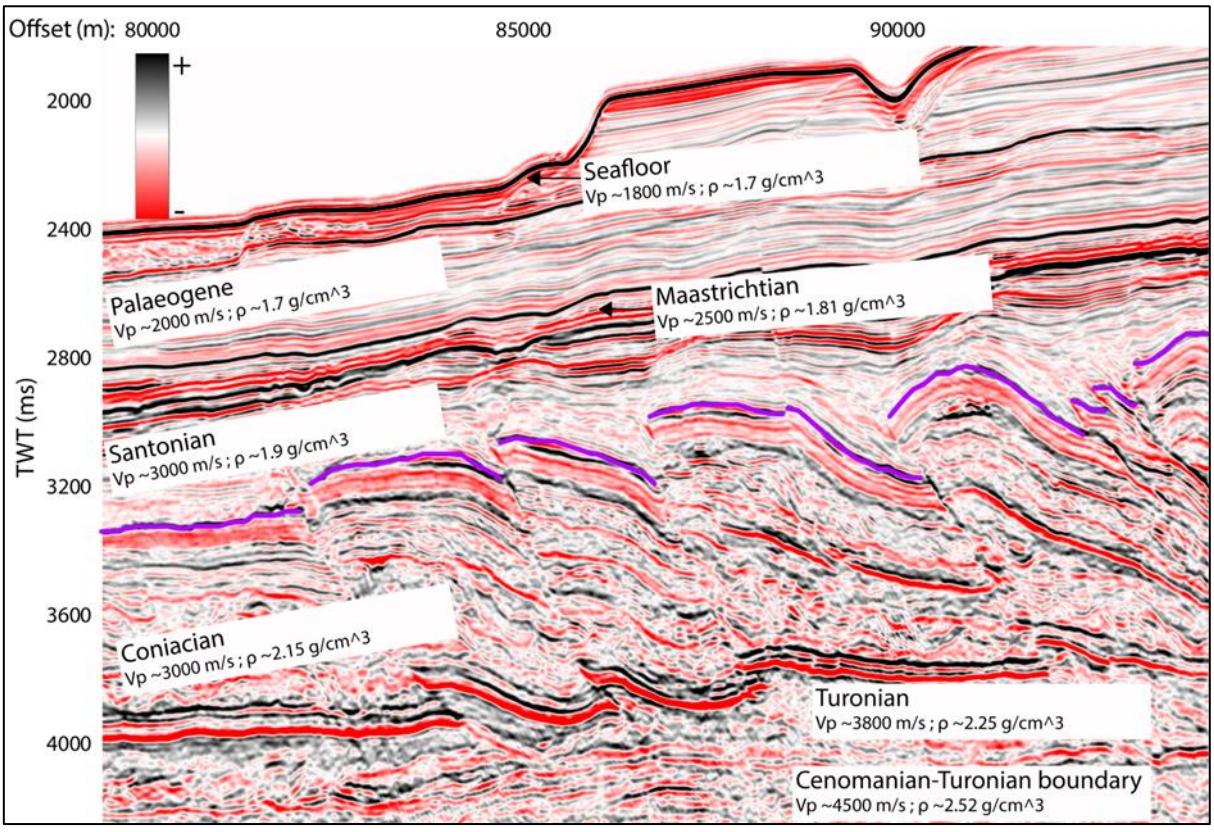


Figure 5.6. An amplitude display seismic section showing faults at the deformation front. The horizon used to measure displacement along the fault is highlighted. The vertical exaggeration (VE) of the section is 8:1.

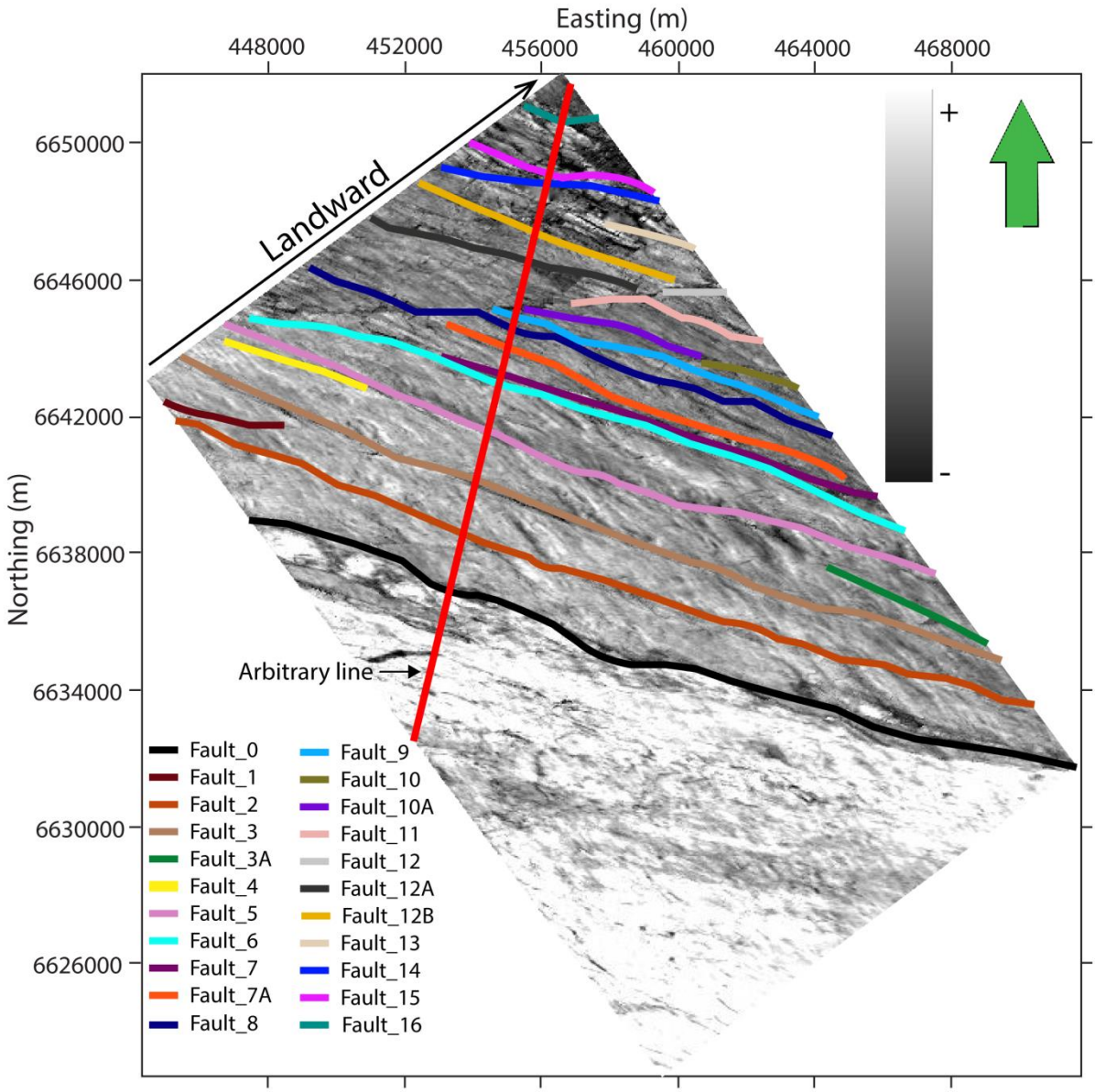


Figure 5.7. An elevation map of the horizon located at the top of the thrust fault system (base of the Santonian) (highlighted in Figure 5.6) with an overlay of thrust fault polygons. The faults are trending WNW-ESE. The red line represents an arbitrary line presented in Figure 5.9.

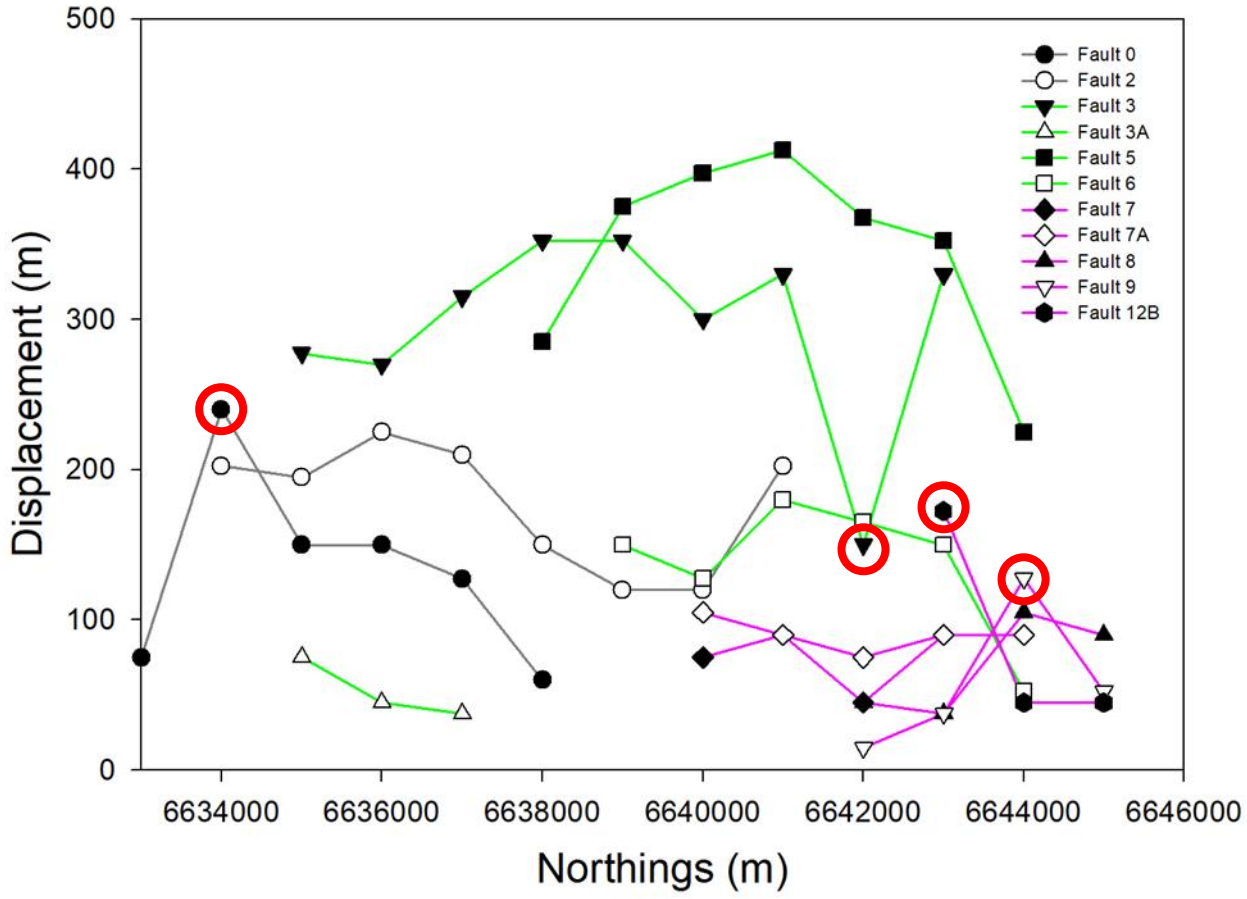


Figure 5.8. A south-to-north profile of the Coniacian to Santonian thrust fault system showing variations in vertical displacement with distance along the strike of the fault. The faults in grey occur along the deformation front; the faults in green are mapped in the inner part of the thrust fault system and the faults in pink are at the rear of the thrust fault system. Anomalous displacement measurements are indicated by the red circles.

Normal faults are identified in the Maastrichtian and the base of the Palaeogene units. The normal faults imaged using the conventional interpretation methods have a vertical displacement above 12 m. It was challenging to determine the dip and dip direction of the faults in the amplitude display of the inline and crossline seismic sections due to inconsistencies in displacement along the faults. In some parts of the study area, the fault displacement decreases below the vertical resolution limit, resulting in difficulties in tracking the faults along strike. The conventional interpretation method is supplemented by the application of horizon-based attributes to highlight the dip and dip direction of the normal faults.

Well-developed folds associated with the thrust fault system are observed. The faults in the Orange Basin have been previously interpreted as fault-propagation folds that are generally asymmetric and characterised by a short forelimb, a broad and gently dipping crest and a long and gently dipping backlimb (Granado et al., 2009). The folds observed in the deepwater Orange Basin lack forelimbs and the backlimbs are gently dipping (at angles between 4° and 24°) (Figure 5.9). The thrust faults propagate through the footwall synclines and the fold vergence is in the direction of transport (Figure 5.9). The amount of backlimb rotation is interpreted to increase towards the inner part of the thrust fault system (Figure 5.9). The folded stratigraphic layers maintain a constant thickness of approximately 825 m across the dip domains.

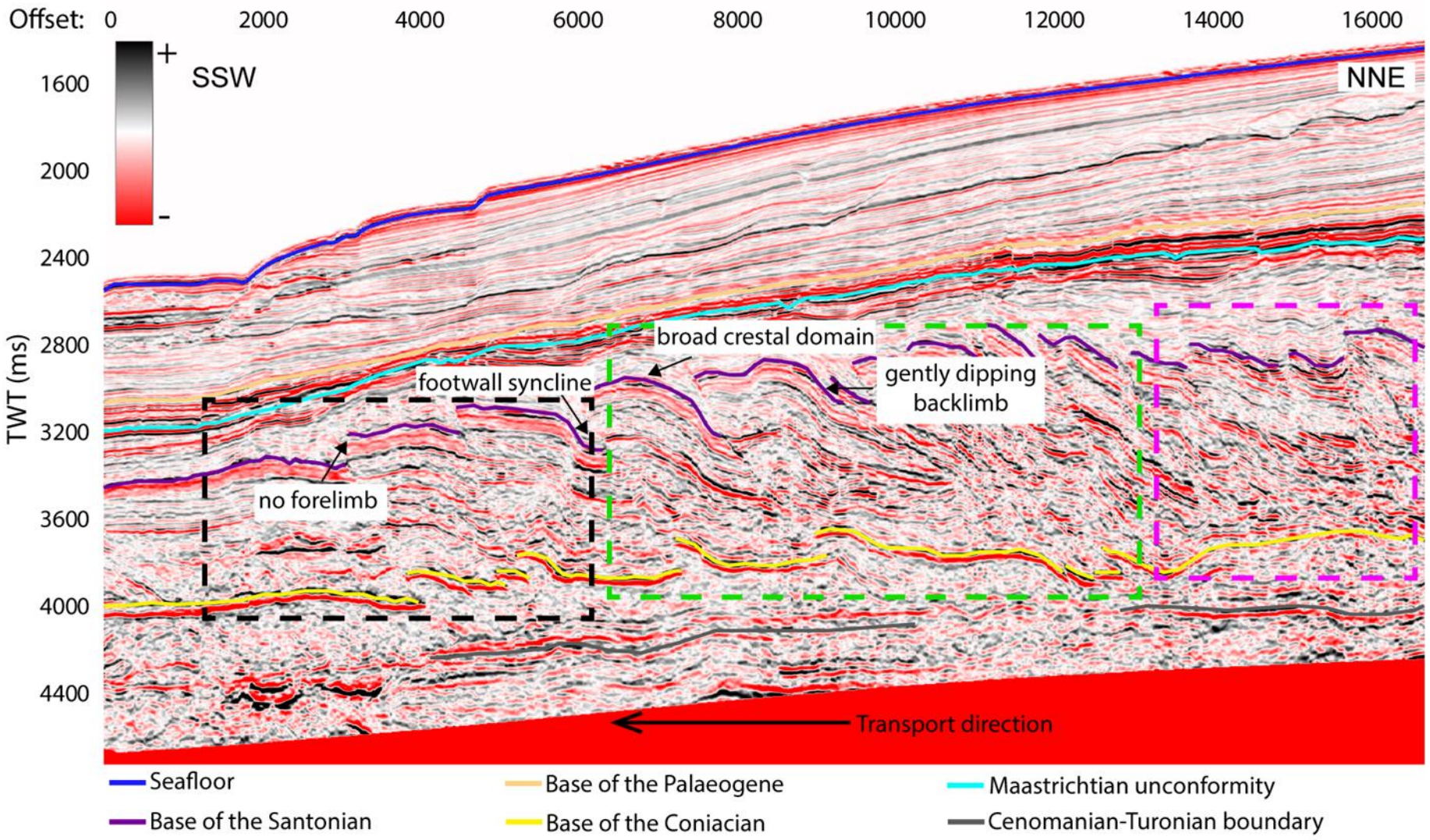


Figure 5.9. An amplitude display seismic section showing the geometry of the folds. The folds are asymmetric with backlimbs that dip gentler than the fault ramp. The backlimbs dip approximately 4° – 24°. The thrust faults cut through the forelimbs of the folds and the footwall synclines. The area to the north is structurally complex and highly deformed compared to the south. The black block highlights faults along the deformation front; green block highlights faults in the inner part of thrust fault system and pink block shows faults at the rear of the system. Vertical exaggeration (VE) of the section is 3:1

5.2.3. Application of horizon-based attributes

The dip and dip azimuth attributes are applied to determine the dip angle and the dip direction of the faults, respectively. Figure 5.10a shows the high-resolution imaging of normal faults at the Maastrichtian unconformity with a similar strike direction as the thrust faults imaged in the Coniacian-Santonian sequences. The faults have dip angles ranging from 4° to 12° and may reach 14° in some areas along the fault. The faults are dipping N-ENE towards the northern and southern portions of the study area (indicated by the black arrows) and in the central part between elevations of 2500 to 3100 ms, the faults are dipping predominantly S-WSW (indicated by the red arrow) (Figure 5.10b). The base of the Palaeogene sequence directly overlies the top of the Maastrichtian sequence and displays similar structural trends. The faults dip between 4° and 13° and have variable dip directions (Figure 5.11a). The faults in the northern and southern parts of the study area are dipping predominantly to the north (indicated by black arrows) and the faults in the central part have a southwesterly dip (indicated by the red arrow) (Figure 5.11b). In Figures 5.10a-b and 5.11a-b, the dip attribute shows clear detection of faults compared to the dip azimuth attribute.

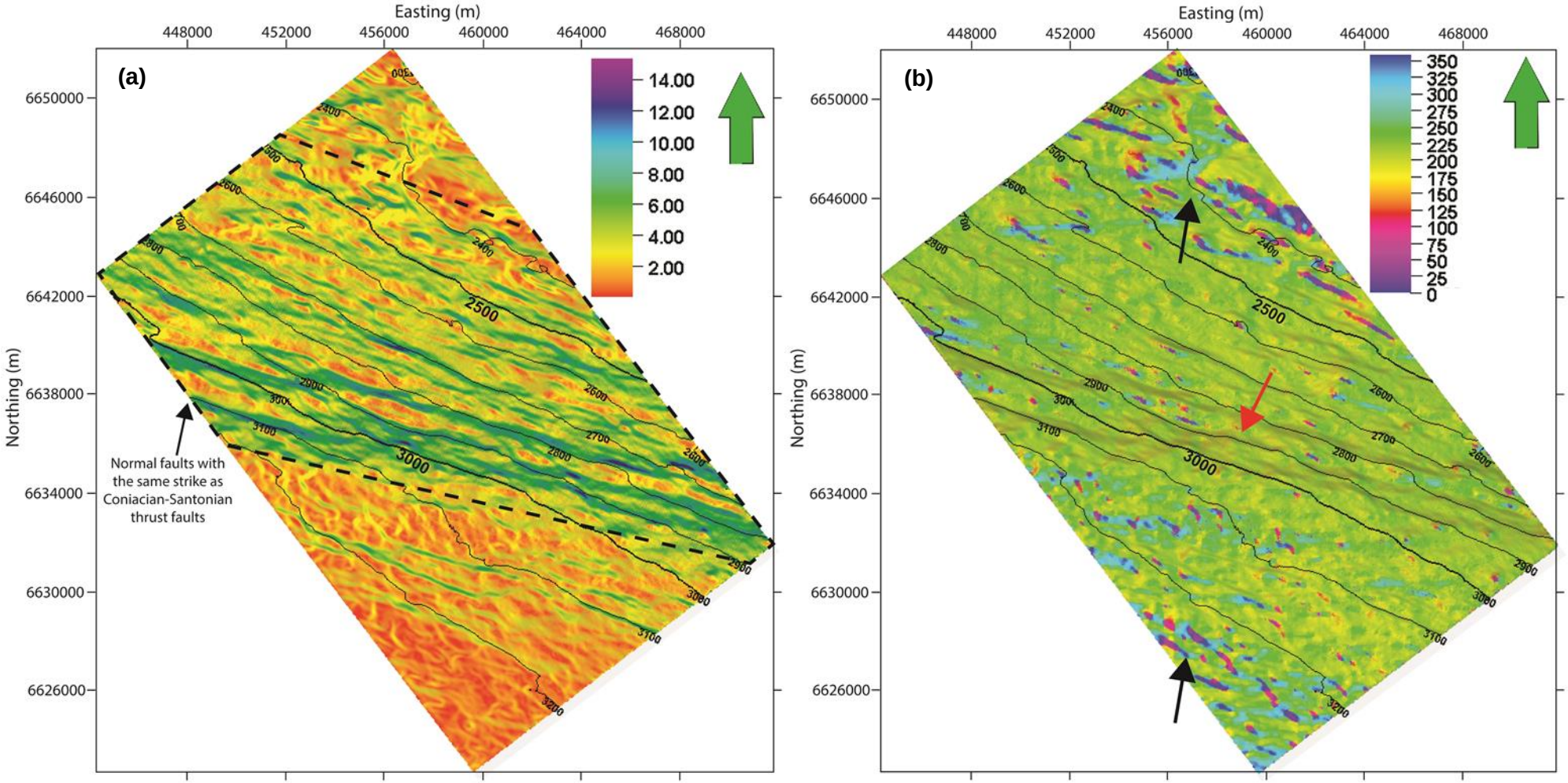


Figure 5.10. (a) A dip map of the Maastrichtian unconformity highlighting faults trending WNW-ESE with varying dip angles along the faults in the central region (marked by the dashed polygon). To the north, the faults are discontinuous and they have a NE-SW trend (indicated by blue arrow). The southern portion of the study area (below the dashed polygon) is less faulted. (b) A dip azimuth map of the Maastrichtian unconformity showing faults dipping SW-WSW in the central region of the study area (marked by the red arrow). In the northern and southern regions, the faults are dipping predominantly to the north, indicated by the black arrows. The contour interval for (a) and (b) is 100 m.

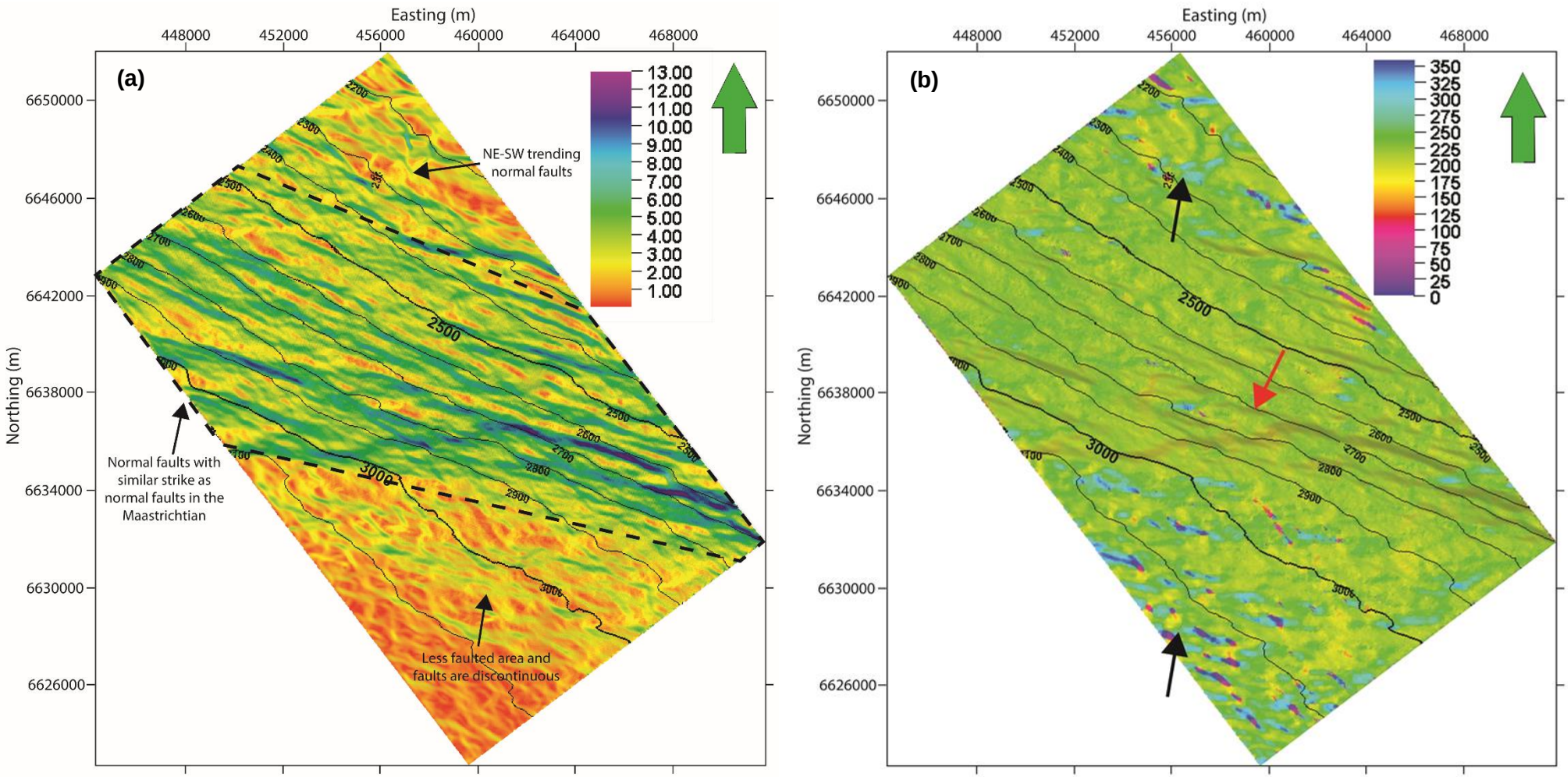


Figure 5.11. (a) A dip map of the base of the Palaeogene horizon illustrating a dense fault network trending WNW-ESE with varying dip angles along the faults in the central region of the study area (indicated by the dashed polygon). To the north, the faults are disconnected and they have a more NE-SW trend. To the south, there is less faulting and the faults are discontinuous. (b) A dip azimuth map of the base of the Palaeogene horizon illustrating faults dipping SW-WSW in the central region of the study area (indicated by the red arrow). In the northern and southern regions, the faults are dipping predominantly N to NW (indicated by the black arrows). The contour interval for (a) and (b) is 100 m.

5.2.4. Application of volumetric attributes

Based on the workflow presented in Chapter 4, the parameters used to produce the ant tracked seismic volume are presented in Table 4.1. The ant tracking algorithm was applied twice on a seismic volume on which the chaos attribute was applied. The dip and dip direction measurements of the normal faults acquired from the application of horizon-based attributes were used in the ant tracking workflow to filter out faults dipping NW and SE. The ant tracking algorithm was applied to determine the relationship between thrust faults at both the Maastrichtian unconformity and base of the Palaeogene horizon levels (i.e., whether the thrust faults propagate between the Maastrichtian and Palaeogene horizons).

The chaos attribute and ant tracking algorithm show good mapping of faults, on the Maastrichtian unconformity and base of the Palaeogene horizons, with displacement measurements of less than 12 m but greater than 6 m (Figures 5.12, 5.13, 5.14a-b and 5.15). Two sets of normal faults are detected using the ant tracking algorithm, particularly faults with N to ENE and S to WSW dip directions (Figure 5.14 and 5.15).

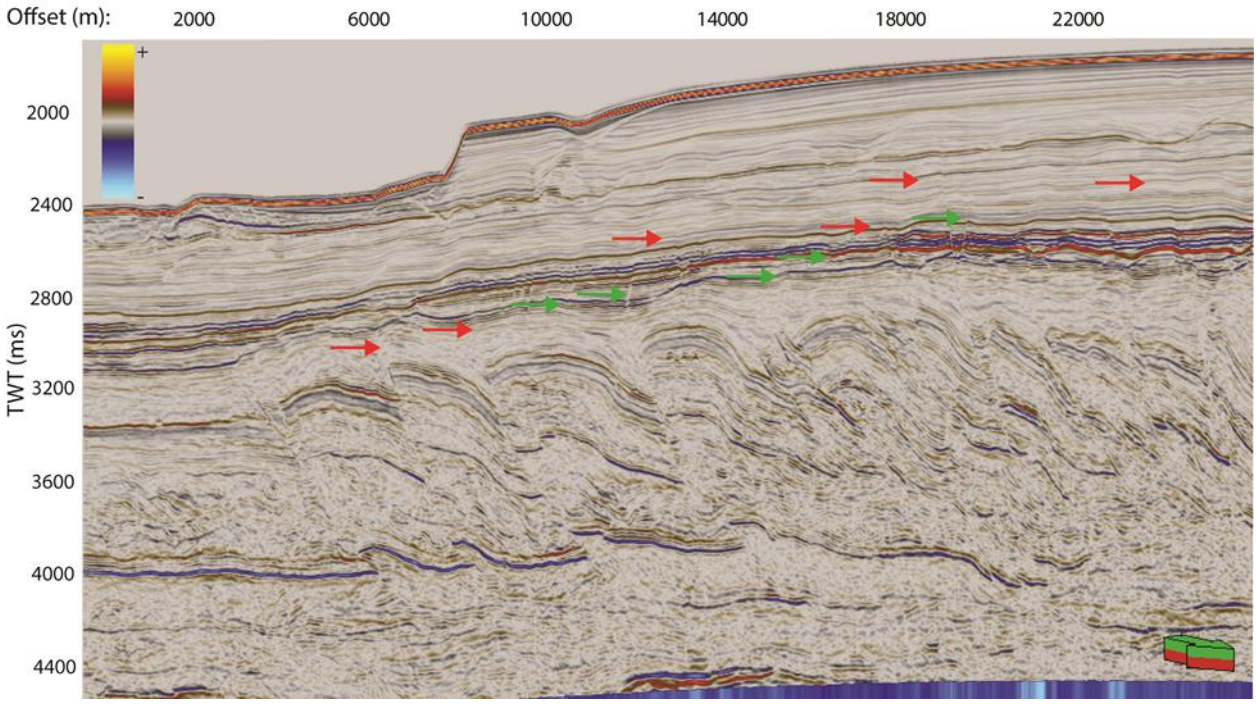


Figure 5.12. An amplitude display of inline 15648. A number of normal faults displace the Maastrichtian unconformity and base of the Palaeogene horizons. The faults indicated by the red and green arrows have displacement below the vertical resolution limit of 12 m, thus cannot be seen on the amplitude display. The vertical exaggeration (VE) of the section is 7:1.

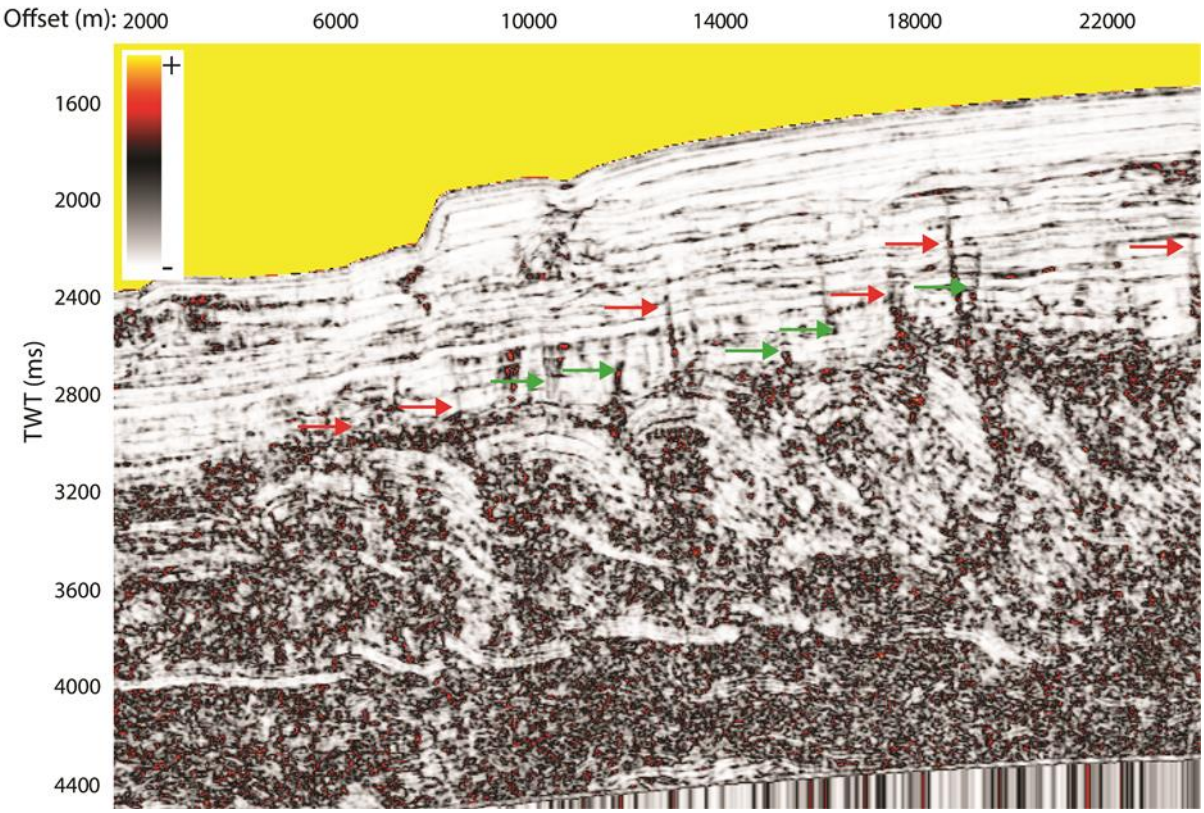


Figure 5.13. Chaos attribute applied to inline 15648 prior to ant tracking computation. The red and green arrows indicate normal faults, with fault displacement below the vertical resolution limit of 12 m, which were enhanced by the chaos attribute. Vertical exaggeration (VE) of the section is 7:1.

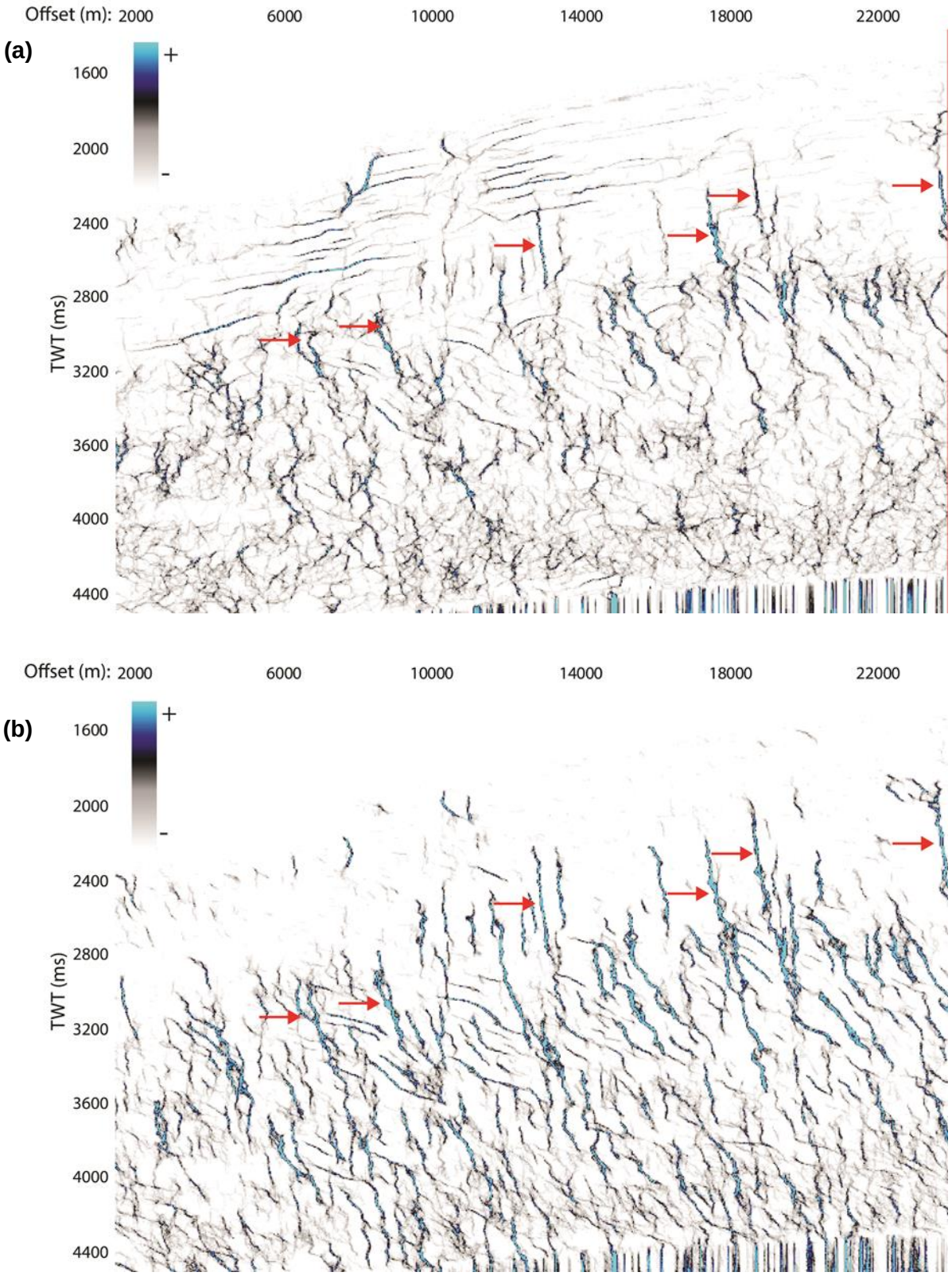


Figure 5.14. Ant tracked sections of inline 15648. These sections show the (a) first run and (b) second run of the ant tracking algorithm limited to detecting fault with a N to ENE dip direction and dip angles between 0° and 90°. A number of faults have been highlighted by the attribute. The faults marked by the red arrows are difficult to see on the amplitude seismic display. Section (a) and (b) are vertically exaggerated by a factor of 7.

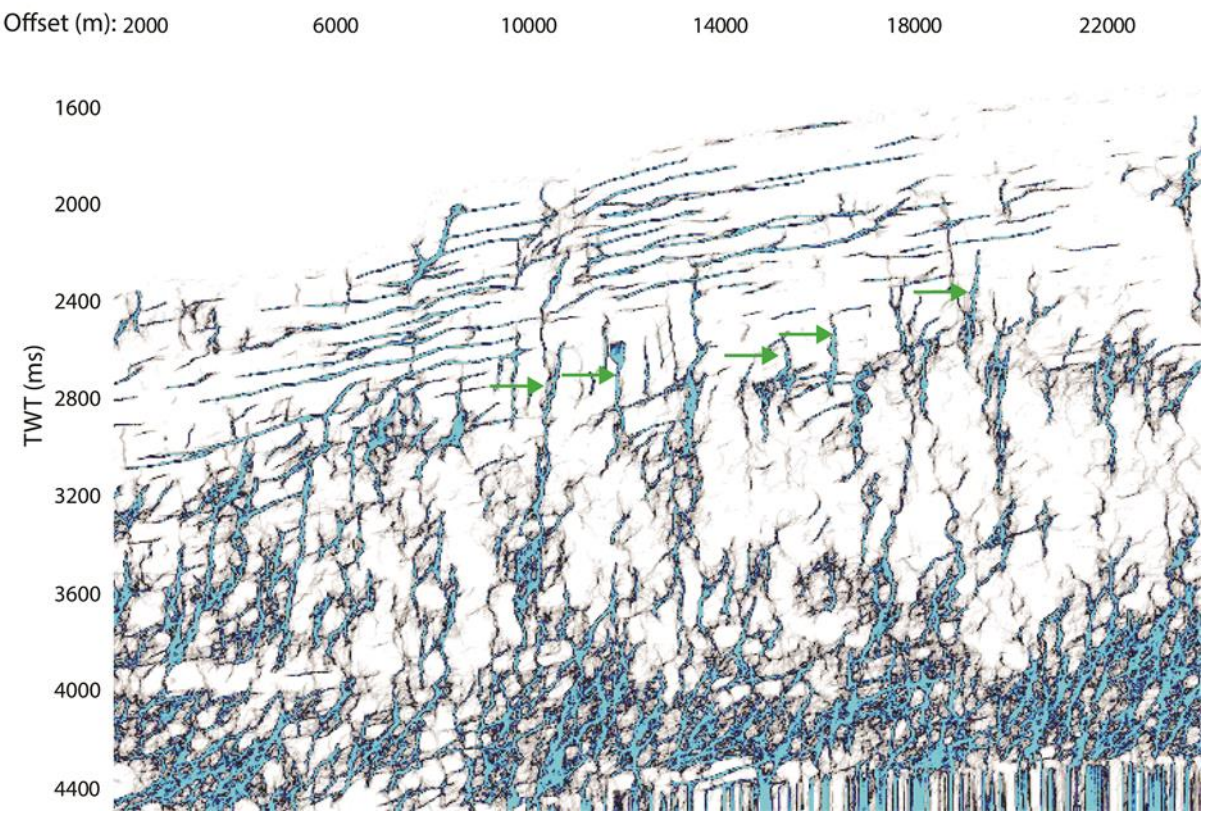


Figure 5.15. An ant tracked section of inline 15648 limited to detecting fault with a S to WSW dip direction and dip angles between 0° and 90°. A number of faults have been highlighted by the attribute. The faults marked by the green arrows are below the vertical resolution limit of 12 m. Vertical exaggeration (VE) is 7:1.

The faults dipping N to ENE are discontinuous along strike and they are less dense compared to the interconnected and denser S to WSW dipping faults (Figure 5.16a-b).

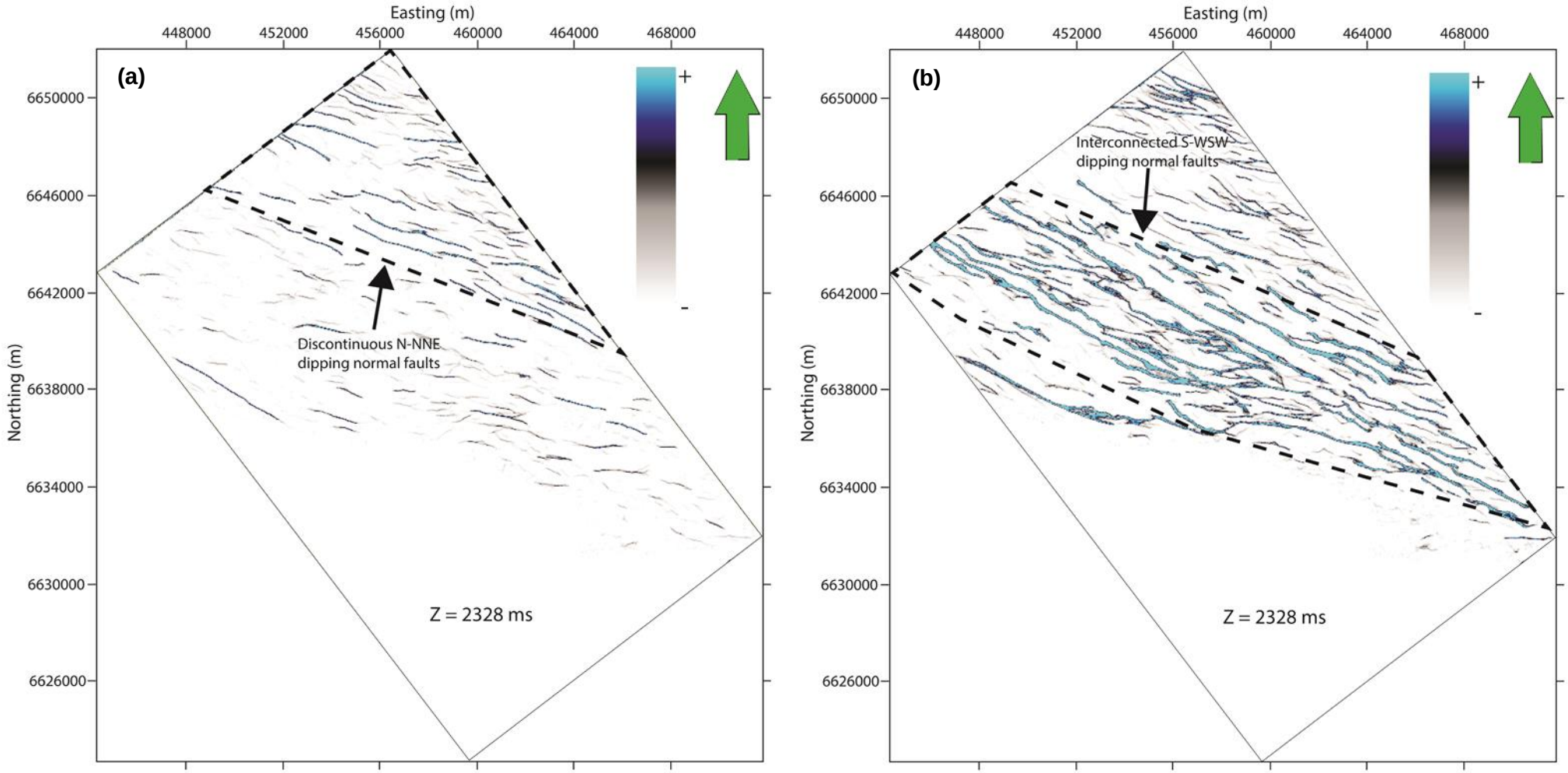


Figure 5.16. (a) Time slice of ant tracking attribute showing N to NE dipping normal faults (indicated by the dashed polygon). The first run was computed with parameters reflecting the more aggressive ants and the second run was computed with parameters reflecting the passive ants. The faults within the polygon are fragmented. (b) Time slice of ant tracking attribute showing S to WSW dipping normal faults (indicated by the dashed polygon) computed with parameters reflecting aggressive ants. The faults within the polygon are interconnected.

5.3. Interpretation and discussion

Two basal detachment layers were seismically imaged in this study; the Cenomanian-Turonian and Coniacian basal detachments. The development of detachments at multiple stratigraphic levels may be associated with overpressure occurring within the Turonian shale unit and the organic-rich shale unit at the Cenomanian-Turonian boundary (Rowan et al., 2004; see Figure 5.2b). This is in agreement with previous studies in the deepwater environment where shale units and multiple detachment levels along passive margins have been observed (Rowan et al., 2004; Briggs et al., 2006). The thickness of the shale unit that coincides with the Coniacian detachment is approximately 600 – 1000 m. However, the thickness of the organic shale unit that coincides with the Cenomanian-Turonian detachment could not be accurately determined because data were cut below approximately 4.4 s (c. 9000 m) (see Figure 5.2b). For deformation to occur above shale detachments, the amount of overpressure has to be greater than the critical-yield stress of the shale (Rowan et al., 2004). This occurs as a result of hydrocarbon generation or after a thick sedimentary package is deposited rapidly enough to increase the fluid pressure sufficiently to reduce the coefficient of friction along the basal detachments (Wu and Bally, 2000; Rowan et al., 2004). The generation of gas within the shale unit at the Cenomanian-Turonian boundary, may have resulted in increased pore fluid pressures, therefore reducing friction and enhancing slip along the basal detechment (Jungslager, 1999; Rowan et al., 2004; de Vera et al., 2010). This provided favourable conditions for gravitational failure of the margin. Gravitational failure can also be enhanced by margin uplift.

Kuhlmann et al. (2010) documented an increase in sedimentation from Cenomanian to Santonian (see Figure 5.1). The increase in sedimentation resulted in the overpressuring of the Turonian shale unit and subsequent formation of the Coniacian detachment (see Figure 5.2a-b). The detachments identified are moderately overpressured, evidence of this is the absence of shale diapirs, which are commonly found in environments with highly overpressured shale detachments (Rowan et al., 2004). The basinward limit of deformation above the Cenomanian-Turonian detachment may be due to a decrease in overpressure in the shale unit, resulting in an increase in frictional resistance to sliding and preventing

lateral movement. The basinward limit of deformation above the Coniacian detachment coincides with the front of a propagating wedge (Figure 5.17a-b) (Wu and Bally, 2000; Rowan et al., 2004).

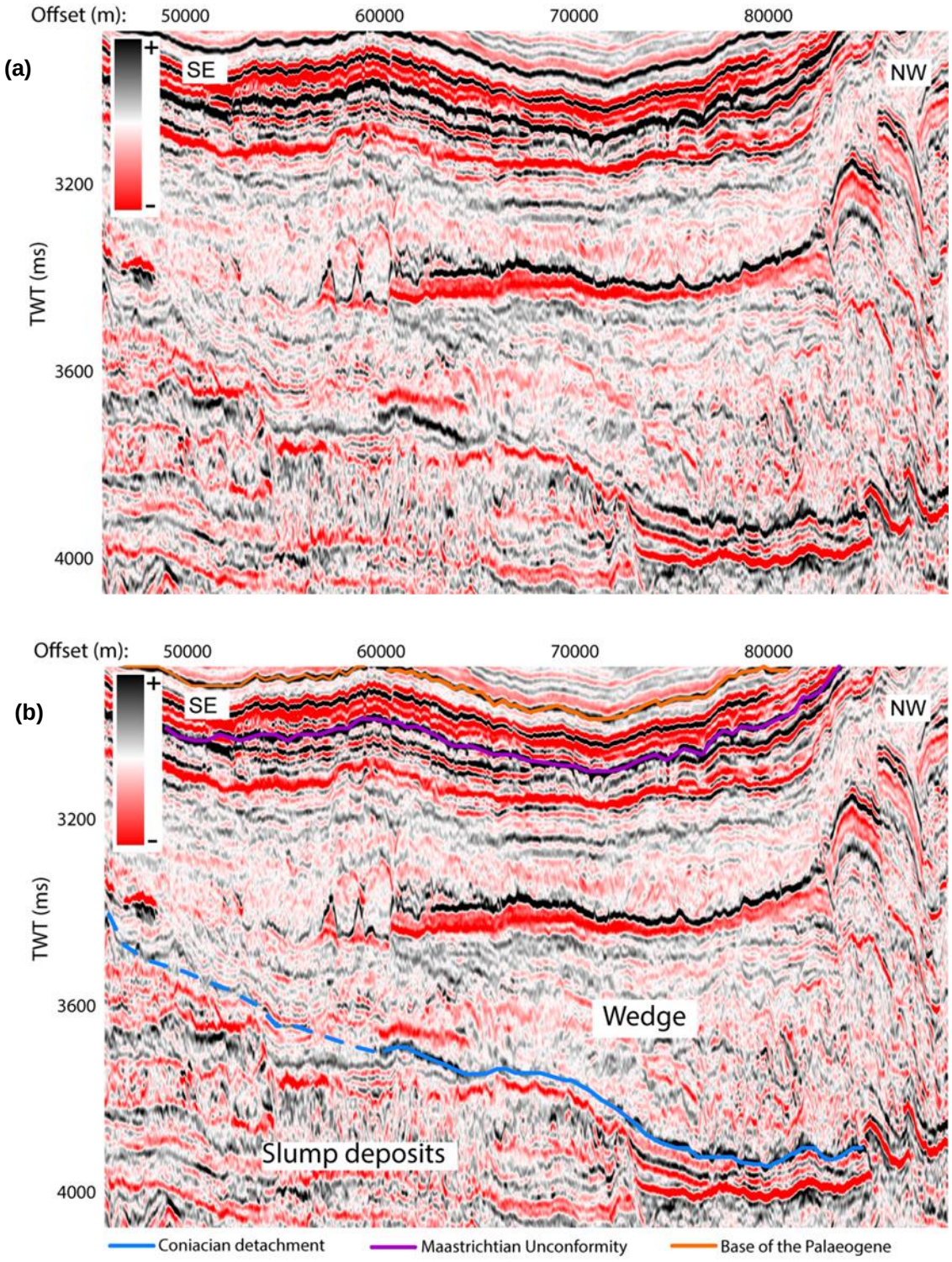


Figure 5.17. (a) Uninterpreted amplitude section. (b) Interpreted amplitude section showing the Coniacian detachment along the base of the wedge. The vertical exaggeration (VE) for (a) and (b) is 17:1

The structural styles formed in contractional domains have been previously proposed to be strongly dependent on the type of detachment layer (Rowan et al., 2004; Bilotti and Shaw, 2005). However, in the deepwater Orange Basin, the detachment layer does not have a major control on the structures formed. The data show that in the deepwater Orange Basin, the folds lack forelimbs and the backlimbs dip (4° - 24°) gentler than the fault ramps (30° - 70°), unlike the no shear fault-bend folds or fault-propagation folds, where the fault ramp and backlimb have the same dip (Morley et al., 2011). Hence, the no shear fault-bend fold and fault-propagation fold models proposed by Suppe (1983) and Suppe and Medwedeff (1990) fail to explain the fold geometry identified in the deepwater Orange Basin. The geometry of these folds can be explained by a break thrust model or a shear fault-bend model (Suppe et al., 2004; Morley et al., 2011).

Shear fault-bend folds have been documented in petroleum basins offshore Africa (e.g. the Niger delta - offshore Nigeria) (Corredor et al., 2005). Based on the shear fault-bend model proposed by (Suppe et al., 2004), only the hangingwall sequences thicken whereas in the deepwater Orange Basin, thickening was identified in the footwall and hangingwall sequences (Morley, 2009b; Figure 5.18). The displacement along faults tends to increase up the fault ramp in shear fault-bend folding (Hughes and Shaw, 2014).This differs from the displacement measurements recorded in this study, where the large displacement measurements are at the centre of the fault ramp and decrease towards the fault tip and the detachment (Figure 5.18 and Appendix A). The shear fault-bend model fails to explain the fold geometry identified in the deepwater Orange Basin. In the data, the thrust faults cut through the footwall syncline. This geometry indicates that the fold anticline formed prior to thrust development (Morley, 2009b). Thickening in the early stage folds is attributed to the movement of a number of small-scale thrust faults, therefore fold development preceded large thrust formation. Small-scale thrust faults within the fold limbs link up to form large thrusts that propagate downwards and sole into the detachments and upwards to break through the fold (Morley, 2009b). This results in large displacement measurements at the centre of the fault ramp and a decrease in displacement towards the detachment and fault tip, which is characteristic of imbricate faults formed through break thrusting (Figure 5.18).

The formation of the structural styles described in the deepwater Orange Basin favours the break thrust model.

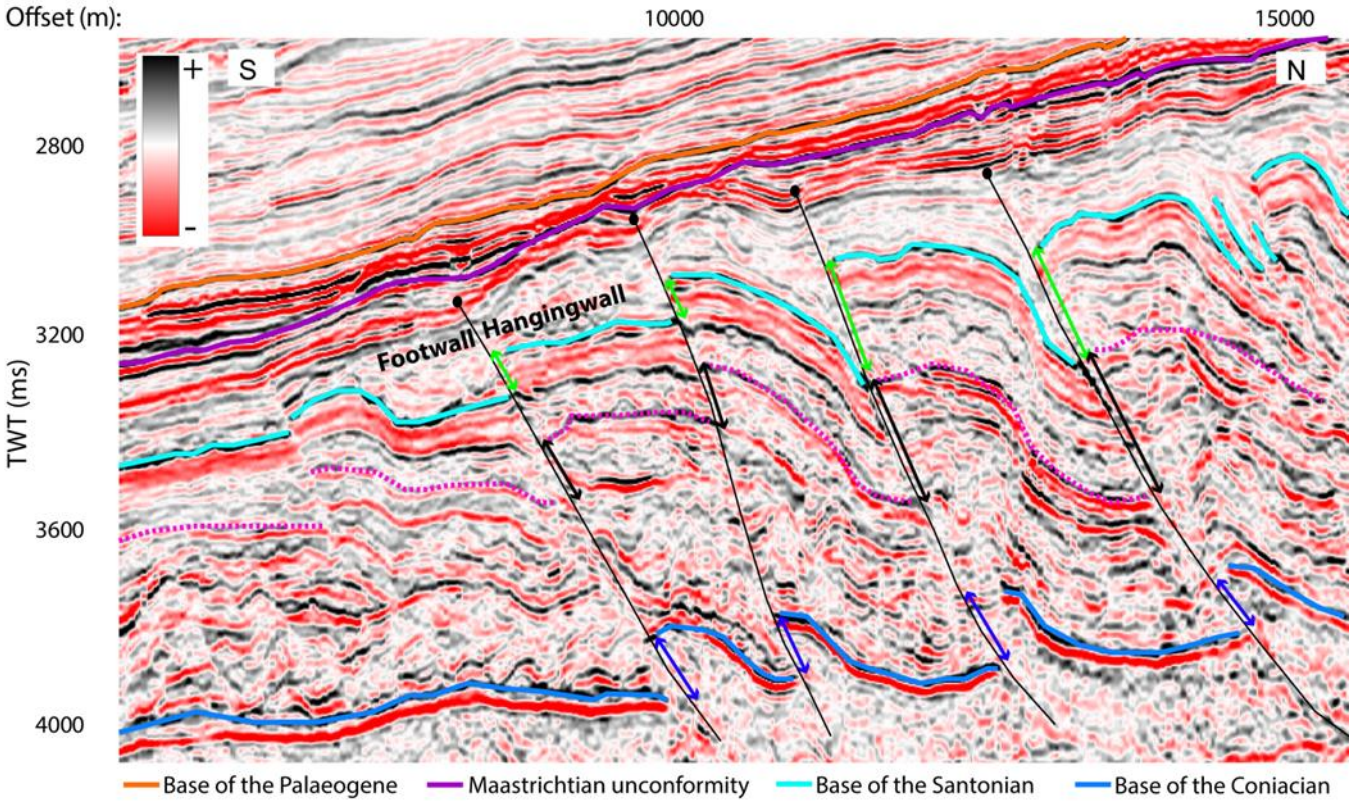


Figure 5.18. An amplitude display seismic section showing a large displacement (between the pink dotted lines) at the centre of the fault indicated by the black arrows and smaller displacement towards the detachment (indicated by the blue arrows) and fault tip (black circle) indicated by the green arrows. Faults propagate through fault limbs forming fault breakthrough folds. Both the footwall and hangingwall units are thickened, resulting in a constant thickness across dip domains. Vertical exaggeration (VE) of the section is 8:1.

The maximum distances between thrust faults are at the deformation front and they steadily decrease towards the inner part of the thrust fault system. The decrease in the distance between the thrust faults is controlled by the amount of the hangingwall block rotation (de Vera et al., 2010). Figure 5.8 presents the fault displacement measurements across the thrust fault system. The faults with the largest displacement measurements (38 - 413 m) are located in the inner part of the thrust fault system and those with smaller displacement measurements (15 m - 240 m) are located at the deformation front and rear of the system. At the rear of the system, the thrust system is linked to an extensional domain. This

zone marks the transition from extensional to compressional tectonics. The anomalies highlighted by the red circles in Figure 5.8 indicate that the fault is bifurcated.

During the Palaeogene, slumping may have caused the thrust faults to be reactivated with a normal sense of movement. Evidence of this is the link between the northward dipping and WNW-ESE trending thrust faults and the overlying normal faults with the same trend and dip direction (see Figure 5.16a). In addition, new faults with a S-WSW dip direction formed. The timing of activity of these faults will need to be fully constrained by geochronological and kinematic data.

6. STRUCTURAL CONTROLS ON POCKMARK DISTRIBUTION AND FORMATION OF SUBMARINE CANYON

6.1. Introduction

Pockmarks and submarine canyons have been documented from coastal regions to deepwater settings (Çifçi et al., 2003). Pockmarks are depressions on the seafloor with a circular to elongate geometry. Formation of pockmarks is as a result of episodic fluid expulsion (Kelley et al., 1994; Hovland et al., 2002; Çifçi et al., 2003; Anka et al., 2014). Submarine canyons are described as steep and deep incisions on the seafloor that act as pathways for mass movement of sediments, as gravity-driven slump events, from the shelf to the deepwater environments (Lastras et al., 2011). Faults can become conduits for fluid and gas migrating to the seafloor (Cole et al., 2000; Cifci et al., 2003). Pockmarks may occur as isolated features in fields covering several tens of square kilometres. Generally, their diameters range from 10 to 200 m and may reach diameters of 1000 m (Hartwig et al., 2012). In some areas, large pockmarks with diameters greater than 10 km have been documented (Davy et al., 2010). Their size is as a result of the capacity, overpressure and the composition of the fluid supplying the pockmark. Pockmarks are important sedimentary features because they provide direct evidence for fluid migration and they can be used to identify conduits for fluid migration (Cole et al., 2000). In the Orange Basin, pockmarks with a NNE-SSW trend and diameters between 170 m and 520 m have been identified along the continental shelf using 2D and 3D reflection seismic datasets.

The pockmarks and submarine canyon are the first seafloor structures to be recorded in the deepwater Orange Basin. The identification of these structures was made possible by the availability of 3D reflection seismic data. Due to the wide line spacing of 2D seismic surveys in deepwater settings, features could not be delineated without spatial aliasing. It is important to determine the origin of these structures and the mechanisms that affect their activation or reactivation to provide a more detailed understanding of processes influencing the topography of the present day seafloor.

6.2. Results

6.2.1. Pockmarks

The northeastern region within the study area, is characterised by elongated depressions trending subparallel to the continental slope in water depths of approximately 2000 ms (roughly 2000 m) (Figure 6.1a). The seafloor depressions are interpreted as pockmarks based on their dimensions and 3D geometry. Figure 6.1a is a depth structure map of the seafloor horizon, illustrating the mapping of pockmarks by the seismic data. To enhance the detection of pockmarks, dip (Figure 6.1b) and dip azimuth (Figure 6.1c) attributes were computed for the seafloor horizon. These attributes provided better mapping resolution than the depth structure map. Furthermore, the morphology, distribution and orientation of the pockmarks are better enhanced by the edge detection attribute map compared to both the dip and dip azimuth attribute maps (Figure 6.1d). Six pockmarks were identified with diameters between 700 m and 1100 m and depths between 75 m and 103 m with the largest pockmark located at the edge of the study area (Figure 6.1d). The pockmarks are elongated in a WNW-ESE direction (Figure 6.1d).

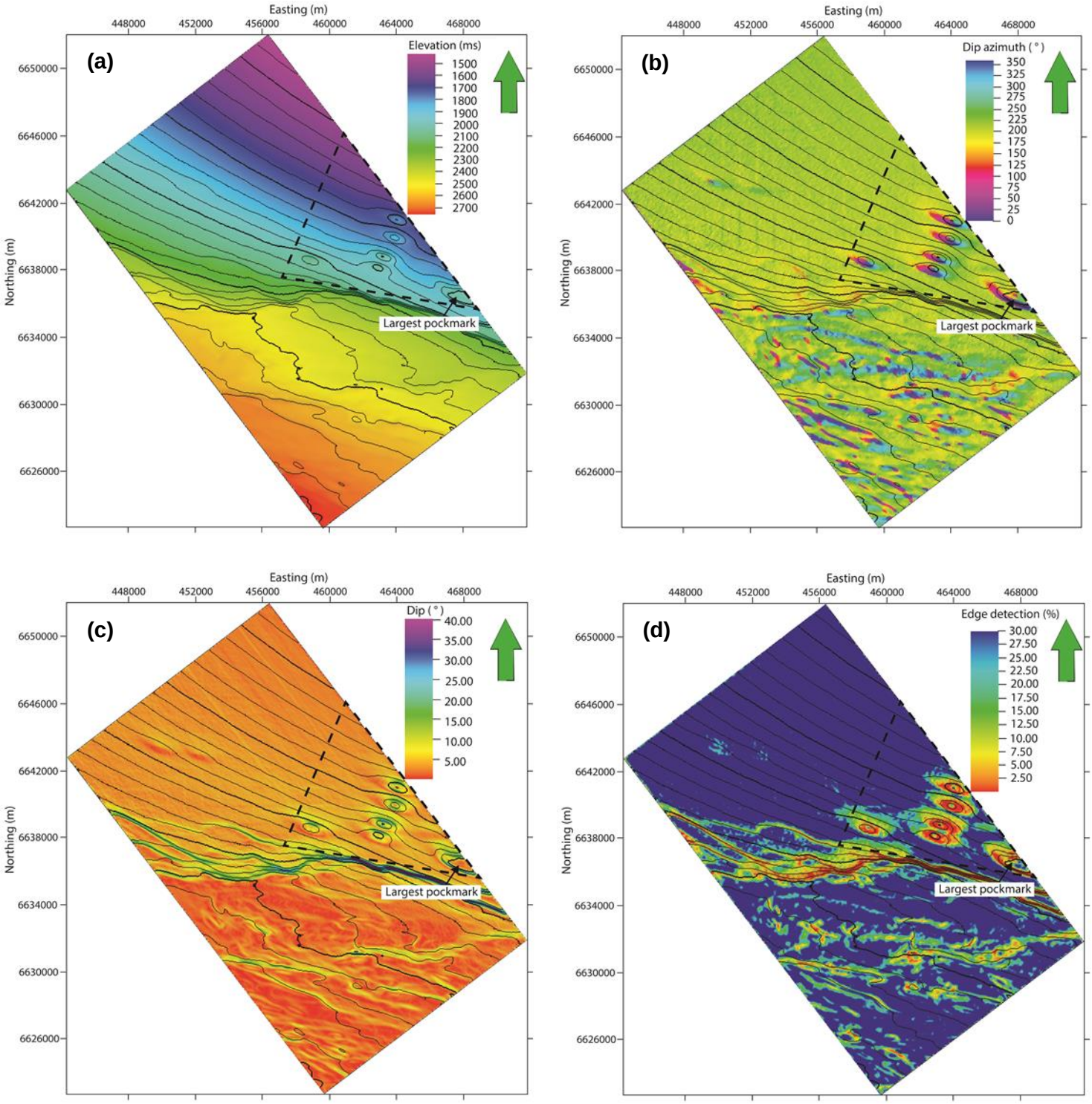


Figure 6.1. (a) A depth structure map, (b) dip azimuth map, (c) dip map and (d) edge detection map of the Holocene seafloor highlighting the pockmarks identified in the study area (black dashed polygon). The contour interval for all the maps is 50 m.

The ant tracking algorithm was computed to delineate structures that are possible conduits for fluid migration to the seafloor. The thrust faults that propagated into the younger sedimentary sequences with a normal sense of movement were limited and they were terminated in the early Palaeogene (Figure 6.2). The thrust faults exploited S-SW dipping normal faults and the normal faults terminate at the base of the pockmarks (Figure 6.3).

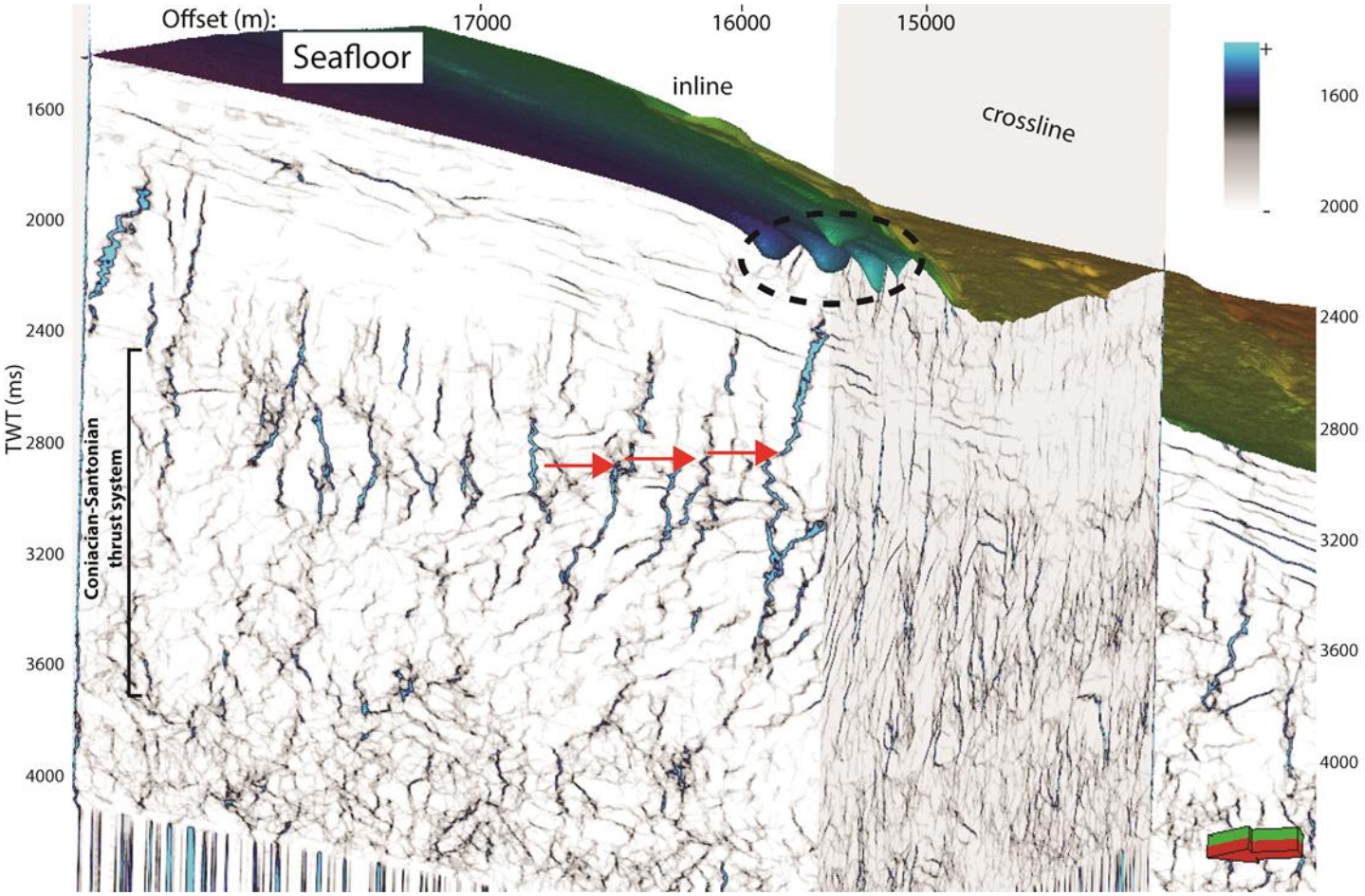


Figure 6.2. Ant tracked volume with the stereonet filter applied to detect faults dipping N-ENE. A number of faults have been highlighted above the Coniacian-Santonian thrust fault system. The normal faults indicated by the red arrows are linked to the thrust faults. The normal faults terminate in the Palaeogene. The pockmarks are shown by the dashed ellipse. Vertical exaggeration (VE) is 7:1.

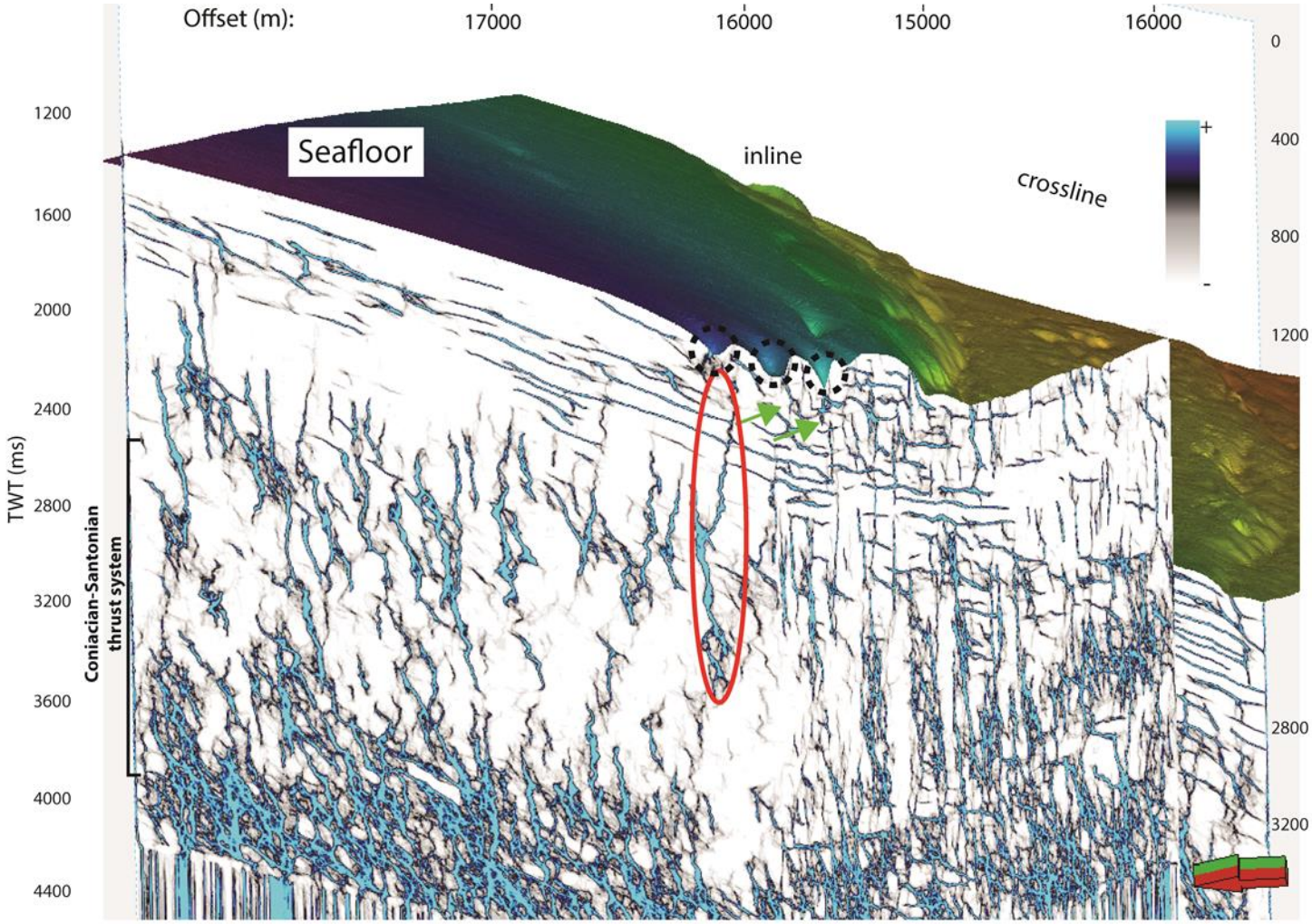


Figure 6.3. Ant tracked volume with stereonet filter applied to detect fault with a S-WSW dip direction. The green arrows indicate the termination of the S-WSW dipping normal faults below pockmarks. The red ellipse shows the connectivity between thrust fault and normal fault that propagated to the surface beneath the pockmarks (marked by black dashed circles). Vertical exaggeration (VE) is 7:1.

6.2.2. Submarine canyon

One submarine canyon was recorded on the seafloor on the lower slope. The canyon wall trends parallel to pockmarks and the Coniacian-Santonian thrust faults (Figures 6.4 and 6.5). The submarine canyon is 45 km wide and incised to depths of 650 m (Figure 6.4). The maximum slope dip recorded along the walls of the canyon was 50°. The slope dip progressively decreases westward along the canyon wall to approximately 25° (Figure 6.5). The canyon was mapped at water depths of approximately 2000 m. The length of the canyon could not be determined as it extends out of the study area. The submarine canyon formed above the deformation front of the Coniacian-Santonian thrust fault system (Figure 6.4).

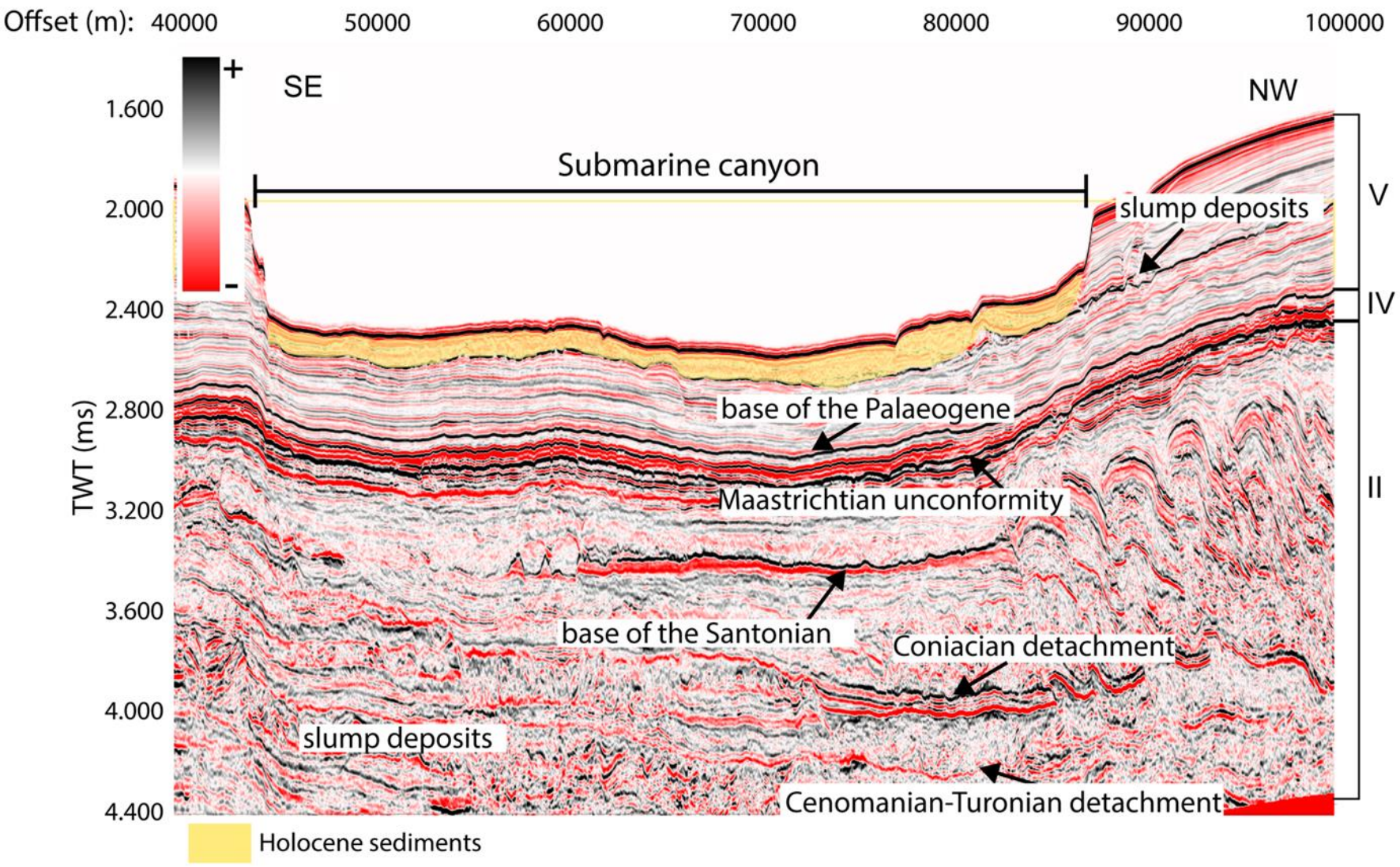


Figure 6.4. An amplitude display seismic section illustrating the structures imaged in the deepwater Orange Basin. The submarine canyon is formed above the deformation front of the thrust fault system. It has a width of 45 km and is incised to depths of approximately 650 m. The vertical exaggeration (VE) of the section is 17:1.

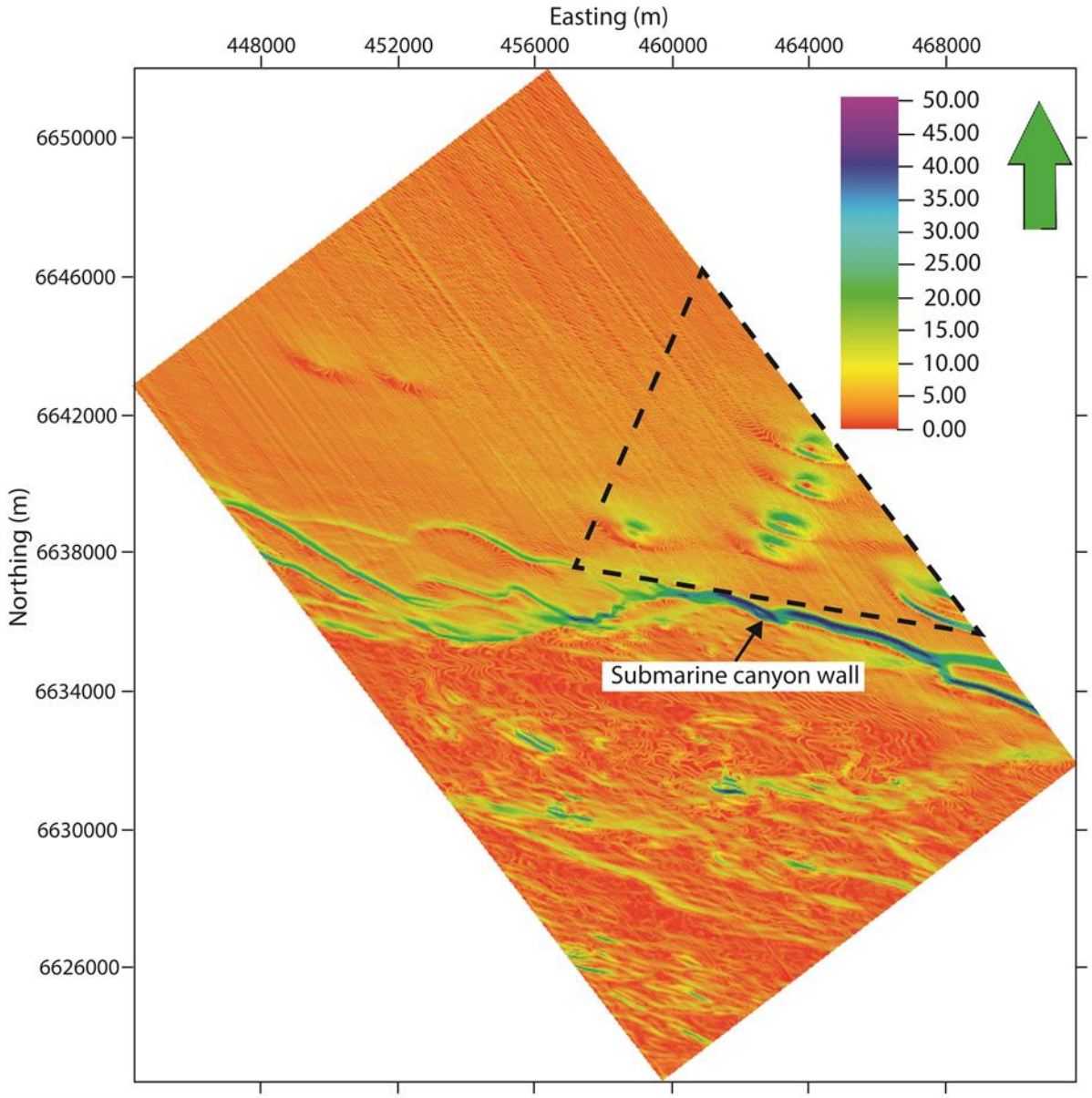


Figure 6.5. A dip map of the seafloor horizon highlighting the dip of the canyon wall and pockmarks, in the area marked by the dashed polygon.

6.3. Interpretation and discussion

Based on the morphology of the seafloor on the lower slope of the Orange Basin, determined from 3D reflection seismic data, the processes responsible for the formation and development of pockmarks and submarine canyons can be inferred.

Pockmarks are commonly accepted to have formed by the migration or expulsion of hydrocarbons to the seafloor (Kelley et al., 1994; Hovland et al., 2002; Çifçi et al., 2003; Gay et al., 2006; Anka et al., 2014). Pockmarks were identified in the northeastern region within the study area. They cover an area of approximately 31 km^2. The concentration of pockmarks in the deepwater Orange Basin is much lower compared to the pockmark concentration documented by Hartwig et al. (2012) on the continental slope. This is due to the absence of polygonal fault patterns in the shallow sediment, thus the primary control is interpreted to be tectonic related. The pockmarks are limited to areas with abrupt changes in the underlying sequences; this makes them less common and large. Based on the results, the WNW-ESE oriented pockmark arrangement correlates with the strike of the Coniacian-Santonian thrust fault system. The pockmarks formed from a deep hydrocarbon source because the results show no evidence of shallow gas pockets beneath the pockmark (Pilcher and Argent, 2007). They were only observed above the thrust faults that are attached to the Cenomanian-Turonian shale detachment layer. Various authors (Jungslager, 1999; Aldrich et al., 2003; Van Der Spuy, 2003; Hartwig et al., 2012) have proposed that the shale unit along the Cenomanian-Turonian boundary is a possible gas-prone source rock. This overpressured shale unit may be a possible gas source for the formation of pockmarks on the seafloor. The thrust faults serve as conduits for the migration of gas to the seafloor. These thrust faults exploit the S to SW dipping normal faults which transport the gas to the seafloor to form pockmarks (see Figure 6.3). The pockmarks are elongated in a WNW-ESE direction and form a linear array along the submarine canyon (see Figure 6.1d). Pilcher and Argent (2007) observed the same arrangement on the slope offshore Gabon and they proposed that these pockmarks formed as a result of gravitational slumping on unstable slopes causing the pockmarks to localise into linear arrays. Alternatively, the WNW-ESE elongation of the pockmarks is possibly due to a number

of small, discrete and circular pockmarks coalescing to form a single pockmark that is elongated through scouring and deepwater bottom currents (Pilcher and Argent, 2007).

The submarine canyon is a single valley that runs straight down the lower continental slope. Huang et al. (2014) proposed that this typical morphology formed by the erosion of a thick and relatively uniform sedimentary sequence on the continental slope, with headward erosion driving the development of the canyon. The development of submarine canyons is attributed to two processes: 1. slumping and mass wasting; and 2. turbidity currents derived from sources on the shelf and upper continental slope. These processes are interpreted to have acted at different times and in conjunction to influence the formation and development of submarine canyons (de Almeida et al., 2015). The possibility that the submarine canyon formed by sediment supply from the Orange River mouth has been ruled out due to the canyon trending in the opposite direction to the Orange River mouth. Tectonics has had a control on the formation of the deepwater Orange Basin canyon by slumping and other mass wasting events occurring along the continental slope. Two slumping events were recorded in the deepwater Orange Basin; one occurring during the Coniacian to Santonian and the other in the Late Cenozoic (see Figure 6.4). The data presented suggest two possible ways in which the submarine canyon formed: 1.the canyon formed solely by the slumping event during the Coniacian to Santonian or solely by the slumping event in the Late Cenozoic; and 2. the Coniacian to Santonian and Late Cenozoic slumping events acted individually and in conjunction to influence the formation of the submarine canyon.

Formation by solely Coniacian-Santonian slumping or solely Late Cenozoic slumping

Continental margin instability resulted in the collapse of the margin under the influence of gravity and subsequent transportation of sediments downslope. The gravitational slumping event that occurred during the Coniacian to Santonian is indicated by the development of extensional growth faults, toe-thrust faults and fault-related folds on the slope and large-scale deposits related to slumping at the base of the lower slope (Brown et al., 1995; Seranne and Anka, 2005; Broad et al., 2006; de Vera et al., 2010; Kuhlmann et al., 2010). Sedimentary sequences in the area dominated by thrust faults are upthrown whereas the area with the slump deposits sags. The Maastrichtian to Quaternary sedimentary sequences mimick the geometry of the underlying Coniacian-Santonian sequence, which was formed by

gravitational slumping (see Figure 6.4). This results in the canyon developing in an area where there has been subsidence. Once the canyon is formed, Holocene sediments are deposited (see Figure 6.4). The shortfall of this hypothesis is that it does not explain the differences in the reflective character of the sedimentary sequences found adjacent to the walls of the canyon and the sequences found below the canyon. If the canyon formed as a result of subsidence, the reflectors below the seafloor adjacent to the walls of the canyon should continue below the canyon, analogous to the Maastrichtian unconformity and base of the Palaeogene reflectors, as opposed to terminating on the canyon walls (see Figure 6.4).

Evidence of Late Cenozoic slumping is indicated by the chaotic reflectors in the Cenozoic sedimentary package (post-rift sequence V) (see Figure 6.4). Formation of the submarine canyon by solely Late Cenozoic slumping explains the termination of reflectors on the canyon wall. Gravitational collapse of the margin during the Cenozoic resulted in the transportation of large slump deposits downslope leading to erosion of the seafloor at that time and subsequent formation of the canyon. The chaotic reflectors of the slump deposit coincide with the base of the canyon and the sedimentary sequences below the chaotic reflectors continue below the base of the canyon. Canyons are conduit for sediments. As Holocene sediments pass through the canyon, the sediments are deposited (see Figure 6.4) . This theory fails to explain the pervasive nature of the submarine canyon with depth.

Formation by a combination of both the Coniacian-Santonian and Late Cenozoic slumping

The formation of the submarine canyons by a combination of the Coniacian to Santonian and Late Cenozoic slumping events detailed above is the most favourable hypothesis. The early development of the canyon was due to subsidence and was structurally controlled. This was followed by Cenozoic slumping which further eroded the submarine canyon. This hypothesis explains the pervasive nature of the submarine canyon with depth as a result of the Coniacian to Santonian slump deposits causing a zone of subsidence where the submarine canyon formed. The termination of the reflectors on the canyon wall can be explained by Cenozoic slumping where large volumes of sediment deposited downslope eroded the walls of the canyon (see Figure 6.4).

7. DISCUSSION

7.1. Seismic attributes

The detailed seismic processing of the 3D seismic data from the deepwater Orange Basin offered great advantages for interpretation of the stratigraphic units and the Coniacian-Santonian thrust fault system. One of the main limitations of using conventional interpretation techniques is that they do not allow for better delineation of faults with displacement measurements below the vertical resolution limit. In this study, the conventional seismic interpretation techniques are supplemented with the application of horizon-based and volumetric seismic attributes to enhance the detection of faults that fall between 12 m and 6 m. The high-resolution prestack time-migrated 3D seismic data used in this study serves as a base on which high-level seismic attributes were computed. For example, the third-order normal faults (dipping 4° - 12° N-ENE and S-WSW) that displace the Maastrichtian and Palaeogene units, have been mapped with a high level of confidence using the dip, dip azimuth, edge detection and ant tracking attributes.

The ant tracking attribute was applied to increase confidence in structural interpretation and reduce bias associated with the interpretation of faults on seismic data. The ant tracked volume has revealed the continuity of the Coniacian-Santonian thrust faults into the Maastrichtian and Palaeogene units, with a normal sense of movement. This represents reactivation of the thrust fault system as a result of slumping during the Palaeogene. This deformation event has been described by Dingle (1980). However, the timing of activity of these faults will need to be fully constrained by geochronological and kinematic data. In addition to mapping the thrust faults, the ant tracking algorithm sucessfully mapped S-WSW dipping normal faults and revealed the relationship between these normal faults, Coniacian-Santonian thrust faults and pockmarks. The Coniacian-Santonian thrust faults exploit the S-SW dipping normal faults and form conduits for gas migration to the seafloor to form pockmarks. Evidence for this is the termination of SW dipping normal faults beneath the pockmarks and the pockmarks exhibit the same trend (WNW – ESE) as the thrust faults and S-SW dipping normal faults, highlighted by the dip azimuth attribute. Futhermore, the ant tracking attribute shows the dense network

of the S-WSW dipping normal faults compared to the sparse and disconnected N-ENE dipping normal faults.

The application of seismic attributes proved to be successful in imaging complex subsurface geometries. The attributes have highlighted faults displacing the Maastrichtian and Palaeogene units. The ant tracking attribute has further highlighted the structures likely to have a control on the migration of hydrocarbons to the seafloor to form pockmarks.

7.2. Basin evolution from Cenomanian to Quaternary

The main mechanism driving gravity failure in the Orange Basin has been interpreted to be margin uplift causing a basinward tilt of the margin along with post-rift thermal subsidence. Shelf margin progradation has had a minor control on the initiation of gravitational tectonics (Granado et al., 2009; de Vera et al., 2010). Episodic gravitational collapse of the margin from Cenomanian to Santonian caused rapid deposition of thick sedimentary packages. Kuhlmann et al. (2010) reported the highest sedimentation rates during the Cenomanian to Santonian. The formation of the Cenomanian-Turonian detachment was as a result of gas generation in the organic-rich shale unit along the Cenomanian-Turonian boundary. This resulted in an increase in pore fluid pressure decreasing friction and enhancing slip along the detachment (Jungslager, 1999; Rowan et al., 2004; de Vera et al., 2010). This provided conditions that favoured gravity failure of the margin (de Vera et al., 2010). Rapid deposition of sediment caused overpressuring of the Turonian shale unit and subsequent formation of the Coniacian detachment (Rowan et al., 2004). The basinward dip of the Cenomanian-Turonian (see Figure 5.3) detachment suggests that the main mechanism driving deformation above the detachments was gravity sliding as opposed to gravity spreading, which was proposed by Rowan et al. (2004). Gravity sliding is defined as the component controlled by the basinward slope of the detachment and gravity spreading is affected by the surficial slope of the seafloor (Rowan et al., 2004). A steeply dipping detachment decreases the resistance of slip on the basal detachment (Brandes and Tanner, 2014).

Previous studies (Rowan et al., 2004; Corredor et al., 2005; Hughes and Shaw, 2015) proposed that the structural styles in deepwater fold belts are strongly dependent on the detachment layer where faults propagate upwards from the detachment. However, the structural styles in the deepwater Orange Basin developed independently from the detachments. The break thrust model explains the development of the fault and fold geometries identified in the deepwater Orange Basin. Rapid deposition of thick sedimentary sequences from the Coniacian to the Santonian resulted in the formation of the Coniacian detachment and was followed by early stage fold development. These folds are similar to detachment folds, however they do not occur above a detachment and they are asymmetric (Morley, 2009b). Throughout fold growth, the Coniacian detachment zone continues to propagate laterally beneath the folds (Woodward, 1997). Numerous small-scale thrust faults develop within the forelimb and the movement of these faults causes thickening within the footwall and hangingwall sequences (Morley, 2009b). The small-scale thrust faults link up to form larger thrust faults that propagate downwards and sole into the Coniacian detachment and upwards to break through the fold and form an imbricate system of breakthrough folds (Morley et al., 2018; Figure 7.1). The thrust faults that sole into the Cenomanian-Turonian detachment were not captured by the Coniacian detachment; therefore they continued to propagate downwards and were terminated at the Cenomanian-Turonian detachment (Figure 7.1 and Appendix B). The one distinguishing characteristic of break thrusts is that the maximum displacement is at the centre of the fault ramp and displacement decreases downwards to the detachment and upwards towards the fault tip (Morley, 1994). At the toe of the thrust system, there is an accumulation of large slump deposits. The area above the slump deposits subsides and the area above the thrust faults is uplifted.

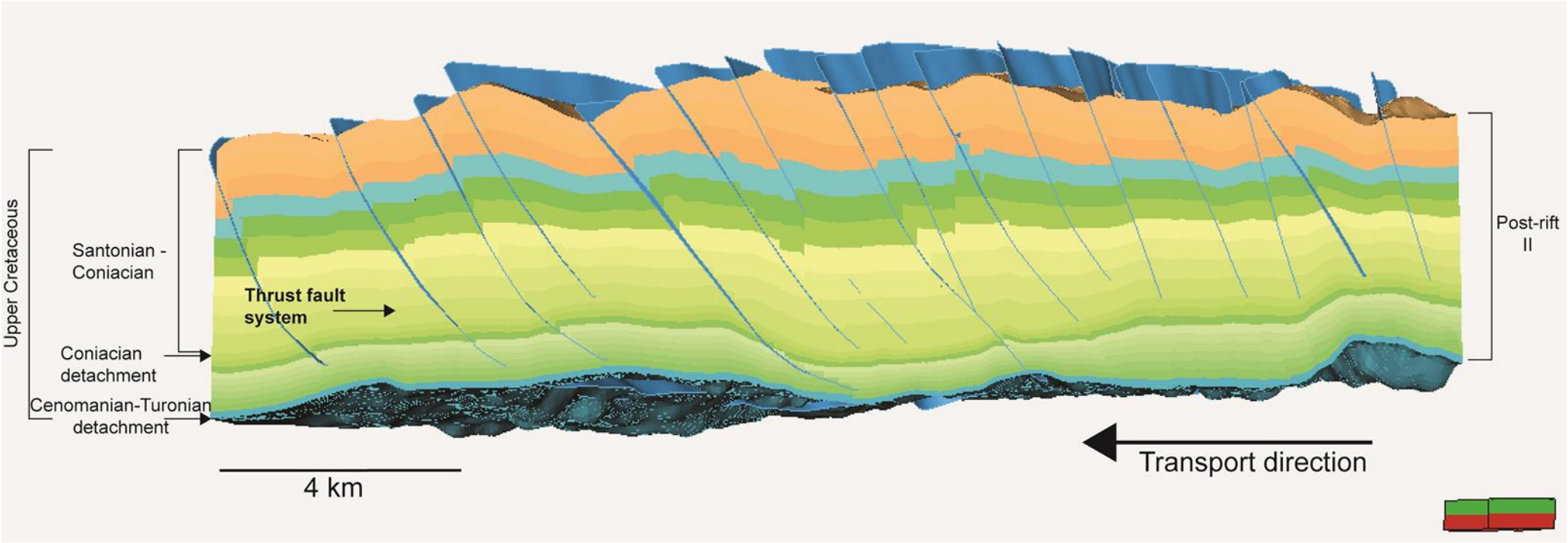


Figure 7.1. 3D model showing landward-dipping thrust faults becoming slightly curved as they attach to the Cenomanian-Turonian detachment. The thrust faults that connect to the Coniacian detachment maintain a planar geometry. The full 3D model animation can be viewed in the attachment.

During the Palaeogene, sedimentation rates were slow and margin uplift continued. Cenozoic slumping occurred at a time when sedimentation rates were slow and the rate of thermal subsidence was decreasing. The erosion of the continental shelf is associated with uplift of the western margin of southern Africa and a major sea level lowstand during the Oligocene (Cramez and Jackson, 2000; Lavier et al., 2001; Wigley and Compton, 2006). Seranne and Anka (2005) and Kuhlmann et al. (2010) proposed that the slumping is related to a stratigraphic shale unit that formed a detachment surface at the base of the Palaeogene. This provided a favourable environment for pre-conditioning of the slump. However, Hirsch et al. (2010) proposed reactivation of older growth faults and toe-thrust systems on the continental slope as a pre-conditioning factor for slumping. Margin uplift may have increased the basin tilt and as a result favoured gravity sliding, leading to gravitational failure during the Late Cenozoic. This resulted in the formation of normal faults in the Maastrichtian and early Palaeogene units. The Coniacian-Santonian thrust faults were reactivated with a normal sense of movement. The reactivation of thrust faults dipping N and the formation of new normal faults dipping N-ENE and S-WSW in the Maastrichtian, formed cross-cutting relationships between the faults (Figure 7.2a-b and Appendix B). The thrust faults that sole into the Cenomanian-Turonian detachment exploit the S-SW dipping normal faults for the transportation of gas, possibly from the source rocks at the Cenomanian-Turonian boundary, to the surface to form pockmarks (Figure 7.3 and Appendix B). The pockmarks are elongated in a WNW-ESE direction, which follows the trend of the Coniacian-Santonian thrust fault system and the trend of the submarine canyon. They form a linear array which is characteristic of pockmarks formed by gravitational slumping. The linear array of elongated pockmarks is also characteristic of pockmarks that formed as a result of scouring and deepwater bottom currents. The pockmarks are elongated in the direction of the current (Pilcher and Argent, 2007). The submarine canyon formed by a combination of the Coniacian to Santonian and Late Cenozoic slumping events. A zone of weakness was created by the Coniacian to Santonian slumping event. This resulted in the subsidence of sedimentary sequences at the deformation front. This was followed by the Late Cenozoic slumping event which eroded the slope to form the canyon.

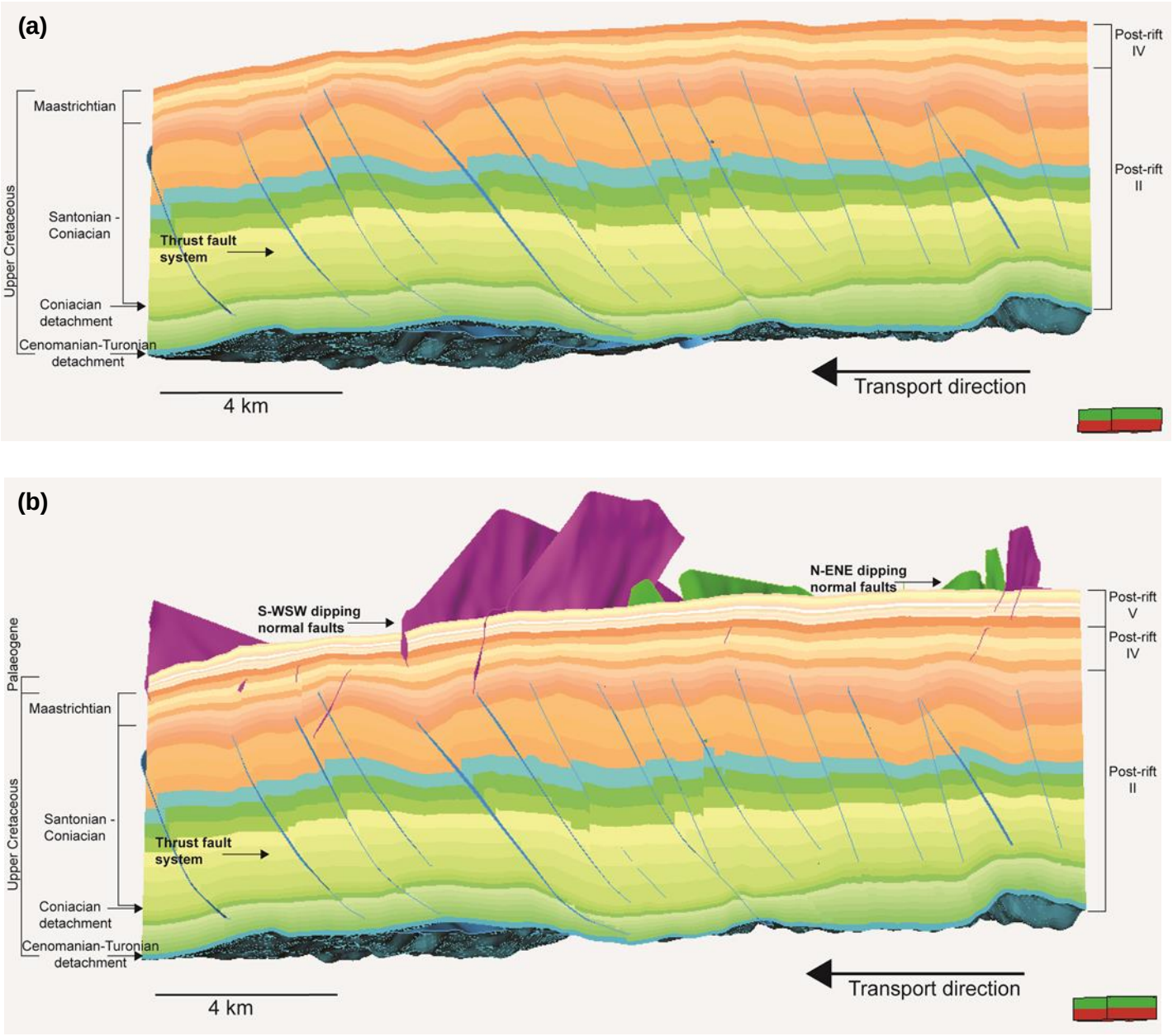


Figure 7.2. 3D model illustrating deposition of (a) Maastrichtian and (b) early Palaeogene units before formation of N-ENE and W-WSW dipping normal faults. The S-WSW dipping normal faults intersect some of the Coniacian-Santonian thrust faults. The N dipping normal faults are reactivated thrust faults. The continuation of the thrust faults into the Palaeogene is not visible in this view of the model. The full 3D model animation can be viewed in the attachment.

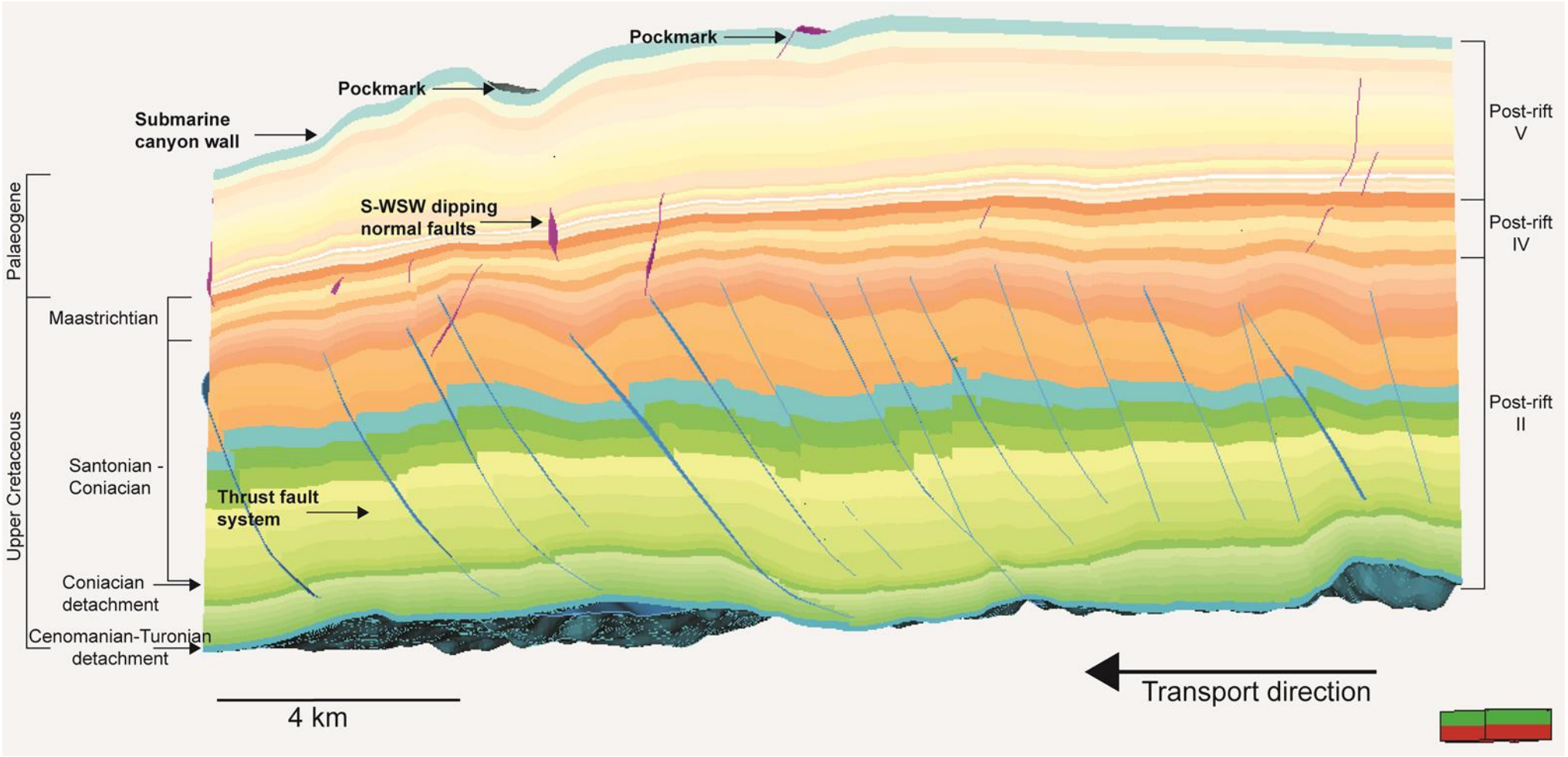


Figure 7.3. 3D model showing the stratigraphic units and their corresponding megasequences identified in the deepwater Orange Basin and the intersection of S-WSW dipping normal faults with the base of the pockmark. The continuation of the thrust faults into the Palaeogene is not visible in this view of the model. The full 3D model animation can be viewed in the attachment.

7.3. A comparison between the Orange Basin shelf and upper slope versus lower slope environments

The listric extensional fault system recorded in the upper slope and the thrust fault system in the lower slope sole onto a common detachment layer, the Cenomanian-Turonian shale detachment (Scarselli et al., 2016). The results presented in Chapter 5 indicate the presence of a second shale detachment at the base of the Coniacian on the lower slope. This detachment layer has not been documented on the upper slope. A possible explanation for this is that the Turonian shale unit on the upper slope is not overpressured, resulting in resistance to slip; therefore deformation does not take place.

Using the classification system by de Vera et al. (2010), three post-rift sequences were identified in the study area; post-rift sequence II, IV and V (see Figures 5.1 and 7.3). Post-rift sequence III is only documented on the continental shelf and upper slope (de Vera et al., 2010). It has been interpreted as a locally developed mass transport complex that is fed by localised source areas that do not have a constant supply of shelf- or slope-derived, extrabasinal sediments (Moscardelli and Wood, 2007; de Vera et al., 2010).

Boyd et al. (2011) recorded a number of gas leakage structures on the continental shelf. These included pockmarks, mounds and gas chimneys. In this study, only pockmarks were observed in the deepwater environment. The pockmarks on the shelf are much smaller than those recorded in the deepwater environment. The sizes of the pockmarks on the shelf range from 100 to 400 m in diameter whereas those interpreted in the deepwater environment range from 700 to 1100 m in diameter (Boyd et al., 2011). Their geometry and distribution differs due to their differences in formation. The pockmarks in the deepwater Orange Basin are large and elongated in the WNW-ESE direction. They are limited to areas with abrupt changes in the underlying sequences and localise into linear arrays. The pockmarks reported along the continental shelf of the Orange Basin differ from those in the deepwater environment in that they are smaller and circular. The pockmarks in the study are structurally controlled whereas the ones on the shelf form above stratigraphically controlled gas chimneys (Boyd et al., 2011).

8. CONCLUSION

Numerous passive margins have linked updip extension and downdip contraction domains that formed as a result of gravitational failure. The shale detached thrust faults, pockmarks and submarine canyons observed in this study are not unique to the deepwater Orange Basin and have been documented in other deepwater areas along passive margins (Cole et al., 2000; Rowan et al., 2004; Corredor et al., 2005; Gay et al., 2006; Morley, 2009a; Morley, 2009b). This study has shown that the deformation styles in sedimentary basins offshore passive margins are not always controlled by the type of detachment, they may have formed independently from the detachment, such as the folds imaged in the deepwater Orange Basin. In the deepwater Orange Basin, basinward-verging asymmetric folds with gently dipping backlimbs and landward-dipping thrust faults that sole into two detachments have been identified. The structural styles observed in the deepwater Orange Basin are similar to those reported in sedimentary basins offshore the western margin of Africa, particularly the Niger Delta. The deepwater thrust fault systems in these basins are characterised by landward-dipping thrust faults that sole into shale detachments. However, the lithological response to deformation in the deepwater Orange Basin differs from that of the Niger delta.

Seismic attributes have been shown to be indispensable tools in seismic interpretation. The application of seismic attributes in the deepwater Orange Basin resulted in the delineation of third-order scale structures and highlighted fault connectivity between the Coniacian-Santonian thrust system and overlying S-SW dipping normal faults. There is preferential flow of gas possibly from the Cenomanian-Turonian source rocks to the seafloor. Gas flows through thrust faults, attached to the Cenomanian-Turonian detachment, which exploit the S-SW dipping normal faults that terminate on the seafloor, beneath pockmarks. The S-SW dipping normal faults are more continuous and they propagate up section until they reach the seafloor whereas the WSW and N-ENE dipping normal faults terminate in the Palaeogene. The observations detailed above suggest that the distribution of pockmarks is controlled by structures. The formation of the submarine canyon is debatable. The results suggest that the submarine canyons formed by two slumping events (Coniacian to Santonian and Late Cenozoic). These

slumping events caused mass movement of sediment downslope. As sediments flow downslope they erode the underlying lithologies and form canyons. However, no submarine canyons have been recorded along the upper slope of the Orange Basin.

The shelf and deepwater environments in passive margins are not analogous. The processes forming features on the seafloor, on the continental shelf and the deepwater are unrelated. Conclusions were drawn from the absence of incisions made by submarine canyons on the shelf edge and upper continental slope and the absence of post-rift sequence III in the deepwater setting. The submarine canyons and pockmarks in the deepwater are predominantly structurally controlled whereas the pockmarks on the continental shelf form above stratigraphically controlled gas chimneys and the submarine canyons observed in other Atlantic passive margins form as a result of slope failure and erosive turbidity currents sourced from the continental shelf and upper slope (Pilcher and Argent, 2007; Boyd et al., 2011; Hartwig et al., 2012; de Almeida et al., 2015).

A broad comparison between the structural styles observed in the deepwater Orange Basin and those reported in other shale detachment deepwater basins (eg. Niger Delta – Nigeria, Amazon fan and Krishna-Godavari Basin – India) suggests more similarities than differences. The notable differences were as a result of fault and fold formation. The fault development in the Niger Delta was by fault-propagation upward from the detachment prior to fold formation whereas in the deepwater Orange Basin, faults developed within the fold limbs after formation of folds (Morley et al., 2011; Morley et al., 2018). A number of models (no shear fault-bend fold, fault-propagation fold, shear fault bend and break thrust) have been proposed to explain the geometries observed in deepwater thrust fault systems. One model cannot be used as a means of describing the formation of fault and fold geometries in all deepwater thrust fault systems.

Although the use of seismic data offered a good overview, integrating mineralogical, geochronological, kinematic and well data to further constrain the interpretation will provide a comprehensive understanding of the stratigraphy, structures and deformation mechanisms.

REFERENCES

Aldrich, J., Zilinski, R., Edman, J., Leu, W. and Corbett, K. (2003). Documentation of a new petroleum system in the South Atlantic. AAPG Annual Convention. Salt Lake City, Utah.

Anka, Z., Loegering, M., di Primio, R., Marchal, D., Rodriguez, J. and Vallejo, E. (2014). Distribution and origin of natural gas leakage in the Colorado Basin, offshore Argentina Margin, South America: seismic interpretation and 3D basin modelling. Geologica Acta, **12**, 269-285.

Bacon, M., Simm, R. and Redshaw, T. (2003). 3-D Seismic Interpretation. Cambridge University Press. 234pp

Bagguley, J. and Prosser, S. (1999). The interpretation of passive margin depositional processes using seismic stratigraphy: examples from offshore Namibia. Geological Society, London, Special Publications, 321 - 344.

Barrett, P. and Froggatt, P. (1978). Densities, porosities, and seismic velocities of some rocks from Victoria Land, Antarctica. New Zealand Journal of Geology and Geophysics, **21**, 175-187.

Barton, N. (2007). Rock quality, seismic velocity, attenuation and anistropy. London: CRC Press. 729pp

Bilotti, F. and Shaw, J. (2005). Deep-water Niger Delta fold and thrust belt modeled as a critical-taper wedge: The influence of elevated basal fluid pressure on structural styles. AAPG bulletin, **89**, 1475-1491.

Biondi, B. (2006). 3D seismic imaging: Investigations in Geophysics Series No. 14. Tulsa: Society of Exploration Geophysicist. 224pp

Bover-Arnal, T., Salas, R., Guimerà, J. and Moreno-Bedmar, J. (2014). Deep incision in an Aptian carbonate succession indicates major sea-level fall in the Cretaceous. Sedimentology, **61**, 1558-1593.

Boyd, D., Anka, Z., di Primio, R., Kuhlmann, G. and De Wit, M. (2011). Passive Margin Evolution and Controls on Natural Gas Leakage in the Orange Basin, South Africa. South African Journal of Geology, **114**, 349-366.

Brandes, C. and Tanner, D. (2014). Fault-related folding: A review of kinematic models and their application. Earth-Science Reviews , **138**, 352-370.

Brett, M. (2016). An introduction to smoothing. Retrieved October 30, 2017, from https://matthew-brett.github.io/teaching/smoothing_intro.html

Briggs, S., Davies, R., Cartwright, J. and Morgan, R. (2006). Multiple detachment levels and their control on fold styles in the compressional domain of the deepwater west Niger Delta. Basin Research, **18**, 435-450.

Broad, D., Jungslager, E., McLachlan, I. and Roux, J. (2006). Offshore Mesozoic Basins. In: Johnson, M.R., Anhaeusser, C.R., Thomas, R.J. (Eds.), The Geology of South Africa. Geological Society of South Africa and Council for Geoscience, 553–571.

Brown, A. (1996). Seismic attributes and their classification. The Leading Edge,**10**, 1090.

Brown, A. (2001). Understanding seismic attributes. Geophysics, **66**, 47-48.

Brown, A. (2011). Interpretation of Three-Dimensional Seismic Data (Vol.7). Tulsa: The American Association of Petroleum Geologists and the Society of Exploration Geophysicists, 646pp

Brown, L., Benson, J., Brink, G., Doherty, S., Jollands, A., Jungslager, E., Keenen, J.H.G., Muntingh, A. and van Wyk, N.J.S. (1995). Sequence Stratigraphy on Offshore South African Divergent Basins. An atlas on exploration for Cretaceous lowstand traps. Soekor (Pty) Ltd. Studies in Geology. American Association of Petroleum Geologists 41, 184pp.

Bull, S. and Cartwright, J. (2010). Small-Scale Insights into Seismic-Scale Slumps: A Comparison of Slump Features from the Waitemata Basin, New Zealand, and the Møre Basin, Off-Shore Norway. . In: Mosher, D., Shipp, R.C., Moscardelli, L., Chaytor, J. D., Baxter, C.D.P., Lee, H.J., Urgeles, R. (Eds.), Submarine Mass Movements and Their Consequences, 257–266.

Bünz, S., Mienert, J., Bryn, P. and Berg, K. (2005). Fluid flow impact on slope failure from 3D seismic data: a case study in the Storegga Slide. Basin Research, **17**, 109-122

Campher, C. (2010). Geological modelling of the offshore Orange Basin, west coast South Africa. University of the Western Cape, Unpublished MSc, 199pp.

Carrington, L. (2012). Sh-wave refraction and reflection investigation of Quaternary geology - Central United States seismic observatory. Lexington: University of Kentucky.

Catuneanu, O., Galloway, W., Kendall, C., Miall, A., Posamentier, H., Strasser, A., and Tucker, M.E. (2011). Sequence Stratigraphy: Methodology and Nomenclature. Newsletter on Stratigraphy, **44**, 173-245.

Childs, C. (2004). Interpolating surfaces in ArcGis spatial analyst. Developer's corner, 32-35.

Cifci, G., Dondurur, D. and Ergun, M. (2003). Deep and shallow structures of large pockmarks in the Turkish shelf, Eastern Black Sea. Geo-Marine Letters, **23**, 311-322.

Clemson, J., Cartwright, J.and Booth, J. (1997). Structural Segmentation and the influence of basement structure on the Namibian passive margin. Journal of the Geological Society, **154**, 477-482.

Cole, D., Stewart, S. and Cartwright, J. (2000). Giant irregular pockmark craters in the Palaeogene of the Outer Moray Firth Basin, UK North Sea. Marine and Petroleum Geology, **17**, 563-577.

Corredor, F., Shaw, J. and Bilotti, F. (2005). Structural styles in the deep-water fold and thrust belts of the Niger Delta. AAPG Bulletin , **89**, 753-780.

Coward, M., Purdy, E., Ries, A. and Smith, D. (1999). The distribution of petroleum reserves in basins of the South Atlantic margins. In Cameron, N., Bate, R., and Clure, V (Eds.), The oil and gas habitats of the South Atlantic, 101-131

Cox, T. and Seitz, K. (2007). Ant tracking seismic volumes for automated fault interpretation. Calgary: CSPG CSEG Convention.

Cramez, C. and Jackson, M. P. A. (2000). Superposed deformation straddling the continental–oceanic transition in deep-water Angola. Marine and Petroleum Geology, **17**, 1095-1109.

Davies, T. and Austin, J. (1997). High-Resolution 3D Seismic Reflection and Core Techniques Applied to Late Quaternary Deposits on the New Jersey Shelf. Marine Geology, **143**, 137 - 141.

Davis, G., Reynolds, S. and Kluth, C. (2012). Structural Geology of Rocks and Regions (3rd ed.). Hoboken: John Wiley & Sons, Inc. 864pp

Davy, B., Pecher, I., Wood, R., Carter, L. and Gohl, K. (2010). Gas escape features off New Zealand: evidence of massive release of methane from hydrates. Geophysical Research Letters , **37**, L21309.

de Almeida, N., Vital, H. and Gomes, M. (2015). Morphology of submarine canyons along the continental margin of the Potiguar Basin, NE Brazil. Marine and Petroleum Geology, **68**, 307-324.

de Vera, J., Granado, P. nd McClay, K. (2010). Structural Evolution of the Orange Basin Gravity-Driven System, Offshore Namibia. Marine and Petroleum Geology, **27**, 223-237.

Dentith, M. and Mudge, S. (2014). Geophysics for the Mineral Exploration Geoscientist. New York: Cambridge University Press. 425pp

Dingle, R. (1980). Large allochthonous sediment masses and their role in the construction of the continental slope and rise off southwestern Africa. Marine Geology, **37**, 333-354.

Dingle, R. (1992). Structural and sedimentary development of the continental margin off southwestern Africa. Communications of the Geological Survey of Namibia, **8**, 37-46.

Dingle, R. V. and Scrutton, R. A. (1974). Continental breakup and the development of post-Paleozoic sedimentary basins around southern Africa. Geological Society of America Bulletin, **85**, 1467-1474.

Dinis, J. and Trincão, P. (1995). Recognition and stratigraphical significance of the Aptian unconformity in the Lusitanian Basin, Portugal. Cretaceous Research, **16**, 171-186.

Futalan, K., Mitchell, A., Amos, K. and Backe, G. (2012). Seismic Facies Analysis and Structural Interpretation of the Sandakan Sub-basin, Sulu Sea, Philippines. AAPG International Conference and Exhibition. Singapore

García-Mondéjar, J. (1990). The Aptian-Albian carbonate episode of the Basque-Cantabrian Basin (northern Spain): general characteristics, controls and evolution. In Tucker, M., Wilson, J., Crevello, P., Sarg, J. and Read, J (Eds.), Carbonate platforms: facies, sequences and evolution, 257-290.

Gas, I. A. (2011, April). An Overview of Marine Seismic Operations. Retrieved 10 20, 2016, from http://www.ogp.org.uk/pubs/448.pdf

Gay, A., Lopez, M., Cochonat, P., Séranne, M., Levaché, D. and Sermondadaz, G. (2006). Isolated seafloor pockmarks linked to BSRs, fluid chimneys, polygonal faults and stacked Oligocene–Miocene turbiditic palaeochannels in the Lower Congo Basin. Marine Geology, **226**, 25-40.

Gibson, M., Jolley, S. and Barnicoat, A. (2000). Interpretation of the Western Ultra Deep Levels 3D seismic survey. The Leading Edge, **19**, 730-735.

Granado, P., de Vera, J. and McClay, K. (2009). Tectonostratigraphic evolution of the Orange Basin, SW Africa. Trabajos de Geologia, **29**, 321 - 328.

Handbury, G. and Sorensen, K. (2013). 3D Seismic Survey Dolphin Job Number: 3014-PDC-Shell SA Shell Orange Basin, South Africa Final Survey Report. Dolphin Geophysical.

Hansberry, R., King, R., Collins, A. and Morley, C. (2014). Complex structure of an upper-level shale detachment zone: Khao Khwang fold and thrust belt, Central Thailand. Journal of Structural Geology, **67**, 140-153.

Hartwig, A. (2014). Hydrocarbon migration and leakage dynamics of the Orange Basin, South Africa. Berlin: Technischen Universität Berlin. 256pp

Hartwig, A., Anka, Z. and di Primio, R. (2012). Evidence of a widespread paleo-pockmarked field in the Orange Basin: An indication of an early Eocene massive fluid escape event offshore South Africa. Marine Geology, **332**, 222-234.

Herron, D. (2011). First steps in seismic interpretation: Geophysical monograph series no. 16, Tulsa: Society of Exploration Geophysicists. 203pp

Herron, D. (2014). Pitfalls in horizon autopicking. Interpretations, **3**, SB1-SB4.

Hersi, O., Abbasi, I., Al-Harthy, A., Cherchi, A. and Schroeder, R. (2014). Stratigraphic evolution and depositional system of lower Cretaceous Qishn formation, Dhofar, Oman. London: Geological Society Special Publication, **392**, 303-323.

Hirsch, K., Scheck-Wenderoth, M., Paton, D. and Bauer, K. (2007). Crustal Structure Beneath the Orange Basin, South Africa. South African Journal of Geology, **110**, 249-260.

Hirsch, K., Scheck-Wenderoth, M., van Wees, J., Kuhlmann, G. and Paton, D. (2010). Tectonic Subsidence History and Thermal Evolution of the Orange Basin. Marine and Petroleum Geology, **27**, 565-584.

Hovland, M., Gardner, J. V. and Judd, A. V. (2002). The significance of pockmarks to understanding fluid flow processes and geohazards. Geofluids, **2**, 127-136.

Huang, Z., Nichol, S., Harris, P. and Caley, M. (2014). Classification of submarine canyons of the Australian continental margin. Marine Geology, **357**, 362-383.

Hughes, A. N. and Shaw, J. H. (2014). Fault displacement-distance relationships as indicators of contractional fault-related folding style. AAPG bulletin, **98**, 227-251.

Hughes, A. and Shaw, J. (2015). Insights into the mechanics of fault-propagation folding styles. Geological Society of America Bulletin, **127**, 1752-1765.

Hughes, A., Benesh, N. and Shaw, J. (2014). Factors that control the development of fault-bend versus fault-propagation folds: Insights from mechanical models based on the discrete element method (DEM). Journal of Structural Geology, **68**, 121-141.

Immenhauser, A., Schlager, W., Burns, S., Scott, R., Geel, T., Lehmann, J., Van der Gaast, S. and Bolder-Schrijver, L.J.A. (1999). Late Aptian to late Albian sea-level fluctuations constrained by geochemical and biological evidence (Nahr Umr Formation, Oman). Journal of Sedimentary Research, **69**, 434-446.

Japsen, P. (2018). Sonic velocity of chalk, sandstone and marine shale controlled by effective stress: Velocity-depth anomalies as a proxy for vertical movements. Gondwana Research, **53**, 145-158.

Jolley, S., Stuart, G., Freeman, S., Knipe, R., Kershaw, D., McAllister, E., Barnicoat, A.C. and Tucker, R.F. (2007). Progressive Deformation of a Late Orogenic Thrust System, From Duplex Development to Extensional Reactivation and Disruption: Witwatersrand Basin, South Africa. Geological Society Special Publication, **272**, 543-569.

Jungslager, E. (1999). Petroleum habitats of the Atlantic margin of South Africa. In N. Cameron, N., Bate, R., and Clure, V (Eds.), The Oil and Gas Habitats of the South Atlantic. London: Geological Society, 153-168

Kelley, J. T., Dickson, S. M., Belknap, D. F., Barnhardt, W. A. and Henderson, M. (1994). Giant sea-bed pockmarks: Evidence for gas escape from Belfast Bay, Maine. Geology, **22**, 59-62.

Kerr, A. (1998). Oceanic plateau formation: a cause of mass extinction and black shale deposition around the Cenomanian–Turonian boundary? Journal of the Geological Society, London, **155**, 619-626.

Khair, H., Cooke, D., Backé, G., King, R., Hand, M., Tingay, M., and Holford, S. (2012). Subsurface mapping of natural fracture networks; A major challenge to be solved. Case study from the shale intervals in the Copper Basin, South Australia. PROCEEDINGS, Thirty-Seventh Workshop on Geothermal Reservoir Engineering. Stanford University, Stanford, California.

Koson, S., Chenrai, P. and Choowong, M. (2014). Seismic attributes and seismic geomorphology. Bulletin of Earth Sciences of Thailand , **6**, 1-9.

Kostenko, O. and Naruk, S. (2009). 3-D geometry and kinematic evolution of deep-water toe thrust anticlines. Denver: AAPG Annual Convention.

Kramer, E. and Heck, L. (2014). Orange Basin 3D Pre-processing and preSDM 2013. Netherlands: Shell Global Solutions International B.V., Risjswijk.

Kuhlmann, G., Adams, S., Anka, Z., Campher, C., di Primio, R. and Horsfield, B. (2011). 3D petroleum systems modelling within a passive margin setting, Orange Basin, blocks 3/4, offshore South Africa–implications for gas generation, migration and leakage. South African Journal of Geology, **114**, 387-414.

Kuhlmann, G., Adams, S., Campher, C., van der Spuy, D., di Primio, R. and Horsfield, B. (2010). Passive margin evolution and its controls on natural gas leakage in the southern Orange Basin, blocks 3/4, offshore South Africa. Marine and Petroleum Geology, **27**, 973-992.

Lastras, G., Acosta, J., Muñoz, A. and Canals, M. (2011). Submarine canyon formation and evolution in the Argentine Continental Margin between 44°30'S and 48°S. Geomorphology, **128**, 116-136.

Lavier, L.L., Steckler, M. S. and Brigaud, F. (2001). Climatic and tectonic control on the Cenozoic evolution of the West African margin. Marine Geology, **178**, 63-80

Leckie, R. M., Bralower, T. J. and Cashman, R. (2002). Oceanic anoxic events and plankton evolution: Biotic response to tectonic forcing during the mid-Cretaceous. Paleoceanography, **17**, 13.1-13.29.

Light, M., Maslanyj, M. and Banks, N. (1992). New Geophysical Evidence for Extensional Tectonics on the Divergent Margin Offshore Namibia. In Storey, B., Alabaster, T. and Pankhurst, R (Eds.), Magmatism and the Causes of Continental Break-Up. London: Geological Society Special Publication, 257-270

Light, M., Maslanyj, M., Greenwood, R. and Banks, N. (1993). Seismic Sequence Stratigraphy and Tectonics Offshore Namibia. In Williams, G and Dobb, A (Eds.), Tectonics and Seismic Sequence Stratigraphy. London: Geological Society Special Publication, 163-191

Liner, C. (2016). Elements of 3D seismology: Investigation in Geophysics Series No. 19. Tulsa: Society of Exploration Geophysicists. 340pp

Lines, L. and Newrick, R. (2004). Geophysical monograph series - Fundamentals of geophysical interpretation. Tulsa: Society of Exploration Geophysicists. 274

Loegering, M., Anka, Z., Autin, J., di Primio, R., Marchal, D., Rodriguez, J., Franke, D. and Vallejo, E. (2013). Tectonic evolution of the Colorado Basin, offshore Argentina, inferred from seismo-stratigraphy and depositional rates analysis. Tectonophysics , **604**, 245-263.

Maloney, D., Davies, R., Imber, J., Higgins, S., and King, S. (2010). New insights into deformation mechanisms in the gravitationally driven Niger Delta deep-water fold and thrust belt. AAPG bulletin, **94**, 1401-1424.

Manzi, M. (2013). Application of 3D seismic analysis techniques to evaluate ore resources on Kloof, South Deeps and Driefontein gold mines, Witwatersrand Basin, South Africa. Geophysics, **77**, 133-147

Manzi, M., Durrheim, R., Hein, K. and King, N. (2012b). 3D edge detection seismic attributes used to map potential conduits for water and methane in deep gold mines in the Witwatersrand basin, South Africa. Geophysics, **77**, WC133-WC147.

Manzi, M., Gibson, M., Hein, K., King, N. and Durrheim, R. (2012a). Application of 3D seismic techniques to evaluate ore resources in the West Wits Line goldfield and portions of the West Rand goldfield, South Africa. Geophysics, **77**, 163 - 171.

Manzi, M., Hein, K., King, N. and Durrheim, R. (2013). Neoarchaean tectonic history of the Witwatersrand Basin and Ventersdorp Supergroup: New constraints from high-resolution 3D seismic reflection data. Tectonophysics, **590**, 94 - 105.

Marfurt, K. and Chopra, S. (2007). Seismic Attributes for the Prospect Identification and Reservoir Characterization. Tulsa: Society of Exploration Geophysicists. 315pp

McMahon, N. A. and Turner, J. (1998). The documentation of a latest Jurassic-earliest Cretaceous uplift throughout southern England and adjacent offshore areas. Geological Society, London, Special Publications, **133**, 215-240.

Mondt, J. (1993). Use of Dip and Azimuth Horizon Attributes in 3D Seismic Interpretation. Society of Petroleum Engineers, **8**, 253-257.

Morley, C. (1994). Fold-generated imbricates: examples from the Caledonides of Southern Norway. Journal of Structural Geology, **16**, 619-631.

Morley, C. (2009a). Growth of folds in a deep-water setting. Geosphere, **5**, 59-89.

Morley, C. (2009b). Geometry of an oblique thrust fault zone in a deepwater fold belt from 3D seismic data. Journal of Structural Geology, **31**, 1540-1555.

Morley, C., King, R., Hillis, R., Tingay, M. and Backe, G. (2011). Deepwater fold and thrust belt classification, tectonics, structure and hydrocarbon prospectivity: A review. Earth Science Reviews, **104**, 41-91.

Morley, C., von Hagke, C., Hansberry, R., Collins, A., Kanitpanyacharoend, W. and King, R. (2018). Review of major shale-dominated detachment and thrust characteristics in the diagenetic zone: Part II, rock mechanics and microscopic scale. Earth Science Reviews, **176**, 19-50.

Moscardelli, L. and Wood, L. (2007). New classification system for mass transport complexes in offshoreTrinidad. Basin Research , **20**, 73-98.

Muntingh, A. (1993). Geology, prospects in Orange Basin offshore western South Africa. Oil and Gas Journal; (United States), **91**.

Ngeri, A., Tamunobereton-ari, I., and Amakiri, A. (2015). Ant-tracker attributes: an effective approach to enhancing fault identification and interpretation. Journal of VLSI and Signal Processing, **5**, 67-73.

Nietzsche, F. (2005). Common techniques for quantitative seismic interpretation. In Avseth, P. Mukerji, T and Mavko, G (Eds.), Quantitative Seismic Interpretation : Applying Rock Physics Tools to Reduce Interpretation Risk. Cambridge: Cambridge University Press.

National Oceanic and Atmospheric Administration. Retrieved 03, 2017, from https://maps.ngdc.noaa.gov/viewers/bathymetry, March, 2017

Paton, D., di Primio, R., Kuhlmann, G., van der Spuy, D. and Horsfield, B. (2007). Insight into the Petroleum System Evolution of the southern Orange Basin, South Africa. South African Journal of Geology, **110**, 267-274.

Paton, D., van der Spuy, D., di Primio, R. and Horsfield, B. (2008). Tectonically Induced Adjustment of Passive Margin Accommodation Space; Influence on the Hydrocarbon Potential of the Orange Basin, South Africa. American Association of Petroleum Geologists, **92**, 589-609.

Pereira, L. (2009). Seismic Attributes in Hydrocarbon Reservoirs Characterization. Universidade de Aveiro, Departamento de Geociências. Portugal: unpublished.165pp

Petroleum Agency South Africa. (2013). History Of Exploration And Production. Retrieved January 8, 2018, from www.petroleumagencysa.com/index.php/petroleum-geologyresources/exploration-history

Pilcher, R. and Argent, J. (2007). Mega-pockmarks and linear pockmark trains on the West African continental margin. Marine Geology , **244**, 15-32.

Qin, X. H. (2014). Rock physics modeling of organic-rich shales with different maturity levels. SEG Denver 2014 Annual Meeting. Society of Exploration Geophysicists.

Randen, T. and Sønneland, L. (2005). Atlas of 3D seismic attributes. In Mathematical Methods and Modelling in Hydrocarbon Exploration and Production. Heidelberg: Springer . 23-46

Randen, T. Pedersen, S., and Sonneland, L. (2001). Automatic Extraction of Fault Surfaces from Three-Dimensional Seismic Data. San Antonio: SEG International Exposition and Annual Meeting.

Rekdal, T. and Long, A. (2006). Recent advances in marine seismic acquisition and processing technology. Recorder: Canadian Society of Exploration Geophysicists, **31**.

Rijks, E. and Jauffred, J. (1991). Attribute extraction: An important application in any detailed 3-D interpretation study. The Leading Edge, **10**, 10-19.

Robin, C., Gorican, S., Guillocheau, F., Razin, P., Dromart, G. and Mosaffa, H. (2010). Mesozoic deep-water carbonate deposits from the southern Tethyan passive margin in Iran (Pichakun nappes, Neyriz area): biostratigraphy, facies sedimentology and sequence stratigraphy. Geological Society, London, Special Publications, **330**, 179-210.

Rogers, J. and Rau, A. J. (2006). Surficial sediments of the wave dominated Orange River Delta and the adjacent continental margin off south-western Africa. African Journal of Marine Science, **28**, 511-524

Rowan, M. G., Peel, F. G, and Vendeville, B. C. (2004). Gravity-driven fold belts on passive margins. In McClay, K.R (Ed.), Thrust tectonics and hydrocarbon systems: AAPG Memoir 82, 157-182.

Ruffell, A. H. (1992). Early to mid-Cretaceous tectonics and unconformities of the Wessex Basin (southern England). Journal of the Geological Society, **149**, 443-454.

Salisbury, M., Harvey, G. and Mathews, L. (2003). The acoustic properties of ores and host rocks in hardrock terranes. In Eaton, D., Milkereit, B. and Salisbury, M (Eds.), Hardrock Seismic Exploration, Geophysical Developments 10. Society of Exploration Geophysicists. 9 - 19

Scarselli, N., McClay, K. and Elders, C. (2016). Seismic geomorphology of cretaceous megaslides offshore Namibia (Orange Basin): Insights into segmentation and degradation of gravity-driven linked systems. Marine and Petroleum Geology , **75**, 151-180.

Schmelzbach, C. (2007). Seismic-Reflection and Seismic-Refraction Imaging of the South Portuguese Zone Fold-and-Thrust Belt. Uppsala, Sweden: Department of Earth Sciences, Geophysics,Villav. 16, Uppsala University. 87pp

Seranne, M., and Anka, Z. (2005). South Atlantic continental margins of Africa: A comparison of the tectonic vs climate interplay on the evolution of equatorial west Africa and SW Africa margins. Journal of African Earth Sciences, **43**, 283-300.

Shaw, J., Connors, C., and Suppe, J. (2005). Seismic Interpretation of Contractional Fault-Related Folds: An AAPG Seismic Atlas Studies in Geology 53. Tulsa, Oklahoma: American Association of Petroleum Geologists. 156pp

Sheriff, R. (1996). Understanding the Fresnel Zone. The Geophysical Corner, 1 - 2.

Sheriff, R. E. (2002). Encyclopedic Dictionary of Applied Geophysics (4th ed.). Tulsa: Society of Exploration Geophysicist. 429pp

Sheriff, R., and Geldart, L. (1995). Exploration Seismology (2nd ed.). Cambridge University Press, 592pp

Solihulhadi, M., and Tolioe, W. (2007). 3D Seismic Data Conditioning to Enhance Fault Interpretation. PROCEEDINGS, Indonesian Petroleum Association. Thirty-First Annual Convention and Exhibition.

Suppe, J. (1983). Geometry and kinematics of fault-bend folding. American Journal of science, **283**, 684-721.

Suppe, J., and Medwedeff, D. (1990). Geometry and kinematics of fault-propagation folding. Eclogae Geologicae Helvetiae, **83**, 409-454.

Suppe, J., Connors, C., and Zhang, Y. (2004). Shear fault-bend folding. In McClay, K.R (Ed.), Thrust tectonics and hydrocarbon systems. AAPG Memoir 82, 303-323

Thomas, D. (2015). Marine Insight. Retrieved January 08, 2018, from https://www.marineinsight.com/types-of-ships/what-methods-are-used-for-marine-seismic-operations-at-sea/

Van Der Spuy, D. (2003). Aptian source rocks in some South African Cretaceous Basins. In Arthur, T. MacGregor, D. and Cameron, N (Eds.), Petroleum Geology of Africa: New Themes and Developing Technologies. 185-202

Van Wagoner, J., Mitchum Jr., R., Posamenteir, H., and Vail, P. (1987). Seismic stratigraphy interpretation procedure using sequence stratigraphy, Part II: key definitions of sequence stratigraphy. In Bally, A. (Ed.), Atlas of seismic stratigraphy. American Association of Petroleum Geologists studies in geology 27,**1**, 11-14

Van Wagoner, J., Posamenteir, H., Mitchum Jr., R., Vail, P., Sarg, J., Loutit, T. and Hardenbol, J. (1988). An overview of the fundamentals of sequence stratigraphy and key definitions. In Wilgus, C. (Ed.), Sealevel changes: an integrated approach. The Society of Economic Paleontologists and Mineralogists Special publication 42, 39-45

Watkeys, M. (2006). Gondwana Break-Up: A South African Perspective. In Johnson, M., Anhaeusser, C. and Thomas, R. The Geology of South Africa. Pretoria: Geological Society of South Africa, Johannesburg/Council for Geoscience. 691pp

Wigley, R. and Compton, J.S. (2006). Late Cenozoic evolution of the outer continental shelf at the Head of the Cape Canyon, South Africa Marine Geology, **226**, 1-23

Woodward, N. (1997). Low-amplitude evolution of break-thrust folding. Journal of Structural Geology, **19**, 293-301.

Wu, S., and Bally, A. W. (2000). Slope tectonics— comparisons and contrasts of structural styles of salt and shale tectonics of the northern Gulf of Mexico with shale tectonics of offshore Nigeria in Gulf of Guinea. In Mohriak, W. and Talwani, M (Eds.), Atlantic rifts and continental margins: American Geophysical Union Geophysical Monograph 115, 151-172.

Yilmaz, O. (2001). Seismic data analysis - Processing, inversion, and interpretation of seismic data. Tulsa: Society of Exloration Geophysicists, 2027pp

Yilmaz, O. and Baysal, E. (2015). An Effective Ghost Removal Method for Marine Broadband Seismic Data Processing. 77th EAGE Conference & Exhibition 2015 Madrid, Spain: IFEMA Madrid. 1-5

Appendix A

Table 1: Vertical displacement of faults along strike measured in seconds.

	Vertical displacement in seconds																				
	Fault_0	Fault_1	Fault_2	Fault_3	Fault_3A	Fault_4	Fault_5	Fault_6	Fault_7	Fault_7A	Fault_8	Fault_9	Fault_10	Fault_10A	Fault_11	Fault_12	Fault_12A	Fault_12B	Fault_13	Fault_14	Fault_15	Fault_16
6651000																						0.06
6650000																					0.07	
6649000																				0.07	0.06	
6648000																		0.03				
6647000																	0.08	0.03	0.03			
6646000																	0.105	0.115				
6645000											0.06	0.035		0.04	0.02							
6644000						0.05	0.15	0.035		0.06	0.07	0.085		0.13	0.035							
6643000				0.22		0.11	0.235	0.1	0.06	0.06	0.025	0.025	0.04									
6642000		0.09		0.1			0.245	0.11	0.03	0.05	0.03	0.01										
6641000			0.135	0.22			0.275	0.12	0.06	0.06												
6640000			0.08	0.2			0.265	0.085	0.05	0.07												
6639000			0.08	0.235			0.25	0.1														
6638000	0.04		0.1	0.235			0.19															
6637000	0.085		0.14	0.21	0.025																	
6636000	0.1		0.15	0.18	0.03																	
6635000	0.1		0.13	0.185	0.05																	
6634000	0.16		0.135																			
6633000	0.05																					

Table 2: Fault displacement measurements along strike measured in metres. The faults with more than 2 displacement measurements recorded along the strike of the fault are presented in this table.

	Vertical displacement in metres										
	Fault_0	Fault_2	Fault_3	Fault_3A	Fault_5	Fault_6	Fault_7	Fault_7A	Fault_8	Fault_9	Fault_12B
6651000											
6650000											
6649000											
6648000											
6647000											
6646000											
6645000									90	53	45
6644000					225	53		90	105	128	45
6643000			330		353	150	90	90	38	38	173
6642000			150		368	165	45	75	45	15	
6641000		203	330		413	180	90	90			
6640000		120	300		398	128	75	105			
6639000		120	353		375	150					
6638000	60	150	353		285						
6637000	128	210	315	38							
6636000	150	225	270	45							
6635000	150	195	278	75							
6634000	240	203									
6633000	75										

Table 3: Vertical displacement on individual faults measure along the fault ramp in seconds. The colours represent the interfaces in Figure 5.18 where displacement measurements were recorded.

	Vertical displacement in seconds																					
	Fault_0	Fault_1	Fault_2	Fault_3	Fault_3A	Fault_4	Fault_5	Fault_6	Fault_7	Fault_7A	Fault_8	Fault_9	Fault_10	Fault_10A	Fault_11	Fault_12	Fault_12A	Fault_12B	Fault_13	Fault_14	Fault_15	Fault_16
6651000																						
Top																						0.06
Centre																						0.17
Bottom																						0.19
6650000																						
Top																					0.07	
Centre																					0.13	
Bottom																					0.14	
6649000																						
Top																				0.07	0.06	
Centre																				0.305	0.16	
Bottom																				0.065	0.1	
6648000																						
Top																		0.03				
Centre																		0.2				
Bottom																		0.07				
6647000																						
Top																	0.08	0.03	0.03			
Centre																	0.23	0.14	0.03			
Bottom																	0.075	0.03	0.035			
6646000																						
Top											0.05						0.105	0.115				
Centre											0.12						0.29	0.18				
Bottom											0.03						0.14	0.07				
6645000																						
Top											0.06	0.035		0.04	0.02							
Centre											0.22	0.1		0.13	0.18							
Bottom											0.04	0.04		0.06	0.21							
6644000																						
Top						0.05	0.15	0.035		0.06	0.07	0.085		0.13	0.035							
Centre						0.17	0.22	0.15		0.17	0.24	0.195		0.305	0.14							
Bottom						0.05	0.06	0.105		0.04	0.08	0.115		0.27	0.08							

Table 3 continued

6643000																							
Top				0.22		0.11	0.235	0.1	0.06	0.06	0.025	0.025	0.04										
Centre				0.245		0.08	0.255	0.025	0.14	0.17	0.07	0.02	0.26										
Bottom				0.05		0.06	0.135	0.045	0.03	0.08	0.05	0.01	0.06										
6642000																							
Top		0.09		0.1			0.245	0.11	0.03	0.05	0.03	0.01											
Centre		0.11		0.22			0.34	0.05	0.16	0.17	0.2	0.09											
Bottom		0.09		0.23			0.12	-	-	0.04	0.155	0.03											
6641000																							
Top			0.135	0.22			0.275	0.12	0.06	0.06													
Centre			0.27	0.26			0.31	0.13	-	0.12													
Bottom			0.1	0.15			0.14	0.12	-	0.1													
6640000																							
Top			0.08	0.2			0.265	0.085	0.05	0.07													
Centre			0.235	0.26			0.25	0.21	0.19	0.17													
Bottom			0.115	0.14			0.11	0.17	0.08	0.04													
6639000																							
Top			0.08	0.235			0.25	0.1															
Centre			0.12	0.35			0.31	0.2															
Bottom			0.115	0.11			0.1	0.16															
6638000																							
Top	0.04		0.1	0.235			0.19																
Centre	0.2		0.22	0.23			0.26																
Bottom	0.12		0.1	0.1			0.08																
6637000																							
Top	0.085		0.14	0.21	0.025																		
Centre	0.095		0.15	0.2	0.115																		
Bottom	0.09		0.125	0.11	0.02																		
6636000																							
Top	0.1		0.15	0.18	0.03																		
Centre	0.11		0.16	0.26	0.08																		
Bottom	0.13		0.1	0.07	0.07																		

Table 4: Vertical displacement on individual faults measure along the fault ramp in metres. The colours represent the interfaces in Figure 5.18 where displacement measurements were recorded.

	Fault throws in metres																					
	Fault_0	Fault_1	Fault_2	Fault_3	Fault_3A	Fault_4	Fault_5	Fault_6	Fault_7	Fault_7A	Fault_8	Fault_9	Fault_10	Fault_10A	Fault_11	Fault_12	Fault_12A	Fault_12B	Fault_13	Fault_14	Fault_15	Fault_16
6651000																						
Top																						90
Centre																						255
Bottom																						285
6650000																						
Top																					105	
Centre																					195	
Bottom																					210	
6649000																						
Top																				105	90	
Centre																				458	240	
Bottom																				98	150	
6648000																						
Top																		45				
Centre																		300				
Bottom																		105				
6647000																						
Top																	120	45	45			
Centre																	345	210	45			
Bottom																	113	45	53			
6646000																						
Top											75						158	173				
Centre											180						435	270				
Bottom											45						210	105				
6645000																						
Top											90	53		60	30							
Centre											330	150		195	270							
Bottom											60	60		90	315							
6644000																						
Top						75	225	53		90	105	128		195	53							
Centre						255	330	225		255	360	293		458	210							
Bottom						75	90	158		60	120	173		405	120							

Table 4 continued

6643000																							
Top				330		165	353	150	90	90	38	38	60										
Centre				368		120	383	38	210	255	105	30	390										
Bottom				75		90	203	68	45	120	75	15	90										
6642000																							
Top		135		150			368	165	45	75	45	15											
Centre		165		330			510	75	240	255	300	135											
Bottom		135		345			180	-	-	60	233	45											
6641000																							
Top			203	330			413	180	90	90													
Centre			405	390			465	195	-	180													
Bottom			150	225			210	180	-	150													
6640000																							
Top			120	300			398	128	75	105													
Centre			353	390			375	315	285	255													
Bottom			173	210			165	255	120	60													
6639000																							
Top			120	353			375	150															
Centre			180	525			465	300															
Bottom			173	165			150	240															
6638000																							
Top	60		150	353			285																
Centre	300		330	345			390																
Bottom	180		150	150			120																
6637000																							
Top	128		210	315	38																		
Centre	143		225	300	173																		
Bottom	135		188	165	30																		
6636000																							
Top	150		225	270	45																		
Centre		165		240	120	120																	
Bottom		195		150	105	105																	

Appendix B: 3D geological model

The full 3D model can be viewed in the attachment: Attachment of full 3D model.Mp4